

THE FLORIDA STATE UNIVERSITY

COLLEGE OF ARTS AND SCIENCES

NUMERICAL STUDY OF THE RELEVANCE OF CLUSTERED
STATES IN DILUTED MAGNETIC SEMICONDUCTORS AND
HIGH TEMPERATURE SUPERCONDUCTORS

By

GONZALO ALVAREZ

A dissertation submitted to the
Department of Physics
in partial fulfillment of the
requirements for the degree of
Doctor of Philosophy

Degree Awarded:
Summer Semester, 2004

The members of the Committee approve the dissertation of Gonzalo Alvarez defended on 05/12/04.

Elbio Dagotto
Professor Directing Dissertation

Naresh Dalal
Outside Committee Member

Adriana Moreo
Committee Member

James Brooks
Committee Member

Jorge Piekarewicz
Committee Member

The Office of Graduate Studies has verified and approved the above named committee members.

ACKNOWLEDGEMENTS

I would like to express my gratitude to my research advisor, Elbio Dagotto, for his support and encouragement throughout my graduate studies. It is not often that one has the opportunity to work with an advisor that always finds the time for listening to the little problems and basic questions that always appear when performing research. He has taught me innumerable lessons and insights on the workings of the scientific community and academic research.

Professor Adriana Moreo has helped and guided me with my research and teaching duties during my stay at Florida State University. To her I want to express also my deepest gratitude. The help of Jan Burgy is very much appreciated. Thanks to him, I expanded my skills and experience in computational physics. My thanks go also to FSU Professor Vladimir Dobrosajievic, for discussing with us his insights into the effects of disorder in strongly correlated electrons. Professor Thomas Dietl helped us with the GaN project in the fascinating field of magnetic semiconductors. I want to thank Dr. Yuki Motome for visiting us and helping me with the implementation of the expansion method proposed by them and used in part of this work. I acknowledge useful discussions about magnetic semiconductors with researchers at the University of Texas at Austin, Dr. Jaime Fernandez-Rossier and Dr. Jairo Sinova and at the University of Maryland, Dr. A. Chattopadhyay, Dr. S. Das Sarma and Dr. E. Hwang. The School of Computational Science and Information Technology at FSU kindly provided most of the computer resources used in this work. Special thanks go to the American Physical Society's topical group on magnetism for recognizing my graduate work by granting me the 2004 "Outstanding Dissertation in Magnetism award".

Last but not least, I would like to thank my friends at the National High Magnetic Field Lab, H. Aliaga, C. Busser, M. Mayr, M. Moraghebi, C. Sen and D. Tanaksovic, for their continued support.

TABLE OF CONTENTS

List of Figures	vii
Abstract	xiii
1. INTRODUCTION	1
1.1 Diluted Magnetic Semiconductors	1
1.2 Why study DMSs?	3
1.2.1 Technological Applications	3
1.2.2 Theoretical Interest	4
1.2.3 Motivation for Numerical Studies	4
1.3 Properties of (III,Mn)V DMS	6
1.4 Theoretical Models	9
1.4.1 Diluted Kondo Lattice Model	10
1.4.2 Band structure of III-V semiconductors	13
1.4.3 Coulomb interaction and direct exchange	15
1.5 Monte Carlo Methods	16
1.5.1 Monte Carlo Simulation	17
1.5.2 Observables	18
1.5.3 Polynomial Expansion Methods	19
2. PHASE DIAGRAM	21
2.1 Magnetic Properties	21
2.2 Carrier Concentration	22
2.3 Coupling Dependence	23
2.4 Local Spin Concentration	26
2.5 Summary	28
3. IMPURITY BAND AND DYNAMICAL PROPERTIES	30
3.1 Density of States	31
3.2 Optical Conductivity	36
3.3 Conductance and Metal-Insulator Transition	40
3.3.1 Theory	40
3.3.2 Numerical Results	43
3.4 Magnetoresistance	48

4. IMPORTANCE OF CLUSTERED STATES	51
4.1 Introduction	51
4.2 Clustered States in DMS Revisited	52
4.3 High- T_c Superconductors	53
4.3.1 Introduction	53
4.3.2 Clustered States	55
4.3.3 Method of Study	56
4.3.4 Exact Ground States	58
4.3.5 Non-Universal Phase Diagram	59
4.3.6 Local Order and Pseudo-gap Formation	62
4.3.7 Multilayers and Colossal Effects	64
4.4 Manganites	70
5. CONCLUSIONS	72
 APPENDICES	
A. RIGOROUS RESULTS FOR KONDO LATTICE AND RELATED MODELS	76
B. POLYNOMIAL EXPANSION METHOD	82
C. TRUNCATED POLYNOMIAL EXPANSION METHOD	85
REFERENCES	94
BIOGRAPHICAL SKETCH	103

LIST OF FIGURES

1.1 Three types of semiconductors: (a) a magnetic semiconductor, which has a periodic array of a magnetic element, (b) a <i>diluted magnetic semiconductor</i> (DMS), an alloy between a nonmagnetic semiconductor and a magnetic element and (c) a non-magnetic semiconductor, which contains no magnetic ions (from Ref. [1]).	2
1.2 Lattice structure of GaAs. White and black spheres represent the location of Ga and As atoms respectively.	15
1.3 Sketch of the energy bands of GaAs.	16
2.1 (a) $ M $ (circles) and spin-spin correlation C at maximum distance (squares) vs. T , on a 4^3 cluster, at $J/t = 1.0$, $x = 0.25$, and $p = 0.4$. The 0.25 horizontal line indicates the value of $ M $ at $T = \infty$. (b) $S(q = 0)$ vs. T , at $J/t = 2.0$, $x = 0.25$, and $p = 0.4$ using 4^3 (circles) and 6^3 (squares) lattices. In all cases T_C is indicated.	22
2.2 (a) Magnetization $ M $ (circles), and spin-spin correlation at maximum distance C (squares) vs. T , at $J/t = 1.0$, $x = 0.25$, and $p = 0.1$, using a 6^3 cluster. (b) $C(d)$ vs. d at $p \sim 3.0$, $x = 0.25$, $J/t = 1.0$, and $T/t = 0.005$, using an 8^2 cluster. The oscillations indicate an AF state.	23
2.3 (a) $ M $ (circles), spin-spin correlation at minimum distance $C(d_{min})$ (squares), and at maximum distance $C(d_{max})$ (diamonds) vs. J/t , for a 4^3 cluster at $x = 0.25$, $p = 0.1$, and $T/t = 0.005$. (b) MC phase diagram in 2D varying J/t , at fixed x and p . At large J/t , a broad scale T^* corresponds to the formation of uncorrelated clusters. T_C transition temperature, defined as the T where FM correlations develop at the largest distance in the clusters used. At small J/t , those temperatures are similar. The optimal J/t is intermediate between itinerant and localized regimes.	24
2.4 $\Delta E = E(\theta = \pi) - E(\theta = 0)$ vs. J/t calculated exactly on finite but large lattices at $T = 0$ for a system of 2 Mn-spins and 1 electron, where θ is the relative angle between the Mn-spins.	25
2.5 Exact $T=0$ local carrier density, for 1 carrier and 2 parallel spins at sites 10 and 20, of a 30-site chain, varying J/t	26

2.6 (a) T_C vs. x for $\text{Ga}_{1-x}\text{Mn}_x\text{As}$ [2] (thick line), and for model Eq. (1.1) using $t = 0.3$ eV (squares) and $t = 0.5$ eV (circles). In both cases, $p \sim 0.4$ and $J/t = 2.0$. Typical error bars are shown. Stars are results for $p \sim 0.5$, $J/t = 1$, and $t = 0.5$ eV. (b) Magnetization $ M $ vs. x for model Eq. (1.1) (circles) at $T/t = 0.005$, $J/t = 2$, $p = 0.4$, compared with the experimental value [1, 3] for $\text{Ga}_{1-x}\text{Mn}_x\text{As}$ at $x \sim 0.07$ and $T = 2\text{K}$ (squares).	27
2.7 (a) Phase diagram of the single-band model Eq. (1.1), as discussed throughout this Chapter. The figure shows schematically the T_C and T^* dependence on the coupling J/t . The region between T^* and T_C contains FM “clusters”, with magnetic moments that are not aligned. (b) Numerically obtained T_C vs. x and p , at $J/t = 2.0$. Filled circles are from model Eq. (1.1) with $t = 0.5$ eV. The green point corresponds to the experimental value for $\text{Ga}_{1-x}\text{Mn}_x\text{As}$ at $x \sim 0.1$	29
3.1 Schematic representation of the DOS, for a ferromagnetic configuration and strong enough J/t coupling. The “impurity band” has weight x , and the chemical potential μ lies within it.	32
3.2 $N_{\uparrow}(\omega)$ and $N_{\downarrow}(\omega)$ vs. $\omega - \mu$ for a 10×10 periodic system with 26 spins ($x \sim 0.25$) and 10 electrons ($p \sim 0.4$) at $T/t = 0.01$. Results are shown for $J/t = 2.0$, $J/t = 3.0$, $J/t = 4.0$, and $J/t = 6.0$ as indicated. $\omega - \mu$ is in units of the hopping, t . The results are averages over eight configurations of disorder (but there is no qualitative difference in the results from different configurations).	33
3.3 $N_{\uparrow}(\omega)$ and $N_{\downarrow}(\omega)$ vs. $\omega - \mu$ for a 6^3 periodic system with 54 spins ($x \sim 0.25$) and 16 electrons ($p \sim 0.4$) at $T/t = 0.01$. Results are shown for (a) $J/t = 2.0$, (b) $J/t = 4.0$, (c) $J/t = 6.0$. $\omega - \mu$ is in units of the hopping, t . The results are averages over eight configurations of disorder (but there is no qualitative difference in the results from different configurations). (d) T_C and T^* vs. J/t for a 6^3 lattice with $x = 0.25$ and $p = 0.4$	34
3.4 Local DOS for three different classes of sites on an 8×8 lattice with $J/t = 2.5$, $T/t = 0.01$, $x \sim 0.2$ and $p = 0.4$. This coupling regime corresponds to the intermediate optimal region, where the impurity band is not fully formed.	36
3.5 Coupling dependence of the conductivity at low temperature in two dimensions. (a) $\sigma(\omega)$ vs. ω for a 10×10 periodic system with 26 spins ($x \sim 0.25$), 10 electrons ($p \sim 0.4$), $T/t = 0.01$, and for different J/ts as shown. (b) $\sigma(\omega)$ vs. ω for a 6^3 periodic system with 54 spins ($x \sim 0.25$), 16 electrons ($p \sim 0.4$), $T/t = 0.01$, and for different J/ts as shown. . . .	37

3.6 (a) Temperature dependence of the optical conductivity of model Eq. (1.1). Shown is $\sigma(\omega)$ vs. ω for a 10×10 periodic system with 26 spins ($x \sim 0.25$), $J/t = 2.5$, $p = 0.3$, and for different temperatures, as indicated. (b) Absorption coefficient $\alpha(\omega)$ spectra for a metallic sample prepared by low temperature annealing. The temperatures from down to top are 300, 250, 200, 150, 120, 100, 80, 60, 40, 20, 10 and 4.2 K. (from Katsumoto <i>et al.</i> [4])	38
3.7 p -dependence of the optical conductivity. Shown is $\sigma(\omega)$, including the Drude weight, vs. ω for a 10×10 lattice, $x = 0.25$, $J/t = 2.5$, $T/t = 0.01$, and different values of p . In the direction of the arrow, p takes the values 0.08, 0.12, 0.20, 0.30, 0.38, and 0.5. <i>Inset</i> : Drude weight, D , vs. fraction of carriers, p .	39
3.8 Geometry used for the calculation of the conductance. The interacting region (lattice) is connected by ideal contacts to semi-infinite ideal leads.	40
3.9 Dependence of the theoretically calculated resistivity, ρ , with temperature in three dimensions. Shown is $\rho = L/G$ vs. T on 4^3 lattices, 16 spins ($x = 0.25$), and 5 carriers ($p = 0.3$) for the J/ts indicated. An average over 20 disorder configurations has been performed in each case. Units are shown in two scales, $ah/(2e^2)$ on the left and $m\Omega\text{cm}$ on the right, with $L = 4$ and assuming $a = 5.6 \text{ \AA}$.	43
3.10 Inverse of the conductance, $1/G$, vs. T calculated on a 10×10 lattice with 26 spins ($x \sim 0.25$), 8 electrons ($p \approx 0.3$), and two values of J/t as indicated. Shown is an average over three disorder configurations. $1/G$ has units of $h/(2e^2)$ in two dimensions.	44
3.11 Magnetization, $ M $, spin-spin correlations, $C(d)$, at maximum and minimum distance, and inverse of the conductance, $1/G$, vs. T on a 12×12 lattice with 22 spins ($x \approx 0.15$), 6 electrons ($p \approx 0.3$), and $J/t=1.0$.	45
3.12 Resistivity of a sample of (Ga,Mn)As with $x = 0.083$ as a function of the temperature. There is a clear peak in the resistivity near the ferromagnetic temperature T_C which is approximately 100K. Samples with different annealing times are shown. (From Ref. [2])	46

3.13	Qualitative explanation of the transport properties of clustered states. Shown are three clusters created ‘by hand’ on an 8×8 lattice and with spin configurations also selected ‘by hand’ to illustrate our ideas. For a (a) FM state at $J/t = 2.5$ and $p = 0.4$, conduction is possible due to the alignment of magnetic moments and the conductance was found to be $G = 2.8(2e^2/h)$. For the “clustered” state regime, two typical configurations (b) and (c) are shown where the conduction channels are broken and as a consequence $G \approx 0$. For the same clustered state but with randomly selected spin orientations (not shown) the conductance is small but finite $G \approx 0.5(2e^2/h)$. The radius of the solid circles represent the local charge density.	47
3.14	Dependence of J/t_{optimal} with x , approximately separating the metal from the insulator (standard notation). At fixed J/t (horizontal solid line), as in experiments, the system should transform from an insulator to a metal with increasing x , in agreement with experiments[2].	49
3.15	Magnetization, $ M $, and inverse conductance, $1/G$, vs. magnetic field, B , on a 12×12 lattice with PBC, $x = 0.15$, $p = 0.3$, $J = 1.0$, and $T/t = 0.01$ (same parameters as in Fig. 3.11). The units of B are Tesla, assuming $g = 2.0$ and $S = 5/2$. The units of $1/G$ are $h/2e^2$	50
4.1	Percolation picture for the formation of the clustered-state regime. (a) Two-dimensional lattice representing randomly-located classical spins as black dots with $x=0.05$. (b) Black areas represent non-zero carrier wave function, assuming a step-function profile for the wave functions with radius equal to 2 sites, as explained in the text. (c) Same as (b) but now showing connected regions (which could in practice correspond to the FM clusters discussed in the text) indicated with different colors.	53
4.2	(a) Crystal structure and (b) phase diagram of $\text{La}_{2-x}\text{Sr}_x\text{CuO}_4$. (From Ref. [5])	54
4.3	MC phase diagram for Eq. (4.1) without disorder at low temperatures, along $V = 1 - J/2$. Six regions are observed: AF, d -SC, stripes, coexisting SC+AF, coexisting stripes+SC, and metal.	60
4.4	(a) MC phase diagram including temperature along “Path 1” (when J reaches 0, the path continues along the horizontal axis). <i>Inset</i> : n vs. μ along Paths 1 and 2. Transitions along Path 1 appear continuous, whereas along Path 2 there are indications of first-order transition. (b) MC phase diagram along “Path 2”. Lattice sizes in all cases are 8×8 and 12×12 . <i>Inset</i> : Spin structure factor $S(\mathbf{q})$ at (π, π) and for incommensurate (IC) momenta.	60

4.5 (a) Plaquette impurity schematic representation. Parameters are chosen such that the blue (black) region favors superconductivity, $(J, V, \mu) = (0.1, 1.0, -1.0)$, with a surrounding white region where $(J, V, \mu) = (0.1, 0.1, -0.5)$ with no order prevailing. The impurity is embedded in a background (red, dark gray) that favors the AF state, $(J, V, \mu) = (1.0, 0.1, 0.0)$. (b) MC phase diagram for model Eq. (4.1) including quenched disorder (lattices studies are 8×8 and 12×12). Shown are T_c and T_N vs. number of impurities (equal to number of holes). The SC and AF regions with short-range order (dashed lines), and T^* as obtained from the PG (dot-dashed line) are also indicated. (c) DOS at points a , b , and c of (a), with a PG.	63
4.6 MC phase diagram (Eq. (4.13)) at $u_{12} = 0.7$. Parameters are $r_1 = -1$, $r_2 = -0.85$, and $u_1 = u_2 = 1$ and disorder strength $W = 0.5$, but the conclusions are not dependent on coupling fine-tuning. <i>Inset</i> : results without disorder ($W = 0$) showing tetracriticality (magenta indicates SC+AF coexistence).	65
4.7 Phase diagram for the Guinzburg-Landau model for $u_{12} = 2$. The clean case ($W = 0$) is bicritical but the addition of disorder ($W = 0.5$) opens a clustered region between the superconductor and the antiferromagnet.	66
4.8 (a) C_{SC}^{\max} vs. Δ_{SC}^{ext} (see text) on a 24×24 lattice, with $u_{12} = 0.7$ and $W = 0.5$, at the five points $a-f$ indicated in Fig. 4.6. A “colossal” effect is observed in a , b , c , and d where the $\Delta_{SC}^{\text{ext}}=0$ state is “clustered”. A much milder (linear) effect occurs far from the SC phase (e and f). MC snapshots are shown at $\Delta_{SC}^{\text{ext}} = 0.0$ (b) and $\Delta_{SC}^{\text{ext}} = 0.2$ (c), both at $T = 0.1$ and $\rho_2 = 0.5$, using the same quenched-disorder configuration. The color convention is explained in the circle (colors indicate the SC phase, while intensities are proportional to $Re(\Delta_i)$). The AF order parameter is not shown. The multiple-color nature of the upper snapshot, reflects a SC phase randomly distributed (<i>i. e.</i> an overall non-SC state). However, a small external field rapidly aligns those phases, leading to a coherent state in (c).	68
4.9 Comparison between the phase diagrams of the single layer system and the two layer system for $u_{12} = 0.7$ and $W = 0.5$ on a 24×24 lattice. . .	69
4.10 (a) T_c vs. N_ℓ for $u_{12} = 0.7$, $\rho_2 = 0.3$, $W = 0.7$, and $24 \times 24 \times N_\ell$ clusters. Shown are results with and without disorder. (b) Experimental T_c (in K) for three HTS families, 2-Tl, 2-Bi, and 1-Tl, as indicated. (From Ref. [6]).	69

4.11	<p><i>Left</i> General phase diagram of two competing phases in the absence of quenched-disorder (or when this disorder is very weak). Thick (thin) lines denote first (second) order transitions. g is some parameter needed to change from one phase to the other. <i>Center</i> With increasing disorder, the temperature range with first-order transitions separating the ordered states is reduced, and eventually for a <i>fine-tuned</i> value of the disorder the resulting phase diagram contains a quantum critical point. In this context, this should be a rare occurrence. <i>Right</i> In the limit of substantial quenched disorder, a window without any long-range order opens at low temperature between the ordered phases. The new scale T^*, remnant of the clean-limit transition, is also shown. (From Ref. [7])</p>	71
5.1	<p>Sketch of the phase diagram indicating the conducting and insulating regions, as obtained by numerical simulation. The dashed area in the paramagnetic phase indicates the crossover region from a mild metallic weak coupling regime to a mild insulating strong coupling regime. . . .</p>	72
C.1	<p>A sketch for the propagation of vector elements. The vertical axis gives the matrix-vector multiplication steps. Circles aligned in the horizontal direction represent lattice sites. Filled circles show sites with non-zero vector elements, and darkness of them schematically illustrates amplitudes of the vector elements. The initial vector gives a localized state at site ν. See also the discussion in §C.2 (from Ref. [8]).</p>	86

ABSTRACT

Several models for materials of much current interest in condensed matter physics have been numerically studied, using unbiased methods, including Monte Carlo simulations and exact treatment of the fermionic trace at finite temperature. It was found that many of these materials share common phenomenological aspects due to the presence of intrinsic inhomogeneities in the form of “clustered states”. Some of these states are highly susceptible to external perturbations. The list includes diluted magnetic semiconductors and high temperature superconducting cuprates among others.

CHAPTER 1

INTRODUCTION

1.1 Diluted Magnetic Semiconductors

Diluted Magnetic Semiconductors (DMSs) are alloys between a non-magnetic semiconductor (*e. g.* GaAs) and a magnetic element, usually manganese (Mn)[1]. Therefore, semiconducting and ferromagnetic properties coexist in these materials. This leads to important technological applications since the charge and the spin of the electron could be used on the same device. At the same time, the underlying solid state system has an enormous interest for basic science.

The possibility of controlling both the charge and the spin of the electron has attracted the interest of researchers for several decades. Magnetic semiconductors, such as Europium chalcogenides and semiconducting spinels, that have a periodic array of magnetic atoms were extensively studied in the late 1960s. However, the crystal structure of such magnetic semiconductors is completely different from that of the most commonly used semiconductors (*e. g.* Si and GaAs) and the crystal growth of those materials is notoriously difficult. On the other hand, diluted magnetic semiconductors (Fig. 1.1), are based on widely known semiconductors like GaAs that can be doped with impurities to change their properties, usually to p - or n -type. II-VI DMSs are DMSs which have a host semiconductor made up of a group II and a group VI element of the periodic table, for example CdTe and ZnS. III-V DMSs are defined in an analogous way and are the most important DMSs studied mainly due to their high Curie temperature (T_C), the highest of all DMSs. In fact, the

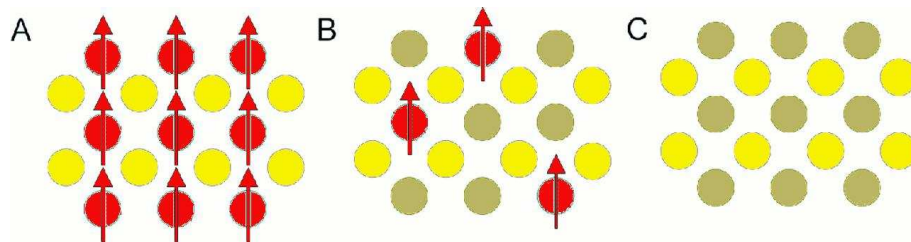


Figure 1.1. Three types of semiconductors: (a) a magnetic semiconductor, which has a periodic array of a magnetic element, (b) a *diluted magnetic semiconductor* (DMS), an alloy between a nonmagnetic semiconductor and a magnetic element and (c) a non-magnetic semiconductor, which contains no magnetic ions (from Ref. [1]).

interest in this field was boosted by the demonstration[9] in 1996 that ferromagnetic transition temperatures in excess of 100 K can be achieved in manganese doped gallium arsenide, (Ga,Mn)As, much higher than the previous record of only 7.5 K for (In,Mn)As[10].

Among the problems in the production of DMS samples is the low solubility of magnetic elements in III-V semiconductors. Since the magnetic effects are often proportional to the concentration of magnetic ions, x , it is necessary to introduce a sizable amount of magnetic moments (a few percent or more) for the material to develop cooperative effects. This requires doping that exceeds the solubility limit of III-V semiconductors. This problem was overcome by low-temperature non-equilibrium molecular beam epitaxial (MBE) growth. MBE is a physical deposition process (basically evaporation) that is carried out in ultra-high vacuum and at substrate temperature typically not exceeding 800 Celsius. Due to the unobstructed molecular flow of the species to be deposited and the chemical cleanliness of the substrate surface, highly controlled growth of very thin epitaxial layers is possible. However, segregation of impurities during MBE growth is an obstacle in obtaining high concentration of magnetic ions. In addition, after the sample is prepared and found to be ferromagnetic below T_C , it is usually necessary to show that ferromagnetism is not caused by the segregation of purely magnetic components,

e. g. MnAs during the fabrication of (Ga,Mn)As, but that Mn has been randomly substituted in the host semiconductor instead. Usually, the quality of the samples is examined by observing the Reflection High Energy Electron Diffraction (RHEED) patterns which help determine if there is any phase segregation[11].

Despite all these difficulties, various DMSs have been fabricated. Higher T_C s have been achieved by annealing. Optimally annealed samples of (Ga,Mn)As with $x > 0.08$ have been found to be ferromagnetic below $T_C = 127$ K [12]. More details will be presented in Section 2.5. Another DMS that could find important applications is gallium nitride, (Ga,Mn)N, with a reported T_C of 500K[13, 14].

1.2 Why study DMSs?

1.2.1 Technological Applications

As mentioned before, the possibility of using the spin as well as the charge of the electron for information processing will find tremendous application in technology and it is the basic idea of spin electronics or *spintronics*. In order for spintronics devices (the most cited example is the transistor of Datta and Das[15]) to work, polarized carriers have to be introduced into a semiconductor, for example using ferromagnetic contacts. However, these devices have not been fabricated yet. The main reason is that it is very difficult to inject net spin polarization directly from a metal into a semiconductor[16], due to the conductance mismatch between the two materials that will cause big suppression of spintronic effects. It is at this point where DMSs would become extremely useful because they would substitute the metallic contact and provide a FM contact that has a conductance similar to that of the semiconductor. Therefore, DMSs have many potential advantages over metals for the fabrication of spintronic devices.

A theory of spin-polarized transport in inhomogeneous magnetic semiconductors has been developed in Ref. [17] similar to the standard theory of charge transport

for $p - n$ junctions. It is likely that these proposed applications for DMS will be realized only if ferromagnetism at room temperature can be achieved and this topic will be revisited later. The focus of this work, however, is on the physics of these ferromagnets and there are indeed important motivations for their study from the point of view of basic science only.

1.2.2 Theoretical Interest

Diluted Magnetic Semiconductors bring together many topics of current interest in condensed matter theory. First, DMSs are correlated electron systems because ferromagnetism is carrier mediated, *i. e.*, the carriers interact with the localized spins of the magnetic ions (Section 1.3). The physics of correlated electrons is without doubt one of the most important areas of research in condensed matter, and many other materials fall in this category, *e. g.* superconductors and manganites. In addition, there is now consensus[18] that the effects of disorder are important to understand the physics of DMSs. The study of disordered systems has an enormous interest *per se*. Of particular importance is to understand the interplay between disorder physics and strong correlations and the role that disorder plays in transport and magnetism.

1.2.3 Motivation for Numerical Studies

There have been a few theoretical studies of DMSs using a mean field approach[19], [20], [21], [22]. They report the dependence of T_C on the carrier density, n , at fixed Mn concentration, x , and calculate the magnetization as a function of the temperature. However, it is well known that mean field theory (MFT) has severe limitations: (i) MFT calculations tend to overestimate the critical temperatures mainly because it neglects thermal fluctuations, (ii) disorder in the Mn positions is not taken into

account within the Mn continuum approximation, which can have a substantial impact on the ferromagnetism.

Theoretical descriptions of DMS materials could be roughly classified in two categories. On one hand, the multi-band nature of the problem is emphasized as a crucial aspect to quantitatively understand these materials[23, 24, 22]. In this context the lattice does not play a key role and a continuum formulation is sufficient. The influence of disorder is considered on average. On the other hand, formulations based on the possible strong localization of carriers at the Mn-spin sites have also been proposed[19, 25]. In this context a single impurity-band description is considered sufficient for these materials. Still within the single-band framework, but with carrier hopping not restricted to the Mn locations, some approaches to the problem have used dynamical mean-field[26] or reduced-basis[27] approximations. An effective Hamiltonian for $\text{Ga}_{1-x}\text{Mn}_x\text{As}$ was derived in the dilute limit and studied in Ref. [28]. All these calculations are important in our collective effort to understand DMSs.

However, it is desirable to obtain a more general view of the problem of ferromagnetism induced by a diluted set of spins and holes. To reach this goal it would be better to use techniques that do not rely on mean-field approximations and, in addition, select a model that has both the continuum and impurity-band formulations as limiting cases. Such an approach would provide information on potential procedures to further enhance T_C and clarify the role of the many parameters in the problem. In addition, these general considerations will be useful beyond the specific details of $\text{Ga}_{1-x}\text{Mn}_x\text{As}$, allowing us to reach conclusions for other DMSs. That is why a Monte Carlo study is strongly needed to obtain a quantitative description of DMS, and to get an accurate phase diagram for these materials. It also fills the gap between the strongly localized and free electron pictures explained before, and it will help test their validity and provide information about the intermediate regime. One of the main goals of this work has been to carry out such Monte

Carlo study and to calculate the critical temperatures and relevant quantities that will contribute to the understanding of the physical properties of DMSs and other correlated electron systems.

1.3 Properties of (III,Mn)V DMS

This section is devoted to the discussion of important properties of (III,Mn)V ferromagnets that have been established experimentally. Detailed reviews of the properties of these materials have been prepared by MacDonald[23], Dietl[22] and a more experimentally oriented discussion can be found in Ref. [3]. Here the focus will be on the observations that are most important in constraining theoretical models.

It is generally accepted that Mn acts as an acceptor when it substitutes for a cation in a III-V semiconductor lattice, leaving a Mn^{2+} ion which has a half-filled d -shell. It is also generally accepted that ferromagnetism occurs in these materials because of interactions between Mn local moments that are mediated by holes. This picture is supported by measurements of the anomalous Hall effect in (Ga,Mn)As [29, 3], since the magnetization extracted from these experiments agrees reasonably well with that obtained from direct SQUID measurements¹ and from magnetic circular dichroism [30]. This shows an intimate connection between carriers and impurity spins. In contrast, in nonmagnetic doped semiconductors, such as phosphorus doped silicon, there has been no evidence for ferromagnetism due to carriers. This carrier-mediated interaction in DMSs has a direct and important implication in the theoretical models that will be described in Section 1.4.

There is strong experimental evidence for the Mn local model. For (Ga,Mn)As the Mn spin is $S = 5/2$ as reported from electron paramagnetic resonance[31] and optical experiments. Therefore, fundamental theories should be able to predict that

¹A SQUID magnetometer consists of two pieces of superconductor formed into a ring by two weak electrical connections so that the circuit acts as a wave function interferometer. SQUIDs are technically important as detectors of magnetic fields, as sensitive voltmeters and as a voltage standard.

magnetic elements act as localized spins and phenomenological theories can safely assume it.

The strength of the coupling between magnetic impurities and holes[32] can be calculated from photoemission measurements [33]. The experimental determination of the exchange coupling J is not conclusive and the precise values are not well known, particularly for Mn concentrations greater than 1%. The values obtained from magnetotransport and photoemission experiments vary from $J = 3.3$ eV to $J = 1.5$ eV.

Another experimentally established fact is that the hole concentration is much smaller than the Mn concentration. In the case of (Ga,Mn)As, if no compensation was present, basic considerations would imply that one hole is added to the system for every Mn substituted in GaAs. However, in reality the ratio of Mn impurity concentration x to hole concentration n , $p = n/x$ is much less than unity. Two possible explanations have been proposed for the compensation in (Ga,Mn)As, the presence of As antisite defects[1] or Mn interstitials [34] that act as donors and tend to passivate substitutional Mn acceptors, reducing the number of holes. This topic is discussed in detail in the literature (for example in Ref. [18]) and the theoretical models that will be proposed here, will consider that compensation already exists in the system without dealing with the detailed mechanisms. The experimental determination of the hole density is not trivial. It is usually obtained from the ordinary Hall coefficient [1, 3], measured in a strong external field to saturate the anomalous Hall effect. But even for large fields the Hall resistivity is not linear in field. However, careful analysis finds agreement with other methods used to determine the hole concentration, *e. g.* Raman scattering intensity [35].

It is also worth noting that the magnetization observed experimentally at low temperatures is much smaller than the theoretical maximum calculated assuming $S = 5/2$, indicating that not all spins align. The total magnetization is dominated

by the impurities because of compensation and since the impurity spins are larger than the carrier spins.

An anomalous shape of the magnetization curve, $M(T)$, is observed experimentally in DMSs[36, 10, 37, 30, 38, 2, 39, 40]. In insulating samples the magnetization curve is often *concave* over a broad temperature range[2, 39]. In metallic samples the magnetization curve is usually nearly linear over a broad range[30, 38]. These results are in striking contrast to the Brillouin-function-like behavior predicted by the mean-field theories[41] and observed in most insulating and metallic ferromagnets. The origin of the anomalous magnetization curve is most likely due to disorder and low carrier concentration. Optimally annealed or high quality samples show a much less deviation from Brillouin-function-like behavior[40].

It has been shown that both T_C and the shape of the magnetization depend on post-growth annealing of the samples. This implies that the chemical changes that possibly occur during annealing affect the physical properties of these materials. Moreover, it has been found that both metallic and insulating samples are ferromagnetic. In (Ga,Mn)As and possibly other DMSs, there is a metal-insulator transition between insulating samples with small manganese concentration and metallic samples with larger concentration. Insulating behavior is characterized by a diverging resistivity for $T \rightarrow 0$, indicating localization of carriers. Conversely, in metallic samples the resistivity decreases and eventually saturates for $T \rightarrow 0$. The term “metal-insulator” transition will also be used in this work to refer to the observed maximum of the resistivity around T_C that occurs at certain concentrations.

All these observations indicate the importance of the effects of disorder and of dilution, and, therefore, they will have to be taken into account in the theoretical description of DMS compounds. It can be seen also that there is much similarity between the ferromagnetism of DMS materials and that of lanthanides and actinides and their compounds, in which f-electron moments are coupled by d-band itinerant electrons. There are also similarities between these materials and the manganite

compounds that have been extensively studied[42], in part because of the large increase in resistance that occurs when T exceeds the critical temperature which is related to the so-called colossal magnetoresistance effect. One of the differences between manganites and DMS is, however, that in DMS the local moments appear on only a small fraction of atomic sites, arranged randomly and the itinerant electron density is also low, as already mentioned. The physics of DMSs is in a sense intermediate between that of rare earth magnets and that of manganites in that the spin-splitting of itinerant electron bands due to their exchange coupling with local moments is comparable to their Fermi energies, rather than being much smaller than band Fermi energies as in the rare earth or larger as in the case of manganites.

1.4 Theoretical Models

Macroscopic effects, such as ferromagnetism, are collective effects caused by the interaction between carriers, atoms and ions that compose the material under study. If it were possible to do so, the microscopic theory would be solved by treating the many-electron Schrödinger equation directly, given the position of all the nuclei. Usually this approach is impossible because of the macroscopic number of interacting electronic degrees of freedom. Instead models are constructed using a combination of approximation of exact theories and phenomenological modeling.

A treatment that is usually successful in many-body physics is spin-density-functional (SDF) theory, where many-body effects appear in contributions to effective independent-particle Hamiltonians by means of exchange-correlation potentials. SDF theory is a first principles approach which has no phenomenological parameters. In the context of DMSs, SDF theory has been applied to (III,Mn)V compounds [43, 32, 44]. These calculations have been performed using the local density approximation (LDA) of SDF theory, an approximation that is not reliable when local moments are formed as is the case for (III,Mn)V DMS. For this reason, these

theories predict that majority spin d -electrons of a Mn atom substituted on a cation site of GaAs lie near the Fermi energy, rather than lying well below the Fermi energy as would be the case if the half-filled d -shell formed a $S = 5/2$ local moment. As explained in Section 1.3, this contradicts experiment. Similar results have been obtained in coherent potential approximation (CPA) band-structure calculations[45]. Despite this disagreement with experiment, it is very likely that useful information on the electronic properties of DMSs can be reliably obtained from SDF related calculations, especially by the LDA+U method which has been developed to mitigate the deficiencies of SDF theory[46].

The work presented here, however, is based on a more phenomenological model, which tries to include all the interactions that have been shown to be relevant by experiments. The next section discusses what these relevant interaction terms should be and the development of the theoretical model to be used. The limitations of the model and the possibility of future improvements are also addressed. Section 1.5 explains the methods used for extracting information from the models.

1.4.1 Diluted Kondo Lattice Model

There are two degrees of freedom in the DMS problem described here: (i) the local magnetic moments corresponding to the 5 electrons in the d -shell of each Mn impurity, with a total spin $5/2$, and (ii) the itinerant carriers produced by the Mn impurities. Because of compensation (Section 1.3), the actual concentration of carriers is smaller than that of Mn impurities. Therefore, in the present study, both the density of Mn atoms, x , and the density of carriers, n , are treated as independent input parameters. Moreover, the ratio $p = n/x$ is defined, which is a measure of the compensation of the system, *e. g.* for $p = 0$ the system is totally compensated and for $p = 1$ there is no compensation.

The Hamiltonian of the system in the one-band approximation can be written as:

$$\hat{H} = -t \sum_{\langle ij \rangle, \sigma} \hat{c}_{i\sigma}^\dagger \hat{c}_{j\sigma} + J \sum_{i \in I} \vec{S}_i \cdot \vec{\sigma}_i, \quad (1.1)$$

where $\hat{c}_{i\sigma}^\dagger$ creates a carrier at site i with spin σ . The carrier-spin operator interacting antiferromagnetically with the localized Mn-spin \vec{S}_i is $\vec{\sigma}_i = \sum_{\alpha, \beta} \hat{c}_{i\alpha}^\dagger \vec{\sigma}_{\alpha, \beta} \hat{c}_{i\beta}$. Through nearest-neighbor hopping, the carriers can hop to *any* site of the square or cubic lattice. The interaction term is restricted to a randomly selected but fixed set of sites, denoted by I .

The form of Eq. (1.1) is based on a model proposed by C. Zener [47] to explain carrier mediated ferromagnetism in the context of manganites. Later it was shown that the Kondo lattice model, Eq. (1.1) when the set I is the whole lattice, can be mapped into the periodic Anderson model [48] in the so called kondo regime. The periodic Anderson model [49] describes heavy fermions by considering the hybridization of two types of orbitals for electrons. The Kondo lattice model describes the effective physics where one type of electrons are considered to be localized spins. These interact with the conduction electrons through the coupling J . This model is believed to at least qualitatively describe important aspects of the rich physics of these systems [23]. Single impurity models [50] [51] are not directly relevant in the context of DMSs since the impurity concentration is greater than the carrier concentration. Therefore, the present model can be regarded as an interpolation between the single impurity model and the kondo lattice models.

The carriers are considered to be electrons and the kinetic energy term describes a conduction band. However, in $\text{Ga}_{1-x}\text{Mn}_x\text{As}$ the carriers are holes and the valence band has to be considered instead. Although the latter is more complicated, the simplified treatment followed here yields the same results for both cases for a one-orbital model [52, 19, 53, 54, 25].

The local spins are assumed to be classical which allows the parametrization of each local spin in terms of spherical coordinates:

$$\vec{S}(\theta_i, \phi_i) = (\sin \theta_i \cos \phi_i, \sin \theta_i \sin \phi_i, \cos \theta_i). \quad (1.2)$$

Rigorous and exact results for this model, especially for the concentrated case (*i. e.*, when the subset I is the complete lattice itself) are presented in Appendix A. When J is small the present model can be mapped into a Heisenberg-like model, which depending on the parameters might have long range interactions. This is because, even though Hamiltonian Eq. (1.1) is a complicated functional of the Mn spins $\vec{S}(\theta_i, \phi_i)$, it has a global rotational symmetry. The first term of the low coupling expansion is $J_{eff}(|i - j|)\vec{S}_i \cdot \vec{S}_j$. This model is usually called an RKKY model[55] and is related to the Heisenberg Hamiltonian. Therefore, in Appendix A, the most important rigorous results known for Heisenberg and Ising models are also summarized.

Formulas needed to carry out a Monte Carlo study are described in this section, following Ref. [42]. The partition function can be written as:

$$Z = \prod_i^N \left(\int_0^\pi d\theta_i \sin \theta_i \int_0^{2\pi} d\phi Z_g(\{\theta_i, \phi_i\}) \right), \quad (1.3)$$

where $Z_g(\{\theta_i, \phi_i\}) = \text{Tr}(e^{-\beta\hat{K}})$ is the partition function of the fermionic sector, $\hat{K} = \hat{H} - \mu\hat{N}$, \hat{N} is the number operator, and μ is the chemical potential.

In the following, an hypercubic lattice of dimension D , length L , and number of sites $N = L^D$ will be considered. Since \hat{K} is a Hermitian operator, it can be represented in terms of a Hermitian matrix which can be diagonalized by an unitary matrix U such that

$$U^\dagger K U = \begin{pmatrix} \epsilon_1 & 0 & \dots & 0 \\ 0 & \epsilon_2 & \dots & 0 \\ \vdots & \vdots & \ddots & \vdots \\ 0 & 0 & \dots & \epsilon_{2N} \end{pmatrix}. \quad (1.4)$$

The basis of the one-electron sector (Appendix A) in which the matrix K is diagonal is given by the eigenvectors $u_1^\dagger|0\rangle, \dots, u_{2N}^\dagger|0\rangle$, where the fermionic operators used in this basis are obtained from the original operators through $u_m = \sum_{j\sigma} U_{m,j\sigma}^\dagger c_{j\sigma}$, with m running from 1 to $2N$.

Defining $u_m^\dagger u_m = \hat{n}_m$ and denoting by n_m the eigenvalues of \hat{n}_m , the trace can be written

$$\begin{aligned} \text{Tr}_g(e^{-\beta\hat{K}}) &= \sum_{n_1, \dots, n_{2N}} \langle n_1 \dots n_{2N} | e^{-\beta\hat{K}} | n_1 \dots n_{2N} \rangle \\ &= \sum_{n_1, \dots, n_{2N}} \langle n_1 \dots n_{2N} | e^{-\beta \sum_{\lambda=1}^{2N} \epsilon_\lambda n_\lambda} | n_1 \dots n_{2N} \rangle, \end{aligned} \quad (1.5)$$

since in the $\{u_m^\dagger | 0\rangle\}$ basis, the operator \hat{K} is $\sum_\lambda \epsilon_\lambda \hat{n}_\lambda$, and the number operator can be replaced by its eigenvalues. The exponential is now a number, and it is equivalent to a product of exponentials such that

$$Z_g = \sum_{n_1} \langle n_1 | e^{-\beta\epsilon_1 n_1} | n_1 \rangle \dots \sum_{n_{2N}} \langle n_{2N} | e^{-\beta\epsilon_{2N} n_{2N}} | n_{2N} \rangle, \quad (1.6)$$

which can be written compactly as

$$Z_g = \prod_{\lambda=1}^{2N} \text{Tr}_\lambda(e^{-\beta\epsilon_\lambda n_\lambda}). \quad (1.7)$$

Since the particles are fermions, the occupation numbers are either 0 or 1, and the sum in Eq. (1.6) is restricted to those values,

$$Z_g = \prod_{\lambda=1}^{2N} \sum_{n=0}^1 e^{-\beta\epsilon_\lambda n} = \prod_{\lambda=1}^{2N} (1 + e^{-\beta\epsilon_\lambda}). \quad (1.8)$$

Thus, combining Eq. (1.3) and Eq. (1.8), Z is obtained as

$$Z = \prod_i^N \left(\int_0^\pi d\theta_i \sin \theta_i \int_0^{2\pi} d\phi_i \right) \prod_{\lambda=1}^{2N} (1 + e^{-\beta\epsilon_\lambda}), \quad (1.9)$$

which is the formula used in the simulations.

1.4.2 Band structure of III-V semiconductors

Although the most important physical properties can be obtained with the one band approximation of Eq. (1.1), the actual band structure of semiconductors and in particular those belonging to the III-V series is more complicated.

First, the lattice structure of GaAs is zincblende [56] as shown in Fig. 1.2. It consists of two interpenetrating face-centered cubic Bravais lattices, displaced along the body diagonal of the cubic cell by one quarter the length of the diagonal. In this arrangement Ga and As atoms occupy each sublattice respectively. The corresponding band structure is shown in Fig. 1.3 and very generally is composed of a conduction band and a number of valence bands. The band energy will vary in proportion to k^2 near the conduction-band minimum and, for the zincblende structure, must by symmetry be independent of the direction of \mathbf{k} . Then, near the conduction band minimum,

$$E_k = E_g + \frac{\hbar^2 k^2}{2m_c}, \quad (1.10)$$

where m_c is called the *effective mass* of an electron. The dimensionless parameter m_c/m is adjusted to give the correct energy dependence for each material and can vary greatly from material to material. The experimental value for GaAs is $m_c/m = 0.066$.

Similarly, the energy varies quadratically with k near the maximum in the valence band. This would correspond to a negative effective mass in Eq. (1.10), but as is well known, a suitable change of variables allows for the description of empty states at the top of the band as positively charged particles (holes) with positive mass[57]. However, the region at the top of the valence band presents other complications, which are apparent in Fig. 1.3. There are three bands. The one with the greatest curvature is called the *light-hole* band because the magnitude of its effective mass is small. There are also two *heavy-hole* bands. Spin-orbit coupling splits off one these otherwise degenerate heavy-hole bands. The heavy-hole band that is split away then becomes mixed with the light-hole band to give the final energy bands shown in Fig. 1.3, where the magnitude of the spin-orbit splitting, $E_{s.o.}$, is also indicated. For GaAs, $E_{s.o.} = 0.34\text{eV}$, although it strongly depends on the material and it is only 0.02eV in GaN.

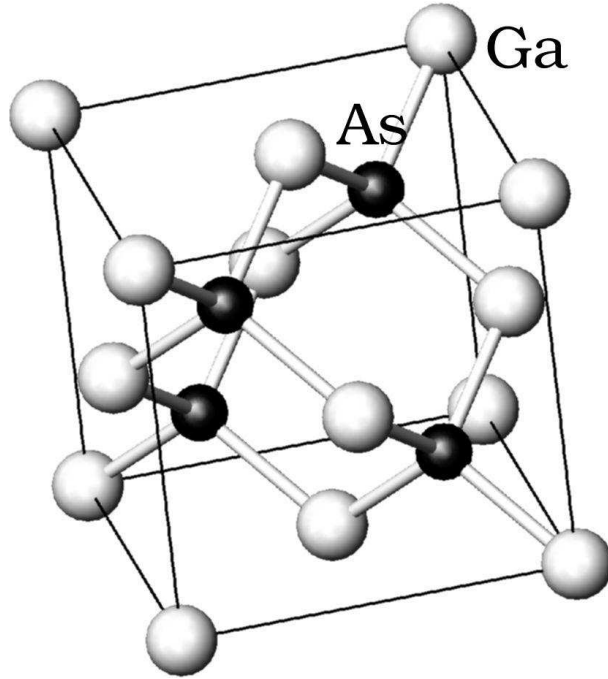


Figure 1.2. Lattice structure of GaAs. White and black spheres represent the location of Ga and As atoms respectively.

In addition, when Mn is substituted for Ga to form the DMS (Ga,Mn)As, new states appear above the valence band, and these states, usually referred to as impurity states, are taken into account in Eq. (1.1), and discussed in Section 3.1.

1.4.3 Coulomb interaction and direct exchange

Besides the use of a single band, there are other approximations in the model described here. First, the Hubbard U/t is not included. This is justified based on the low-carrier concentration of the problem, since in this case the probability of double occupancy is small. In addition, Mn-oxide investigations[42, 58, 59] have shown that an intermediate or large J coupling acts similarly as U/t , also suppressing double occupancy. A nearest-neighbors antiferromagnetic coupling between the Mn spins is not included. Again, this is justified as long as x is small because the probability of finding two neighboring sites both having a spin is equal to x^2 . Finally, potential

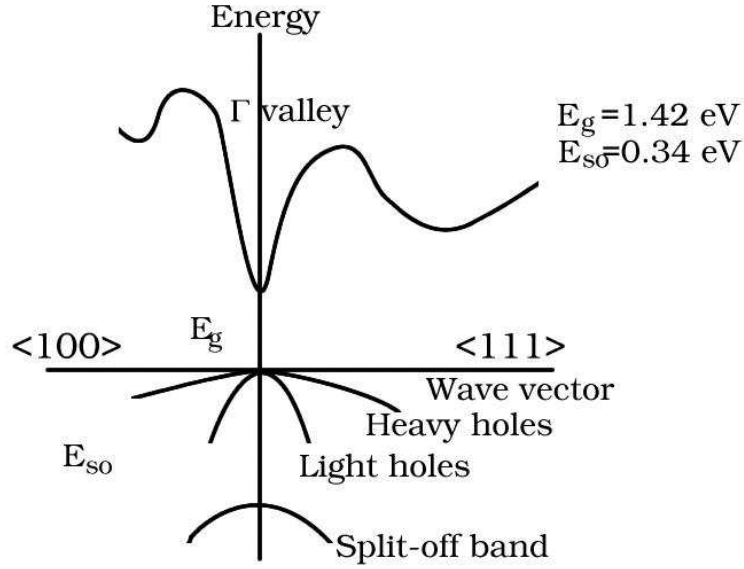


Figure 1.3. Sketch of the energy bands of GaAs.

disorder is also neglected (together with the spin, the Mn sites should in principle act as charge trapping centers). Nevertheless the qualitative results that will be presented in the following chapters should be valid regardless of the specific origin of disorder and localization.

1.5 Monte Carlo Methods

The theory described in the previous section cannot in general be solved exactly. As explained in §1.2.3, many approximations to the models for DMSs have been studied (mean field, SDF, CPA). However, the method to extract information from the theory that will be used in this work is based on Monte Carlo algorithms, that have the advantage that the error made in the calculations can be calculated with the desired precision.

The expression “Monte Carlo method” is actually very general. Monte Carlo (MC) [60, 61] methods are stochastic techniques – meaning that they are based on the use of random numbers and probability statistics to solve the problem, basically

integration. Monte Carlo is now used routinely in many diverse fields, and it is particularly useful in the field of strongly correlated electrons.

1.5.1 Monte Carlo Simulation

The integral over the angular variables in Eq. (1.9) can be performed using a classical Monte Carlo simulation[62]. The eigenvalues must be obtained for each classical spin configuration using library subroutines (LAPACK and its variants were used in this work). Finding the eigenvalues is the most time consuming part of the numerical simulation. It is important to remark that the integrand is positive and, therefore, “sign problems” in which the integrand of the multiple integral under consideration can be non-positive, are fortunately not present in our study.

Although the formalism is in the grand-canonical ensemble, the chemical potential was adjusted to give the desired carrier density, n . To do so, the equation $n(\mu) - n = 0$ was solved for μ at every Monte Carlo step by using the Newton-Raphson method [63]. This technique proved very efficient in adjusting with precision the desired electronic density.

Usually, between 2000 to 5000 Monte Carlo iterations were used to let the system thermalize, and then 5000 to 10,000 additional steps were carried out to calculate observables, measuring every 5 of these steps to reduce autocorrelations.

Since for fixed parameters there are many possibilities for the random location of Mn impurities, results are averaged over several of these disorder configurations. Approximately 10 to 20 disorder configurations were generally used for small lattices (4^3 and 10×10) and 4 to 8 for larger lattices (6^3 and 12×12). The inevitable uncertainties arising from the use of a small number of disorder configuration does not affect in any dramatic way the results that will be presented below. This is deduced from the analysis of results for individual disorder samples. Indeed, the qualitative trends are present in all of these configurations.

1.5.2 Observables

Quantities that depend on the Mn degrees of freedom (θ_i and ϕ_i in the previous formalism) are calculated simply by averaging over the Monte Carlo configurations. Obviously any observable that does not have the continuous symmetry of the Hamiltonian will vanish over very long runs. Thus, it is standard in this context to calculate the absolute value of the magnetization, $|M| = \sqrt{\sum_{ij} \vec{S}_i \cdot \vec{S}_j}$, as opposed to the magnetization vector. Another useful quantity is the spin-spin correlation, defined by:

$$C(x) = \frac{1}{N(x)} \sum_y \vec{S}_{y+x} \cdot \vec{S}_y \quad (1.11)$$

where $N(x)$ is the number of non-zero terms in the sum. The correlation at a distance d is averaged over all lattice points that are separated by that distance, but since the system is diluted, the quantity must be normalized to the number of pairs of spins separated by d , to compare the results for different distances.

The observables that directly depend on the electronic degrees of freedom can be expressed in terms of the eigenvalues and eigenvectors of the Hamiltonian matrix \hat{K} [42]. The density of states (DOS), $N(\omega)$, is simply given by $\sum_\lambda \delta(\omega - \epsilon_\lambda)$. However, the majority and minority DOS, $N_\uparrow(\omega)$ and $N_\downarrow(\omega)$, were also calculated in this study and since the corresponding formulas are not very common in the literature, they are presented here. $N_\uparrow(\omega)$ indicates the component that aligns with the local spin, *i. e.*, $N_\uparrow(\omega)$ is the Fourier transform of $\sum_i \langle \tilde{c}_{i\uparrow}^\dagger(t) \tilde{c}_{i\uparrow}(0) \rangle$, where $\tilde{c}_{i\uparrow} = \cos(\theta_i/2)c_{i\uparrow} + \sin(\theta_i/2)e^{-i\phi_i}c_{i\downarrow}$. Then:

$$\begin{aligned} N_\uparrow(\omega) = & \sum_\lambda \delta(\omega - \epsilon_\lambda) \left[\sum_i U_{i\uparrow,\lambda}^\dagger U_{\lambda,i\uparrow} \cos^2(\theta_i/2) + U_{i\downarrow,\lambda}^\dagger U_{\lambda,i\downarrow} \sin^2(\theta_i/2) + \right. \\ & \left. \left(U_{i\uparrow,\lambda}^\dagger U_{\lambda,i\downarrow} \exp(-i\phi_i) + U_{i\downarrow,\lambda}^\dagger U_{\lambda,i\uparrow} \exp(i\phi_i) \right) \times \right. \\ & \left. \cos(\theta_i/2) \sin(\theta_i/2) \right], \end{aligned} \quad (1.12)$$

where for sites i without an impurity $\theta_i = \phi_i = 0$ is assumed. A similar expression is valid for $N_{\downarrow}(\omega)$. The optical conductivity was calculated using the expression:

$$\sigma(\omega) = \frac{\pi(1 - e^{-\beta\omega})}{\omega N} \int_{-\infty}^{+\infty} \frac{dt}{2\pi} e^{i\omega t} \langle \vec{j}_x(t) \cdot \vec{j}_x(0) \rangle, \quad (1.13)$$

where the current operator is:

$$\vec{j}_x = ite \sum_{j\sigma} (c_{j+\hat{x},\sigma}^\dagger c_{j,\sigma} - H.c.), \quad (1.14)$$

with \hat{x} the unit vector along the x -direction. For $\omega \neq 0$, $\sigma(\omega)$ can be written as:

$$\begin{aligned} \sigma(\omega) = & \sum_{\lambda \neq \lambda'} \frac{\pi t^2 e^2 (1 - e^{-\beta\omega})}{\omega N} \times \\ & \frac{|\sum_{j\sigma} (U_{j+\hat{x}\sigma,\lambda}^\dagger U_{\lambda',j\sigma} - U_{j\sigma,\lambda}^\dagger U_{\lambda',j+\hat{x}\sigma})|^2}{(1 + e^{\beta(\rho_\lambda - \mu)})(1 + e^{-\beta(\rho_{\lambda'} - \mu)})} \times \delta(\omega + \rho_\lambda - \rho_{\lambda'}). \end{aligned} \quad (1.15)$$

Both $N(\omega)$ and $\sigma(\omega)$ were broadened using a Lorentzian function as a substitute to the δ -functions that appear in Eqs. 1.12 and 1.15. The width of the Lorentzian used was $\epsilon = 0.05$ in units of the hopping, t .

The optical conductivity in d dimensions obeys the sum rule:

$$\frac{D}{2} = \frac{\pi e^2 \langle -\hat{T} \rangle}{2Nd} - \int_{0^+}^{\infty} \sigma(\omega) d\omega, \quad (1.16)$$

where D is the Drude weight and \hat{T} is the kinetic energy:

$$-\hat{T} = t \sum_{\langle ij \rangle, \sigma} (c_{i\sigma}^\dagger c_{j\sigma} + H.c.). \quad (1.17)$$

Although the Drude weight gives the conductivity properties of the lattice, its error can be large because of finite size effects. Therefore, the ‘‘mesoscopic’’ conductance was also calculated in order to gather additional information. The details are explained in Section 3.3.

1.5.3 Polynomial Expansion Methods

MC simulations have been found very suitable to extract information from the theoretical models for strongly correlated electron systems. However, MC studies are

affected by finite-size effects since the system size is limited, due to an increase of the computational complexities and hence CPU time increases with system size. To properly study thermodynamic properties of the model, it is necessary to perform extrapolations to the thermodynamic limit by means of finite size scaling. For the algorithm that uses exact diagonalization presented previously, the CPU time scales as $O(N^4)$ where N is the size of the system (number of lattice sites). This is because one diagonalization scales as $O(N^3)$ and at every MC step every spin on the lattice is flipped which implies an extra $O(N)$. It is remarkable that diagonalization is one of the most complex operations in linear algebra and it cannot take advantage of the sparseness of the Hamiltonian matrix, which is the case in DMS systems.

In order to overcome this difficulty, improved algorithms have been proposed to reduce the computational complexity of the calculation. A Polynomial Expansion Method (PEM) was developed in Ref. [64] with a complexity that is proportional to $O(N^3)$. A newer algorithm that extends the PEM, has been proposed [8], which by truncating the matrix products that appear in the expansion in a controlled way, reduced the complexity to $O(N)!$ Because they have not been discussed extensively in the literature and because these algorithms have been tested and used in the work that will be presented in the following chapters, they are described in more detail in Appendices B and C.

CHAPTER 2

PHASE DIAGRAM

2.1 Magnetic Properties

One of the objectives of the numerical study is to obtain the phase diagram for Hamiltonian Eq. (1.1), and particularly to understand the dependence of T_C on the many variables of the problem. It is very likely that these simulations will help in determining how to prepare samples with higher T_C . Simulations were first carried out for parameters that apply to $\text{Ga}_{1-x}\text{Mn}_x\text{As}$.

Typical results for small and intermediate J/t of our large-scale computational effort are in Fig. 2.1. It was found that even with just the 4^3 cluster, T_C could be estimated fairly well, as will be shown. This is important to simplify the computational search for optimal T_C s varying many parameters. In Fig. 2.1a, the temperature where a deviation from the high- T limit is found is slightly larger than the $T_C/t = 0.04$ obtained from larger clusters. Studying the spin-spin correlation at the largest available distance, a nonzero value characteristic of an ordered ferromagnetic (FM) state was obtained at T just below 0.04. Fig. 2.1b provides another example of our comprehensive T_C study, using just two cluster sizes at the $x-p$ location of the highest T_C , at fixed $J/t = 2$. It can be seen that the use of only 4^3 and 6^3 clusters provides the same value of $T_C \sim 0.08t$ within the statistical error.

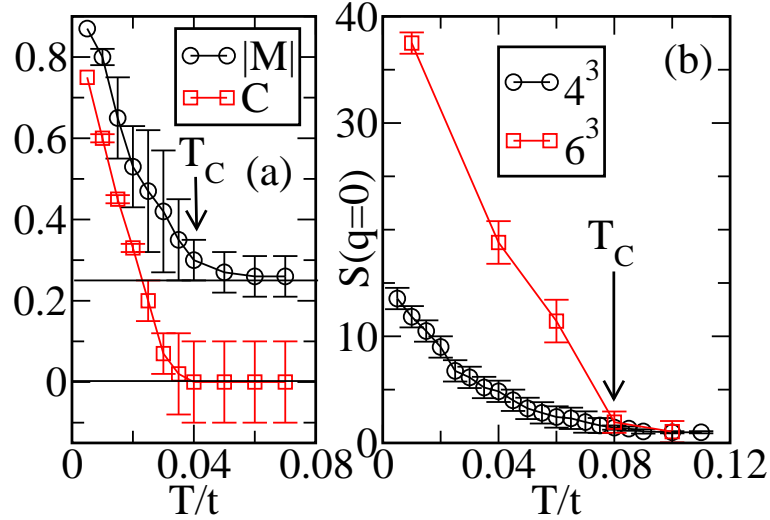


Figure 2.1. (a) $|M|$ (circles) and spin-spin correlation C at maximum distance (squares) vs. T , on a 4^3 cluster, at $J/t = 1.0$, $x = 0.25$, and $p = 0.4$. The 0.25 horizontal line indicates the value of $|M|$ at $T = \infty$. (b) $S(q = 0)$ vs. T , at $J/t = 2.0$, $x = 0.25$, and $p = 0.4$ using 4^3 (circles) and 6^3 (squares) lattices. In all cases T_C is indicated.

2.2 Carrier Concentration

To understand the qualitative T_C trends, first consider the simplest case: the p dependence at fixed J and x . Using the results in Fig. 2.2a contrasted against Fig. 2.1a (same lattice size) T_C is found to increase by a factor of approximately 2, when p varies from 0.1 to 0.4. However, this tendency does not continue with increasing p , since at $p = 1$ or beyond, a ferromagnetic state is not formed: the Pauli principle reduces drastically the carrier kinetic energy, leading instead to an antiferromagnetic state. An example at $p = 3$ and on an 8×8 cluster (results are qualitatively similar in two and three dimensions) is in Fig. 2.2b, where the oscillations in the spin correlations indicate staggered order. In general, the optimal p is close to 0.5, between the hole empty $p = 0$ and saturated $p = 1$ limits, as also found with dynamical mean field theory (DMFT) [20]. A similar result occurs in Mn-oxide models, recovered from Eq. (1.1) at $x = 1$. In that context, investigations at large Hund coupling, the analog of J for DMSs, have shown that $p = 0.5$ optimizes

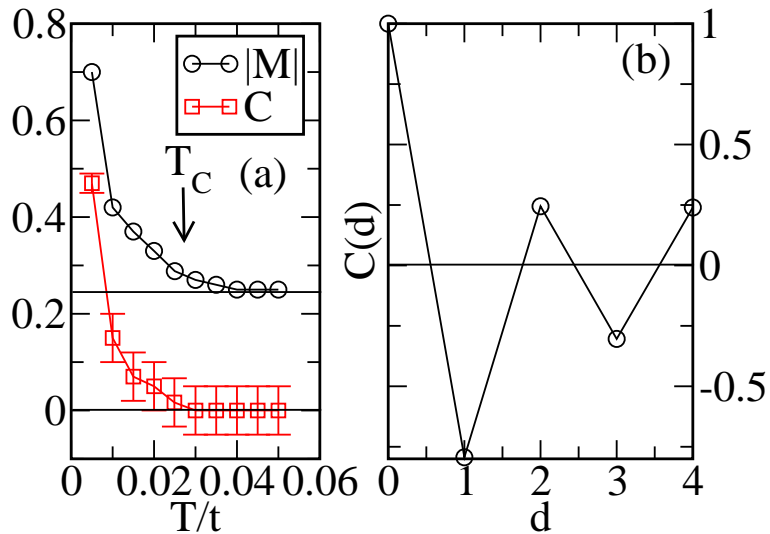


Figure 2.2. (a) Magnetization $|M|$ (circles), and spin-spin correlation at maximum distance C (squares) vs. T , at $J/t = 1.0$, $x = 0.25$, and $p = 0.1$, using a 6^3 cluster. (b) $C(d)$ vs. d at $p \sim 3.0$, $x = 0.25$, $J/t = 1.0$, and $T/t = 0.005$, using an 8^2 cluster. The oscillations indicate an AF state.

T_C to a number between $0.11t$ and $0.13t$ [42, 65], likely an *upper-bound* on the T_C that could be achieved with Eq. (1.1).

2.3 Coupling Dependence

Consider now the J/t dependence of T_C . The mean field (MF) approximation suggests $T_C^{MF} \propto J^2$ [20]. However, this does not hold when more accurate methods are used in the calculations. In fact, for $J/t \rightarrow \infty$ and a Mn dilute system, the holes are trapped in Mn-sites, reducing drastically the conductance (Section 3.3) and T_C . Small FM clusters of spins are formed at a temperature scale T^* , but there is no correlation between them, leading to a global vanishing magnetization [54]. These results *cannot* be obtained within a mean-field approximation. The large- J/t ideas can be tested in our MC simulation by monitoring the short- and long-distance behavior of the spin-spin correlations $C(d)$. In a “clustered” state (large J/t), $C(d)$ at the shortest distance can be robust at $T < T^*$, but $C(d)$ at the largest distance vanishes because of the uncorrelated nature of the magnetism between independent

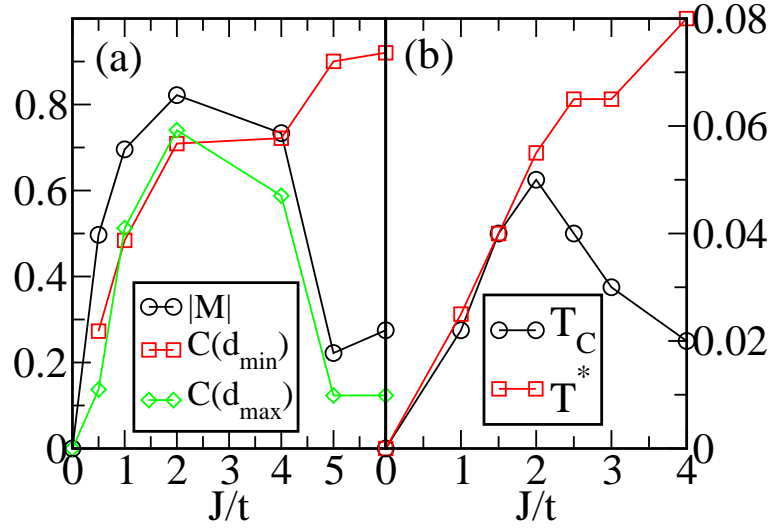


Figure 2.3. (a) $|M|$ (circles), spin-spin correlation at minimum distance $C(d_{min})$ (squares), and at maximum distance $C(d_{max})$ (diamonds) vs. J/t , for a 4^3 cluster at $x = 0.25$, $p = 0.1$, and $T/t = 0.005$. (b) MC phase diagram in 2D varying J/t , at fixed x and p . At large J/t , a broad scale T^* corresponds to the formation of uncorrelated clusters. T_C transition temperature, defined as the T where FM correlations develop at the largest distance in the clusters used. At small J/t , those temperatures are similar. The optimal J/t is intermediate between itinerant and localized regimes.

clusters (see Fig. 2.3a). This subtle effect explains the incorrect MF prediction, since $T_C^{mf} \sim T^*$, which grows with J/t . (see also Fig. 2.3b). Since both in the $J/t \rightarrow 0$ and $J/t \rightarrow \infty$ limits T_C is suppressed, an *optimal* $J/t|_{opt}$ must exist where T_C is maximized. Simulation results as in Fig. 2.3 indicate that the optimal J/t value is close to 2. This phenomenon is not captured in itinerant[66] or localized[19, 52] limits nor by DMFT [20], but it is observed in the present generic MC simulations.

A “toy” model will now be introduced that will help in the understanding of the existence of a $J/t|_{opt}$. A finite lattice with *two* Mn spins and *one* carrier will be considered at $T = 0$. For any fixed angle θ between the Mn-spins, assumed coplanar, the energy can be calculated exactly. The ground state of this $p = 0.5$ system is always at $\theta = 0$, corresponding to a FM configuration, while the energetically less favorable state is $\theta = \pi$, corresponding to an antiferromagnetic configuration. Their energy difference ΔE (Fig. 2.4) is a crude estimation of the FM state stability. An

optimal J/t is found in all dimensions, with stability increasing with the coordination number. In Fig. 2.4 results for 1, 2 and 3 dimensions are indicated and the distance between the 2 Mn spins is such that the associated effective $x \sim 0.1$ is the same in all cases. The optimal J/t of this “toy” example is larger only by a factor 2, compared with the realistic value of Fig. 2.3b. The effects of localization are understood measuring the electronic density $n(i)$ or wave function $|\Psi_i|^2$ of the same problem on a chain as depicted in Fig. 2.5. At small J/t , the delocalization manifests in the nearly uniform density, leading to weak FM. At large J/t , strong localization decouples the Mn-spins, producing again weak FM. In this strongly localized limit, the energy does not depend on θ . However, there is an optimal value where the system takes advantage of J/t , but also allows for a nonzero effective coupling among separated classical spins, leading to a stronger FM.

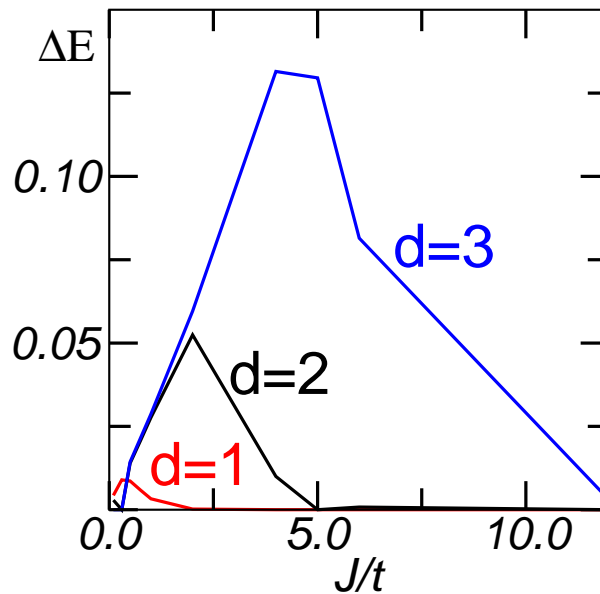


Figure 2.4. $\Delta E = E(\theta = \pi) - E(\theta = 0)$ vs. J/t calculated exactly on finite but large lattices at $T = 0$ for a system of 2 Mn-spins and 1 electron, where θ is the relative angle between the Mn-spins.

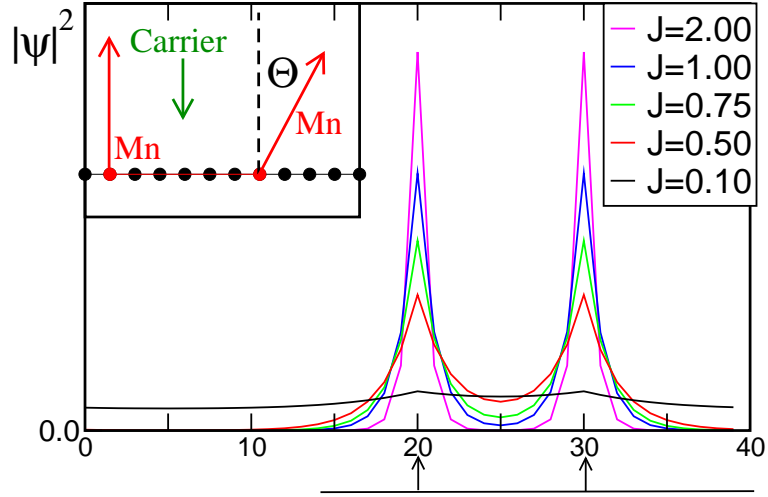


Figure 2.5. Exact $T=0$ local carrier density, for 1 carrier and 2 parallel spins at sites 10 and 20, of a 30-site chain, varying J/t .

2.4 Local Spin Concentration

In this section, the x dependence of T_C will be studied. For simplicity, $J/t = 2$ will be used, which is both close to optimal and experimentally realistic. For $J/t \gg 1$ values, the optimal density for T_C would be $x = 1$, as in manganites. Fig. 2.6a shows T_C vs. x at $p \sim 0.4$, and for two reasonable values of t . Experiments [1, 3] indicate a linear growth of T_C up to 5% (shown), as in the numerical results. The slope of T_C vs. x is in remarkable agreement with MC predictions, in a reasonable range of t . In samples with $x > 0.05$, a reduction of T_C had been originally reported in experiments [1, 3]. However, data gathered with an optimized annealing treatment[67] indicate that T_C remains constant. This is still in contradiction with the linearly growing T_C of the MC results, but it suggests that even more refined thin-films may continue increasing T_C with increasing x . The MC results unambiguously indicate linear behavior up to $x \sim 0.25$ (Fig. 2.6a). To the extent that our model describes DMSs quantitatively, higher values of T_C could be expected experimentally.

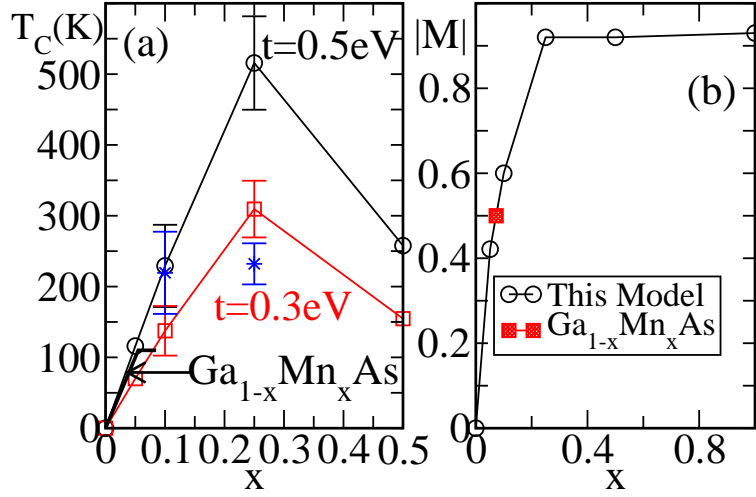


Figure 2.6. (a) T_C vs. x for $\text{Ga}_{1-x}\text{Mn}_x\text{As}$ [2] (thick line), and for model Eq. (1.1) using $t = 0.3$ eV (squares) and $t = 0.5$ eV (circles). In both cases, $p \sim 0.4$ and $J/t = 2.0$. Typical error bars are shown. Stars are results for $p \sim 0.5$, $J/t = 1$, and $t = 0.5$ eV. (b) Magnetization $|M|$ vs. x for model Eq. (1.1) (circles) at $T/t = 0.005$, $J/t = 2$, $p = 0.4$, compared with the experimental value [1, 3] for $\text{Ga}_{1-x}\text{Mn}_x\text{As}$ at $x \sim 0.07$ and $T = 2\text{K}$ (squares).

As J/t decreases from 2, the maximum in T_C moves toward smaller x 's, and only $t > 0.5$ can provide high- T ferromagnetism. This illustrates the key role that the optimization of J/t plays in these models, effect not captured by MF approximations.

$|M|$ at $T \sim 0$ is in Fig. 2.6b. In agreement with experiments, the $x \sim 0.1$ result indicates a magnetization equal to approximately half of its maximum value. This non-saturated behavior originates in the random distribution of Mn-spins, since Mn-clusters are formed providing a trap to holes. Non-clustered spins are not much visited by those holes, and their spins are not polarized. With growing x , holes are more itinerant, polarizing the entire sample (Fig. 2.6b). Moreover, the nonsaturated low temperature state can be fully polarized with relatively small magnetic fields: in our studies, fields of just 10 T are sufficient to raise $|M|$ from 0.5 to nearly 1.0, at $x = 0.1$.

2.5 Summary

MC investigations of a spin-fermion model for DMSs indicate that the subtle regime of intermediate J/t appears to be the most relevant in these compounds. $T_C \sim 0.08t$ is an upper limit for the FM critical temperature, result close to those accepted for $x = 1$ [42]. The main results of this Chapter are summarized in Fig. 2.7, that contains the nontrivial J/t dependence of T_C and T^* , and T_C with varying x and p , at optimal J/t . To the extent that the present model is applicable to DMS materials, broad guidelines to improve T_C can be established: the optimal $J/t|_{opt} \sim 2$ must be intermediate between the itinerant and localized limits (Fig. 2.7a). This J/t , or larger, is expected to keep the semiconducting nature of the state at $T > T_C$. x should be increased beyond 0.1. At $J/t|_{opt}$, the best value is $x \sim 0.25$. The number of antisite defects must be controlled such that $p \sim 0.5$ ($p \sim 1$ would be detrimental because of competing antiferromagnetism). These predictions are in agreement with experimental developments since $\text{Ga}_{1-x}\text{Mn}_x\text{As}$ samples with T_C as high as 150 K were prepared[40], a result believed to be caused by an enhanced free-hole density. Also samples with $T_C \sim 127$ K and $x > 0.08$ were reported in Ref. [12], and, a T_C of 140K was achieved on high quality $\text{Ga}_{1-x}\text{Mn}_x\text{As}$ films grown with Arsenic dimers[68]. There is plenty of room to further increase the critical temperatures according to these theoretical calculations. As the coordination number grows, T_C grows. Finally, the simplest procedure to increase T_C relies on increasing the scale t . In fact, $\text{Ga}_{1-x}\text{Mn}_x\text{As}$ and $\text{In}_{1-x}\text{Mn}_x\text{As}$ have different hybridization strengths[69], and this should be an important consideration in studying new materials. This work also suggests formal analogies between DMSs and manganite models, with similar T_C s, and a related clustered state above ordering temperatures that will be discussed in more detail in Chapter 4.

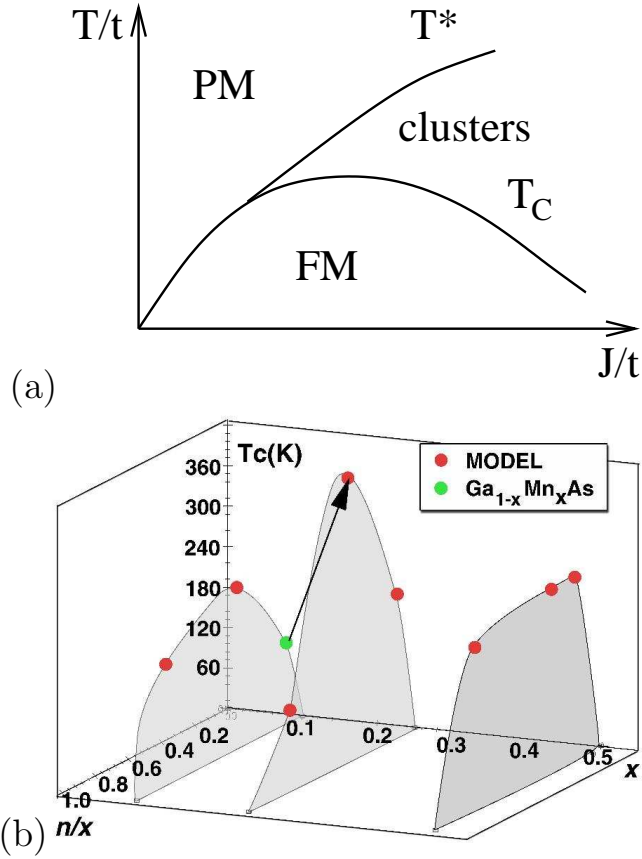


Figure 2.7. (a) Phase diagram of the single-band model Eq. (1.1), as discussed throughout this Chapter. The figure shows schematically the T_C and T^* dependence on the coupling J/t . The region between T^* and T_C contains FM “clusters”, with magnetic moments that are not aligned. (b) Numerically obtained T_C vs. x and p , at $J/t = 2.0$. Filled circles are from model Eq. (1.1) with $t = 0.5$ eV. The green point corresponds to the experimental value for $\text{Ga}_{1-x}\text{Mn}_x\text{As}$ at $x \sim 0.1$.

CHAPTER 3

IMPURITY BAND AND DYNAMICAL PROPERTIES

A more detailed study of the ferromagnetic state requires knowledge of the changes induced by magnetic impurities in the host semiconductor electronic structure at high doping levels. The band structure of III-V semiconductors was presented in §1.4.2. Optical absorption measurements on non-magnetic GaAs doped with Mn in the very dilute limit indicate that Mn forms a shallow acceptor level at 110 meV above the valence band [70]. However, the isolated impurity level picture is likely to break down at the high doping levels needed to initiate the ferromagnetic state in (Ga,Mn)As. Indeed, most band structure calculations predict a substantial hybridization of the GaAs bands with Mn d levels in this doping regime [45, 32, 71]. Direct measurements of the electronic states in (Ga,Mn)As from angle resolved photoemission spectroscopy (ARPES) show Mn-induced states both below the top of the valence band, and also very near the Fermi energy (E_F). The Mn-induced states at E_F are a critical component for carrier mediated ferromagnetism in the III-V series. In addition, infrared spectroscopy has allowed for the measurement of the absorption coefficient and optical conductivity of (Ga,Mn)As thin films that will enable a detailed examination of fine features near E_F .

The issue of identifying the band in which the itinerant carriers reside has led to discussion in the literature. According to one school of thought [72, 66, 73, 74, 24, 28] the holes are doped into the GaAs valence band. Within these models, the role of Mn doping is primarily restricted to increase the hole concentration. Another view

[45, 54, 25, 75, 20, 19, 76] assumes that as doping progresses from the very dilute limit, to the heavily doped regime, the shallow Mn acceptor level broadens and forms an impurity band.

The model presented in §1.4.1 could in principle assume either one of these scenarios depending on the strength of the coupling, although this study supports the view that the relevant regime of J/t is that of intermediate coupling, where the impurity band is formed and where carriers are only partially trapped near Mn spins. The formation of locally ordered regions (clusters) above T_C will also be discussed as it affects the dynamical properties. Finally, the transport properties of DMSs will be presented as obtained from the numerical study.

3.1 Density of States

In this section, the density-of-states (DOS) calculated at several couplings is shown and discussed. A few basic facts about the DOS of the model, Eq. (1.1), are presented first. If carrier localization effects are not taken into account and a ferromagnetic state is considered at strong J/t coupling, then two spin-split bands (“impurity bands”) will appear for this model, each with weight proportional to x , at each side of the unperturbed band which would have weight $2(1 - x)$ (Fig. 3.1). For partially compensated samples, $p < 1$, the chemical potential will be located somewhere in the first spin-split band, and, as a consequence, only this band would be relevant in the model Eq. (1.1).

In practice, Monte Carlo simulations show that, in the regime of interest where T_C is optimal, the impurity band is not completely separated from the unperturbed band. For this reason, both the unperturbed band and the impurity band have to be considered in quantitative calculations. To illustrate this, Fig. 3.2 shows $N(\omega)$ vs. ω for different J/ts in two dimensions. With growing J/t , the “impurity band” begins to form for $J/t \geq 3.0$, and at $J/t = 6.0$ it is separated from the main band, *i. e.*, there is a gap between the main band and the impurity band. However, note

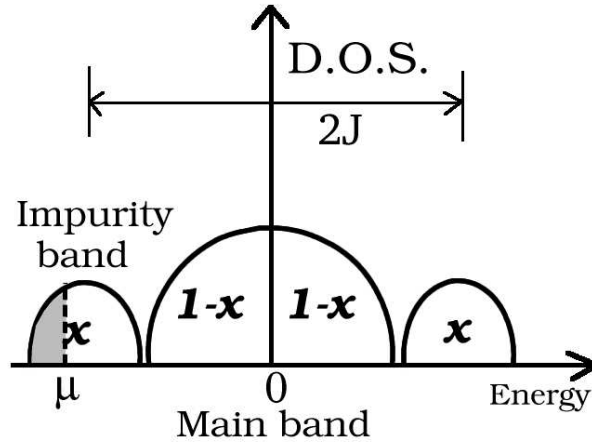


Figure 3.1. Schematic representation of the DOS, for a ferromagnetic configuration and strong enough J/t coupling. The “impurity band” has weight x , and the chemical potential μ lies within it.

that for this extreme regime of J/t , T_C is far lower than for $J/t = 3.0$, as discussed before in Section 2.3. In fact, the optimal J/t for the (x, p) parameters used here was found to be in the range 2.0-4.0. This implies that the model shows the highest T_C when the “impurity band” is about to form, but is not yet separated from the main band. This fact introduces an important difference between the approach to DMS materials followed in this work, and the theoretical calculations presented in Ref. [52, 19]. Fig. 3.3a-c indicates that a similar behavior is found in three dimensions. Once again, the optimal T_C occurs for intermediate J/t , as seen in Fig. 3.3d where the phase diagram obtained from a 6^3 lattice with $x = 0.25$ and $p = 0.3$ is shown. T_C and T^* were determined from the spin-spin correlations at short and large distances, as explained in §1.5.2.

The physical reason for the observed behavior is that at very large J/t , the states of the impurity band are highly localized where the Mn spins are. Local ferromagnetism can be easily formed, but global ferromagnetism is suppressed by the concomitant weak coupling between magnetized clusters.

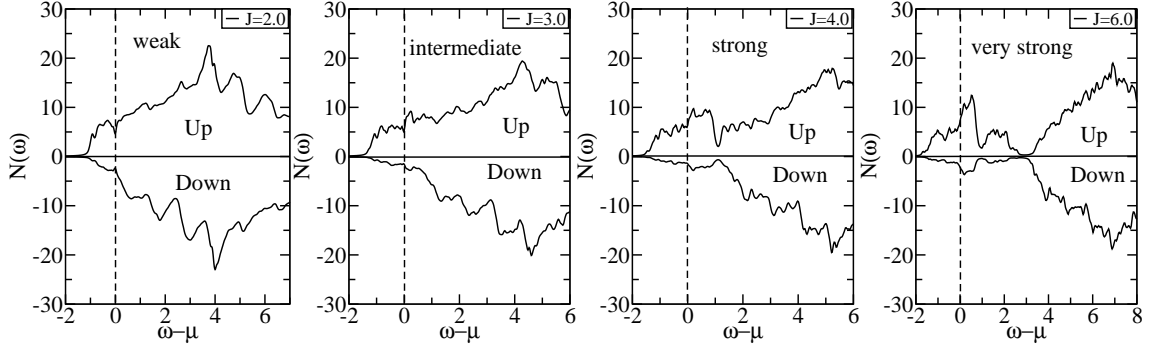


Figure 3.2. $N_{\uparrow}(\omega)$ and $N_{\downarrow}(\omega)$ vs. $\omega-\mu$ for a 10×10 periodic system with 26 spins ($x \sim 0.25$) and 10 electrons ($p \sim 0.4$) at $T/t = 0.01$. Results are shown for $J/t = 2.0$, $J/t = 3.0$, $J/t = 4.0$, and $J/t = 6.0$ as indicated. $\omega-\mu$ is in units of the hopping, t . The results are averages over eight configurations of disorder (but there is no qualitative difference in the results from different configurations).

Both, Figures 3.2 and 3.3 represent results obtained at particular values of parameters $x = 0.25$, $p = 0.3$, and $T/t = 0.01$. However, results for several other sets $\{(x, p, T)\}$ were gathered as well. The x dependence of the DOS is simple: increasing x produces a proportional increase in the number of states of the impurity band, and a corresponding decrease of the main band weight (see Fig. 3.1). In terms of p , increasing the effective carrier concentration by a small amount was found to simply shift the chemical potential to the right. Concerning the temperature dependence of the DOS, at low temperature the states contributing to the impurity band are polarized, *i. e.* the system is ferromagnetic, as shown by the different weights of the majority and minority bands (Figs. 3.2 and 3.3). As the temperature increases, spin disorder grows due to thermal fluctuations, and when $T \sim T^*$, *i. e.* in the paramagnetic regime, the bands become symmetric.

It appears that the only change that a small increase in the carrier concentration produces is an increase in the chemical potential. However, experimentally the appearance of a pseudo-gap at the Fermi energy has been reported[77]. Although the finite size effects in the present theoretical calculation do not allow for a detailed study of $N(\omega)$ at or very near the Fermi energy with high enough precision, in

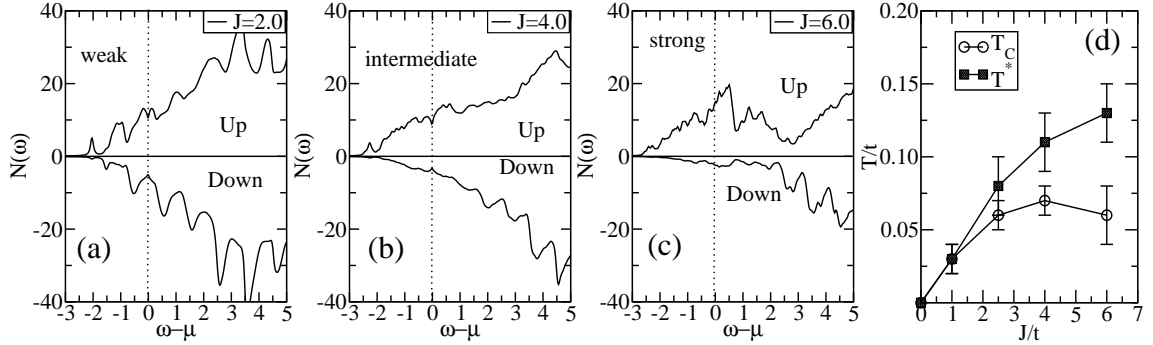


Figure 3.3. $N_{\uparrow}(\omega)$ and $N_{\downarrow}(\omega)$ vs. $\omega - \mu$ for a 6^3 periodic system with 54 spins ($x \sim 0.25$) and 16 electrons ($p \sim 0.4$) at $T/t = 0.01$. Results are shown for (a) $J/t = 2.0$, (b) $J/t = 4.0$, (c) $J/t = 6.0$. $\omega - \mu$ is in units of the hopping, t . The results are averages over eight configurations of disorder (but there is no qualitative difference in the results from different configurations). (d) T_C and T^* vs. J/t for a 6^3 lattice with $x = 0.25$ and $p = 0.4$.

certain cases a pseudo-gap was indeed observed in the present study at the chemical potential, particularly when the system is in the clustered regime. While this result certainly needs confirmation, it is tempting to draw analogies with the more detailed calculations carried out in the context of manganites, where the presence of a pseudo-gap both in theoretical models and in experiments is well established[78, 42, 59]. Pseudo-gaps are also present in under-doped high temperature superconductors. Given the analogies between DMS materials and transition-metal oxides unveiled in previous investigations[25], it would not be surprising that DMSs present a pseudo-gap in the clustered regime as well. More work is needed to confirm these speculations.

Results presented in this section for the DOS qualitatively agree with those found in Ref. [26] using the dynamical mean-field technique (DMFT) in the coupling regime studied there. However, the DMFT approach is a mean-field approximation local in space and, as a consequence, the state emphasized here –with randomly distributed clusters– cannot be studied accurately with such a technique.

Experimental evidence of the formation of the impurity band for $\text{Ga}_{1-x}\text{Mn}_x\text{As}$ has been provided by Okabayashi *et al.* in Refs. [79, 69]. Photoemission results for DMS

materials have also been presented in Ref. [80]. These experiments indicate that the Fermi energy is slightly above, but very near to, the valence-band maximum. Since in our results the Fermi energy is within the “impurity band”, this provides further evidence that the “impurity band” and the main band are not separated, but that they overlap in (Ga,Mn)As for the samples experimentally studied. It is interesting to remark that half the total width of the impurity band obtained in our simulations is about $2t$ (see, *e. g.*, Figs. 3.2 and 3.3), and using $t = 0.3$ eV[25] this is equal to 0.6 eV, in good agreement with the width 0.5 eV estimated from the photoemission experimental measurements mentioned before[79].

A study of the local DOS was also carried out. The purpose of the analysis was to further understand the inhomogeneous state that forms as a consequence of Mn-spin dilution and concomitant carrier localization. The local density of state $N_i(\omega)$ is defined by an equation similar to Eq. (1.12) but keeping the site dependence. The local DOS is shown in Fig. 3.4 on an 8×8 lattice at $x = 0.25$, $p = 0.4$, $J/t = 2.5$, and $T/t = 0.05$. In this particular case only, an arrangement of classical spins was introduced “by hand” such that the clusters are formed. In this way, sites can easily be classified in three groups, as discussed below. Despite using a particularly chosen spin configuration, the results for the DOS are similar to those obtained previously (Fig. 3.2) using a truly random distribution of spins. Lattice sites are classified as follows: the first group is defined to contain lattice sites that have a classical spin and belong to a spin cluster. The second class is composed of sites that have an isolated classical spin, *i. e.*, nearby sites do not have other classical spins. Finally, lattice sites without classical spins in the same site or its vicinity belong to the third class. $N_I(\omega)$, $N_{II}(\omega)$, and $N_{III}(\omega)$ denote the local DOS at sites corresponding to each of the three classes, respectively. In Fig. 3.4, “FM CLUSTER” indicates $N_I(\omega)$, while “ISOLATED SPIN” and “EMPTY SITE” are $N_{II}(\omega)$ and $N_{III}(\omega)$, respectively. It can be observed that $N_I(\omega)$ contributes to states inside the impurity band (there is a sharp peak near -1), but also contributes to the main band since the J/t used is

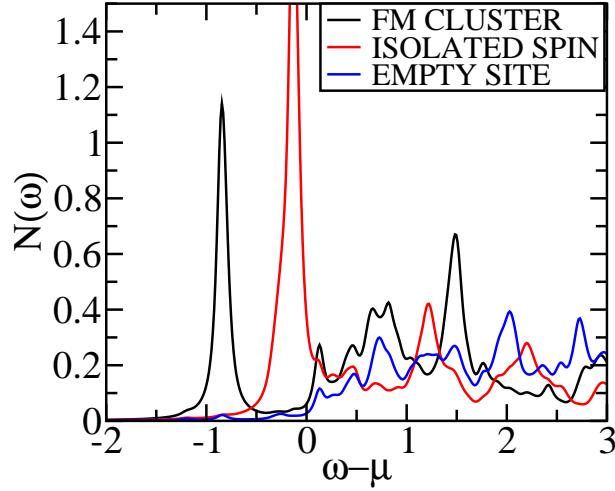


Figure 3.4. Local DOS for three different classes of sites on an 8×8 lattice with $J/t = 2.5$, $T/t = 0.01$, $x \sim 0.2$ and $p = 0.4$. This coupling regime corresponds to the intermediate optimal region, where the impurity band is not fully formed.

intermediate. $N_{\text{II}}(\omega)$ contributes a sharp peak near zero, and also has weight in the main band. This can be explained as follows: the electron is weakly localized at an isolated site yielding a state at $\omega_{\text{II}} \approx -J$ or, since $\mu \approx -J$ for $p \approx 0.4$, $\omega_{\text{II}} - \mu \approx 0$ (see Fig. 3.4). This interesting result shows that many of the states near zero in Figs. 3.2 and 3.3 may be *localized*, and they do not contribute to the conductivity. Finally, in $N_{\text{III}}(\omega)$ the empty sites contribute weight only in nearly unperturbed states, *i. e.*, states that belong to the main band. In conclusion, the local carrier density is very inhomogeneous and this fact has an important effect on the form of the site-integrated DOS. The results presented in this section show that scanning tunneling microscopy (STM) experiments would be able to reveal the clustered structure proposed here, if it indeed exists, when applied to DMS materials.

3.2 Optical Conductivity

In the previous section, it was argued that at the optimal coupling J/t – where T_C is maximized – the impurity band is not completely separated from the main band. This conclusion is supported by results obtained from the optical conductivity as well,

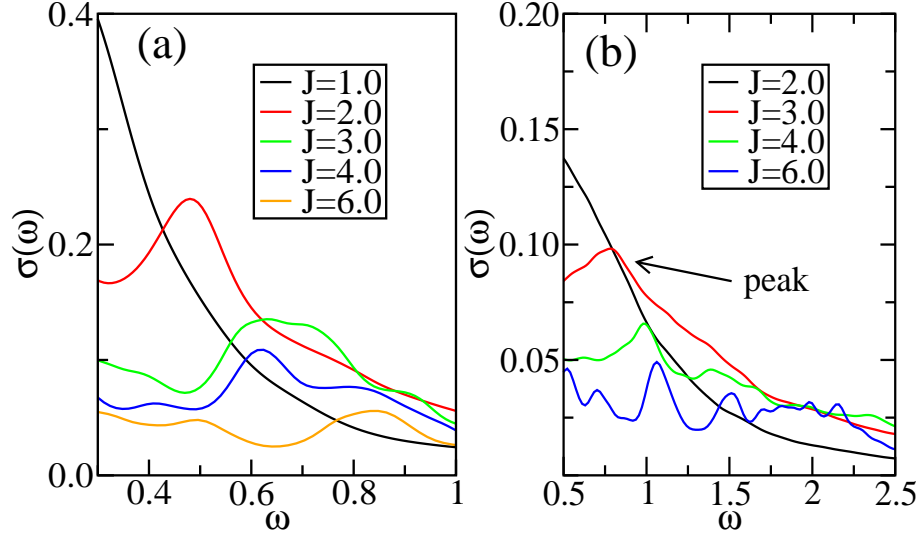


Figure 3.5. Coupling dependence of the conductivity at low temperature in two dimensions. (a) $\sigma(\omega)$ vs. ω for a 10×10 periodic system with 26 spins ($x \sim 0.25$), 10 electrons ($p \sim 0.4$), $T/t = 0.01$, and for different J/ts as shown. (b) $\sigma(\omega)$ vs. ω for a 6^3 periodic system with 54 spins ($x \sim 0.25$), 16 electrons ($p \sim 0.4$), $T/t = 0.01$, and for different J/ts as shown.

which is shown in Fig. 3.5a on a two-dimensional lattice. The optical conductivity has two main features: (i) a zero-frequency or Drude peak and (ii) a finite-frequency broad peak which is believed to correspond to transitions from the impurity band to the main band, as argued below. From Fig. 3.5a, it is observed that inter-band transitions are not much relevant at weak coupling ($J/t = 1.0$), but they appear with more weight at intermediate couplings ($J/t = 2.0 - 3.0$), where T_C is optimal. It is worth remarking that at J/t strong enough, *i. e.* $J/t = 6.0$, when the impurity band is well-formed, the finite-frequency peak is weaker in strength than for the optimal J/t due to localization. In fact, if J/t is so large that the “impurity band” is completely separated from the unperturbed band, then carrier localization would not allow for inter-band transitions. Similar results for the optical conductivity are found in three dimensions and are presented in Fig. 3.5b.

The rise in absorption that appears for $J/t \geq 2.5$ at intermediate frequencies is due to inter-band transitions, *i. e.* transitions from the impurity band to the

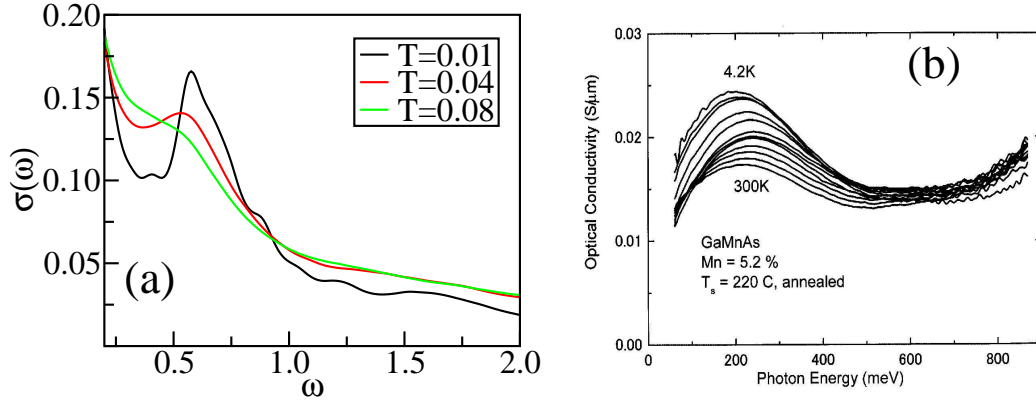


Figure 3.6. (a) Temperature dependence of the optical conductivity of model Eq. (1.1). Shown is $\sigma(\omega)$ vs. ω for a 10×10 periodic system with 26 spins ($x \sim 0.25$), $J/t = 2.5$, $p = 0.3$, and for different temperatures, as indicated. (b) Absorption coefficient $\alpha(\omega)$ spectra for a metallic sample prepared by low temperature annealing. The temperatures from down to top are 300, 250, 200, 150, 120, 100, 80, 60, 40, 20, 10 and 4.2 K. (from Katsumoto *et al.*[4])

unperturbed band. The frequency of this peak, ω_{inter} , depends upon J/t as well as carrier concentration p , but for $J/t \geq 2.5$ (which is an intermediate value) and $p = 0.4$ (a realistic value), it was observed that $0.5t \leq \omega_{inter} \leq 1.0t$. The model parameter t was previously estimated[25] to be $t \sim 0.3eV$, yielding $0.15eV \leq \omega_{inter} \leq 0.3eV$, in agreement with experiments (see below).

The temperature dependence of $\sigma(\omega)$ is shown in Fig. 3.6a. A broad peak at around 0.2 eV is experimentally observed in the optical conductivity of $Ga_{1-x}Mn_xAs$, as shown in Fig. 3.6b which is reproduced from Ref. [4]. This feature has been explained before in two different ways: (i) as produced by transitions from the impurity band to the GaAs valence band[26] or (ii) as caused by inter-valence band transitions[24, 74, 81]. Due to the frequency range and temperature behavior observed, our study supports the first possibility, *i. e.*, that the finite-frequency peak observed for $Ga_{1-x}Mn_xAs$ at around 0.2 eV is due to transitions from the impurity band to the main band. Experimental measurements[82] are also in agreement with this explanation for the 0.2 eV peak observed in the optical conductivity of (Ga,Mn)As samples.

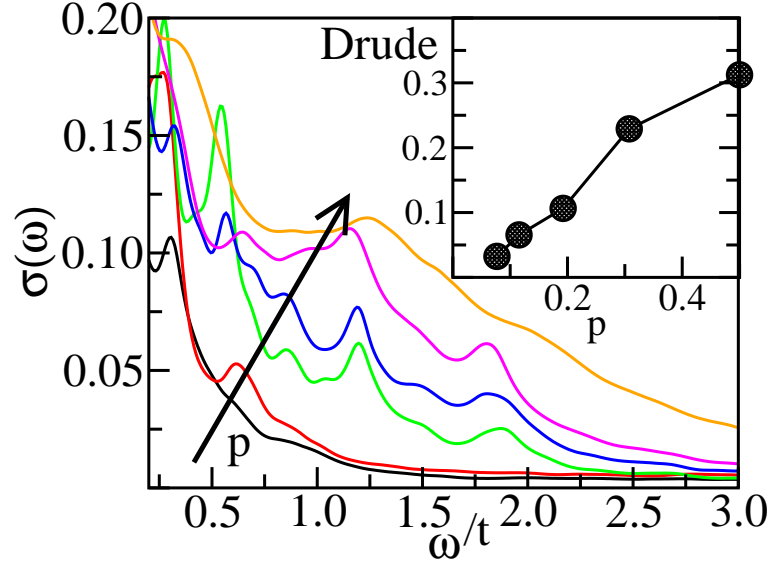


Figure 3.7. p -dependence of the optical conductivity. Shown is $\sigma(\omega)$, including the Drude weight, vs. ω for a 10×10 lattice, $x = 0.25$, $J/t = 2.5$, $T/t = 0.01$, and different values of p . In the direction of the arrow, p takes the values 0.08, 0.12, 0.20, 0.30, 0.38, and 0.5. *Inset:* Drude weight, D , vs. fraction of carriers, p .

The Drude weight increases in intensity with increasing carrier density, as can be seen from Fig. 3.7. In fact, the ratio p of carriers to Mn concentration, could explain, within the framework of this model, the different behavior observed at low frequencies for (Ga,Mn)As and (In,Mn)As. In the former case, no tail of the Drude peak is found. However, for InMnAs, a significant Drude tailing is observed[83, 4], with increasing intensity as the temperature increases. At large enough doping, our calculations based on model Eq. (1.1) predict a Drude-like peak for $\sigma(\omega)$ which could correspond to the regime valid for InMnAs, while for low doping this study predicts a very small Drude peak, which is the case for (Ga,Mn)As. Unfortunately, the precise carrier concentrations for both materials are not known experimentally with precision.



Figure 3.8. Geometry used for the calculation of the conductance. The interacting region (lattice) is connected by ideal contacts to semi-infinite ideal leads.

3.3 Conductance and Metal-Insulator Transition

3.3.1 Theory

In order to calculate the conductance of a system of interacting electrons, an electric potential must be applied to it and the linear response measured. To that effect, consider the system represented in Fig. 3.8, where the lattice, \mathcal{S} , has been connected by ideal contacts to two semi-infinite leads, at its left \mathcal{L}_L and right \mathcal{L}_R sides. The electric potential profile can be defined as:

$$H_1 = -eV \cos(\omega t) \hat{x}, \quad (3.1)$$

where the position operator along the horizontal direction is given by

$$\hat{x} = \sum_{i \in \mathcal{S} \cup \mathcal{L}_R} c_{i,\sigma}^\dagger c_{i,\sigma} \quad (3.2)$$

Then, the charge operator, $\hat{Q} = -e\hat{x}$ and the current through the system is given by the operator \hat{I} that obeys the following equation:

$$i\hbar \hat{I} = [\hat{H}, \hat{Q}] = -e [\hat{H}, \hat{x}] = -ei\hbar \hat{v}_x. \quad (3.3)$$

To obtain the total Hamiltonian of the system, \hat{H} , the electric potential term, Eq. (3.1), has to be added to Eq. (1.1). The velocity operator can be found by calculating the commutator in Eq. (3.3) and the result is

$$i\hbar \hat{v}_x = -t \sum_{i \in \mathcal{A}, j \in \mathcal{B}} (c_{i,\sigma}^\dagger c_{j,\sigma} - c_{j,\sigma}^\dagger c_{i,\sigma}), \quad (3.4)$$

where \mathcal{A} is the set of sites at the right end of the left lead, (*i. e.* those sites of the left lead in contact with the lattice), and \mathcal{B} is the set of sites at the left end of the lattice (*i.e.* those sites of lattice in contact with the left lead). The equation shows that the knowledge of the charge flux in the contact between the left lead and the sample is enough to evaluate the total current through the lattice. Obviously, the result is a consequence of the conservation of the flux along the whole system. Now the mean value of the current is given by

$$\langle \hat{I} \rangle = \sum_n f_n \langle n | \hat{I} | n \rangle \quad (3.5)$$

where $|n\rangle$ are the eigenvector of the one-electron sector (see Appendix A) and f_n are the occupation of the one-electron level n . It is straightforward to show that the conductance is given by:

$$G = \lim_{\omega \rightarrow 0} \frac{\langle \hat{I} \rangle}{V} = -e^2 \hbar \pi \lim_{\omega \rightarrow 0} \sum_{n,m} |\langle n | \hat{I} | m \rangle|^2 \frac{f_n - f_m}{E_n - E_m} \delta(E_m - E_n - \hbar\omega), \quad (3.6)$$

where the expression

$$i\hbar \langle n | \hat{v}_x | m \rangle = (E_n - E_m) \langle n | \hat{x} | m \rangle \quad (3.7)$$

has been used, which follows immediately from Eq. (3.3). Now, $|\langle n | \hat{I} | m \rangle|^2$ can be expressed in terms of the eigenvectors and eigenvalues in the one-electron sector that are obtained through the diagonalization procedure explained in §1.5.1 and thus be evaluated. However, direct use of Eq. (3.6) leads to numerical problems since eigenvalues are discrete and the conductance is obtained as a sum of delta functions. This fact forces the use of some procedure to extrapolate the limit $\omega \rightarrow 0$ that distorts the final static ($\omega = 0$) value.

To overcome these problems, J. Vergés[84] proposed to calculate the conductance, G , by using Green functions instead of eigenfunctions and use a Dyson equation to evaluate the former. Then, the Kubo formula at $T = 0$ is given by [85]

$$G = 2 \frac{e^2}{h} \text{Tr} \left[(i\hbar \hat{v}_x) \text{Im} \hat{\mathcal{G}}(E) (i\hbar \hat{v}_x) \text{Im} \hat{\mathcal{G}}(E) \right], \quad (3.8)$$

where \hat{v}_x is the velocity operator in the x direction and $\text{Im}\hat{\mathcal{G}}(E)$ is obtained from the advanced and retarded Green functions using $2i\text{Im}\hat{\mathcal{G}}(E) = \hat{\mathcal{G}}^R(E) - \hat{\mathcal{G}}^A(E)$, where E is the Fermi energy. Eq. (3.8) needs the Green function matrix elements at sets \mathcal{A} and \mathcal{B} only due to the simple form of \hat{v}_x , Eq. (3.4), and the presence of the trace. To that effect, the selfenergy, Σ_i , of the ideal right lead is obtained, then iterated through the sample layer by layer, and finally, connected to the selfenergy coming from the left ideal lead. The equation defining the iteration is obtained from Dyson equation for the Green function [86] and has the following form:

$$\Sigma_{i-1} = V_{i-1,i}(EI - V_{i,i} - \Sigma_i)^{-1}V_{i,i-1}. \quad (3.9)$$

Using this equation, Σ_{i-1} is calculated once the former selfenergy matrix and the intralayer $V_{i,i}$ and interlayer $V_{i-1,i}$ matrices are known. After iterating the right side from $+\infty$ to 1 and the left side from $-\infty$ to 0, the Green function elements needed to calculate G are given by

$$[EI - H - \Sigma_l(E) - \Sigma_r(E)]\mathcal{G}(E) = I, \quad (3.10)$$

where H is the matrix representing the layer 0 or \mathcal{A} plus layer 1 or \mathcal{B} system Hamiltonian. $\Sigma_l(E)$ represents the left selfenergy matrix and similarly for the one on the right.

The method was first used in Ref. [87] for a spin-fermion model in the context of manganites. The numerical results that will be presented below make use of this method. The entire equilibrated lattice as obtained from the MC simulation is introduced in the geometry of Fig. 3.8. In some cases a variant of the method was used (this modification was suggested by J. Vergés). Instead of connecting the lattice to an ideal lead with equal hoppings, a replica of the lattice was considered at the sides. This modification, although slightly slower, takes into account all of the Monte Carlo data. In addition, averages over the random Mn spin distributions are carried out. The physical units of the conductance G in the numerical simulations are e^2/h as can be inferred from Eq. (3.8).

3.3.2 Numerical Results

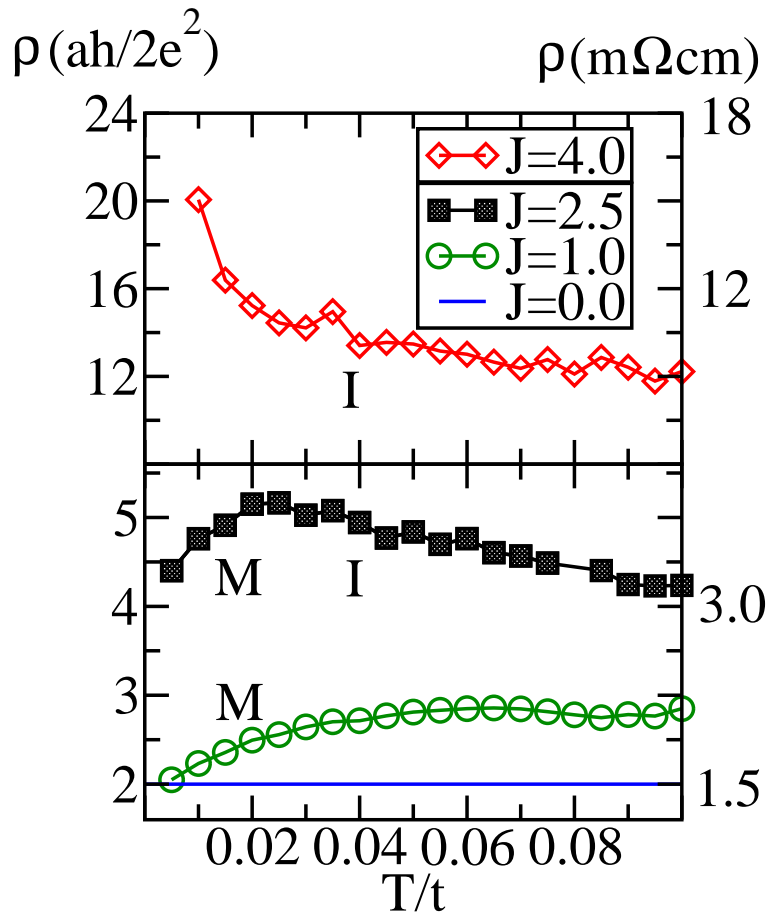


Figure 3.9. Dependence of the theoretically calculated resistivity, ρ , with temperature in three dimensions. Shown is $\rho = L/G$ vs. T on 4^3 lattices, 16 spins ($x = 0.25$), and 5 carriers ($p = 0.3$) for the J/ts indicated. An average over 20 disorder configurations has been performed in each case. Units are shown in two scales, $ah/(2e^2)$ on the left and $m\Omega cm$ on the right, with $L = 4$ and assuming $a = 5.6 \text{ \AA}$.

In Fig. 3.9 the inverse of the conductance, which is equal to the resistivity in two dimensions, is plotted for a three-dimensional lattice at weak, intermediate, and strong coupling, at fixed $x = 0.25$ and $p = 0.3$. For the weak coupling regime ($J/t = 1.0$) the system is weakly metallic at all temperatures. In the other limit, at strong coupling, $1/G$ decreases with increasing temperature, indicating a

robust insulating phase, as a result of the system being in a clustered state at the temperatures explored[25, 54], with carriers localized near the Mn spins. At the important intermediate couplings emphasized in this work, the system behaves like a dirty metal for $T < T_C$, while for $T_C < T < T^*$, $1/G$ slightly decreases with increasing temperature, indicating that a soft metal to insulator transition takes place near T_C . For $T > T^*$, where the system is paramagnetic, $1/G$ is almost constant. As mentioned before, for strong enough J/t , $T_C \rightarrow 0$ and therefore no metallic phase is present.

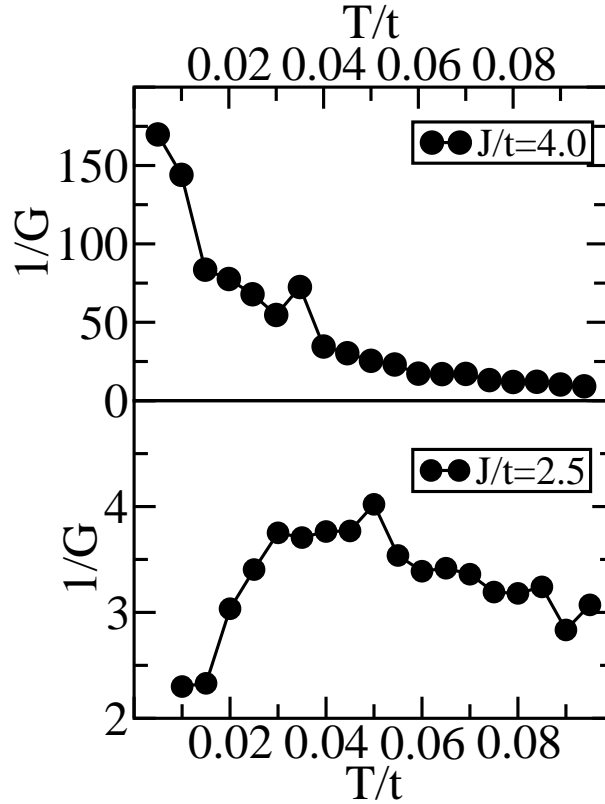


Figure 3.10. Inverse of the conductance, $1/G$, vs. T calculated on a 10×10 lattice with 26 spins ($x \sim 0.25$), 8 electrons ($p \approx 0.3$), and two values of J/t as indicated. Shown is an average over three disorder configurations. $1/G$ has units of $h/(2e^2)$ in two dimensions.

Similar qualitative behavior is found for the two-dimensional case (Figs. 3.10 and 3.11). Furthermore, in Fig. 3.11 the spin-spin correlations have been plotted to show the location of T_C and T^* and their relation to the resistivity. The approximate

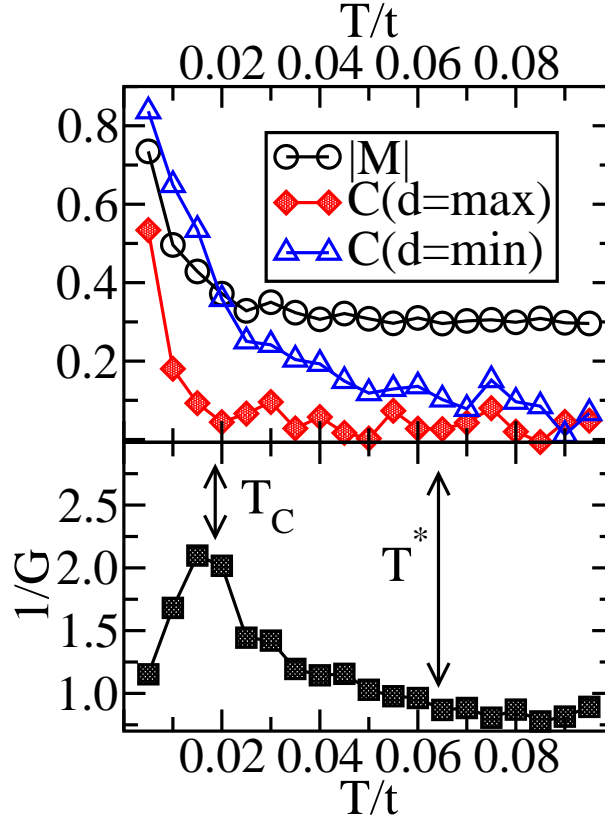


Figure 3.11. Magnetization, $|M|$, spin-spin correlations, $C(d)$, at maximum and minimum distance, and inverse of the conductance, $1/G$, vs. T on a 12×12 lattice with 22 spins ($x \approx 0.15$), 6 electrons ($p \approx 0.3$), and $J/t=1.0$.

vanishing of spin correlations at different temperatures, depending on the distance d studied, allowed us to obtain an approximate determination of T_C and T^* , as mentioned in §1.5.2.

It is interesting to compare the numerical results with experiments. For $\text{Ga}_{1-x}\text{Mn}_x\text{As}$, data similar to those found in our investigations have been reported [4, 38]. A typical measurement for resistivity versus temperature, T , can be found in Fig. 3.12 [2]. The qualitative behavior of the resistivity in these samples agrees well with the theoretical results presented in Fig. 3.9 if intermediate couplings are considered. On the other hand, stronger or weaker couplings are not useful to reproduce the data, since the result is either insulating or metallic at all temperatures,

respectively. By metallic and insulator regimes what is meant is the slope of the resistivity vs. temperature curves; the resistivity of DMSs samples is usually much higher than that of good metals.

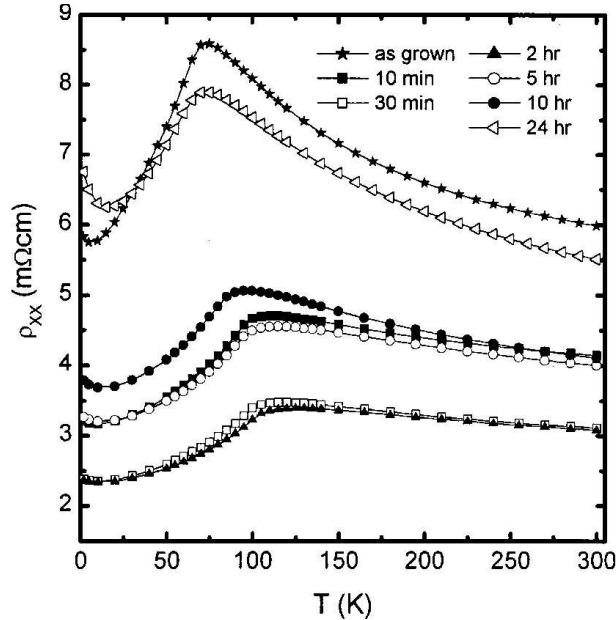


Figure 3.12. Resistivity of a sample of (Ga,Mn)As with $x = 0.083$ as a function of the temperature. There is a clear peak in the resistivity near the ferromagnetic temperature T_C which is approximately 100K. Samples with different annealing times are shown. (From Ref. [2])

Furthermore, the experimental numerical values of the resistivity are in agreement with the results presented here, even though model Eq. (1.1) does not include a realistic treatment of the GaAs host bands (§1.4.2). This can be shown as follows. The conductivity of a three-dimensional sample is related to the conductance by $\sigma = G/L$, where L is the side length of the lattice. Hence the resistivity is $\rho = L/G$. The units of G are, as explained before, $h/(2e^2)$, and in our case $L = 4a$, where a is the lattice spacing. Assuming $a = 5.6 \text{ \AA}$, then the values shown in Fig. 3.9 are obtained.

It is important to remark that in Fig. 3.9 the minimum resistivity for $J/t = 2.5$ is 3.3 mΩcm, whereas the minimum possible value for that carrier concentration and

lattice size used is $1.5 \text{ m}\Omega\text{cm}$, which corresponds to the case $J/t = 0$. As already mentioned, in spite of the label “metallic” for these results, the absolute values of the resistivity are high. Similarly, in the metallic phase of the sample shown in the experimental results of Ref. [2], the minimum resistivity is only $3 - 6 \text{ m}\Omega\text{cm}$ approximately. Both in theory and experiments, the metallic phase appears to be “dirty”, which is likely due to the reduced number of carriers, and the localizing effect of the disorder.

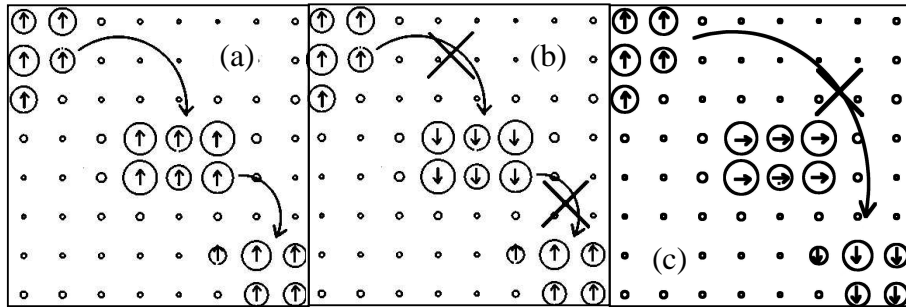


Figure 3.13. Qualitative explanation of the transport properties of clustered states. Shown are three clusters created ‘by hand’ on an 8×8 lattice and with spin configurations also selected ‘by hand’ to illustrate our ideas. For a (a) FM state at $J/t = 2.5$ and $p = 0.4$, conduction is possible due to the alignment of magnetic moments and the conductance was found to be $G = 2.8(2e^2/h)$. For the “clustered” state regime, two typical configurations (b) and (c) are shown where the conduction channels are broken and as a consequence $G \approx 0$. For the same clustered state but with randomly selected spin orientations (not shown) the conductance is small but finite $G \approx 0.5(2e^2/h)$. The radius of the solid circles represent the local charge density.

For J/t intermediate or strong, localization of the wave function is observed at intermediate temperatures (Section 2.3). This implies that carriers tunnel between impurity sites without visiting the main band, leading to insulating behavior. Below T_C conduction is favored by the ferromagnetic order and, as a consequence, as temperature decreases conductance increases. To further understand why the conductance (resistance) has a minimum (maximum) around T_C it is helpful to consider the three states: FM, clustered, and paramagnetic (PM) as depicted for a special spin configuration in Fig. 3.13 on an 8×8 lattice. This configuration is not

truly random but it was chosen “by hand” for simplicity so that the spin clusters can easily be recognized. In the case of a random configuration of spins a similar reasoning can be drawn. For the FM state of Fig. 3.13, conduction is possible and indeed the measured conductance is $G \approx 2.8(2e^2/h)$. For the two possible clustered states represented in Figs. 3.13b and c, the conduction is reduced due to the different alignment of spins in different clusters. This is verified by calculating the conductance which is $G \approx 0.0$ in those cases. For a paramagnetic spin arrangement with spin pointing in random directions (not shown), the conductance is small but finite, $G \approx 0.5(2e^2/h)$. It follows that the clustered state has the minimum conductance, and this explains the observed behavior of the resistivity with a maximum near T_C , *i. e.* , when the system is clustered.

It is also interesting to remark that the optimal value of J/t changes with x (*e. g.* for small x , J/t optimal is also small). Since $J/t|_{\text{opt}}$ (see Section 2.3 for notation) approximately separates the metal from the insulator, working at a fixed J/t (as in real materials) and varying x , then an insulator at high temperatures is found at small x , turning into a metal at larger x . Although results of previous investigations with as grown samples had found an insulator-metal-insulator transition with increasing x [38], a more careful annealing procedure yields results [2] that are in excellent agreement with the numerical simulations reported here. The issue discussed in this paragraph is visually illustrated in Fig. 3.14, for the benefit of the reader.

3.4 Magnetoresistance

The magnetoresistance (MR) percentage ratio was calculated using the definition $MR = 100 \times (\rho(0) - \rho(B))/\rho(B)$. Fig. 3.15 shows the magnetization, $|M|$, and the resistivity as a function of the applied field B on a 12×12 lattice, $x = 0.15$, $p = 0.4$, $J/t = 1.0$, and low temperature. In two dimensions at $x = 0.25$ and $p = 0.3$, the intermediate coupling corresponds to $J/t = 2.5$, but at $x = 0.15$, now $J/t = 1.0$

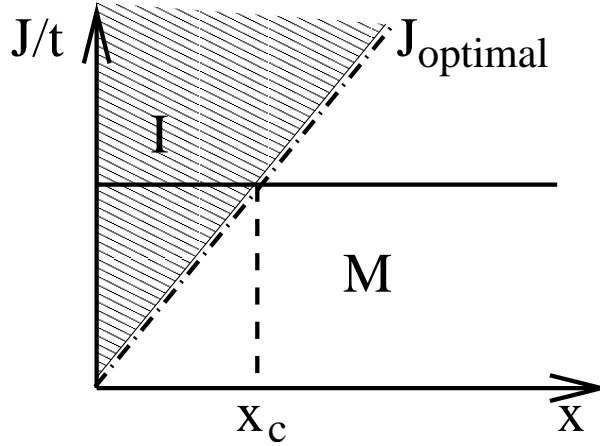


Figure 3.14. Dependence of J/t_{optimal} with x , approximately separating the metal from the insulator (standard notation). At fixed J/t (horizontal solid line), as in experiments, the system should transform from an insulator to a metal with increasing x , in agreement with experiments[2].

corresponds to optimal coupling since as x decreases the optimal J/t also decreases. For these parameters, T_C was estimated to be $0.02t$ and $T^* \approx 0.06t$. The value in Tesla of the magnetic field was calculated assuming $g = 2.0$ and $S = 5/2$ for the localized spins. The units of the resistivity are $h/(2e^2)$ for the two-dimensional lattice. The approximate values of the magnetoresistance are 18% at 4 Tesla, and 30% at 12 Tesla.

In the simulations it was observed that $|M|$ increases with increasing magnetic field. At zero magnetic field $|M|$ is 60% of its maximum value, while at 12 T it has reached 80% approximately. This is in agreement with the experimental results in Fig. 3 of Ref. [38] where the magnetization is 50% of its maximum value at zero field, but it reaches 70% of that maximum value at 4 T. In this numerical study it was also observed that $1/G$ decreases with increasing magnetic field, showing at all fields a negative magnetoresistance. Near T_C the resistivity decreases by 20%-30% increasing the field from zero to 12 T, while the decrease in resistivity at higher temperatures is much smaller. The present computational results agree very well with the experimentally measured dependence of the resistivity and magnetization

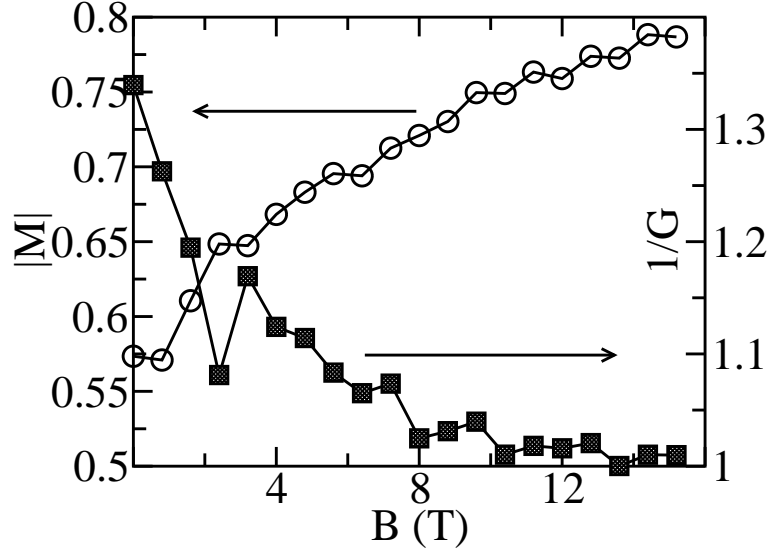


Figure 3.15. Magnetization, $|M|$, and inverse conductance, $1/G$, vs. magnetic field, B , on a 12×12 lattice with PBC, $x = 0.15$, $p = 0.3$, $J = 1.0$, and $T/t = 0.01$ (same parameters as in Fig. 3.11). The units of B are Tesla, assuming $g = 2.0$ and $S = 5/2$. The units of $1/G$ are $h/2e^2$.

on magnetic fields. For example, in Fig. 2(b) of Ref. [38], the decrease in resistivity is 25% near $T_C \approx 60$ K when increasing the field from zero to 15 T. A much smaller decrease in resistivity is observed at higher temperatures ($T > 120$ K). It is also indicated in that experimental reference that the magnetoresistance is between 30% and 40% at 12 Tesla.

It is interesting to remark that substantial magnetoresistance effects have been reported in thin films consisting of nanoscale $Mn_{11}Ge_8$ ferromagnetic clusters embedded in a dilute ferromagnetic semiconductor matrix[88]. The characteristics of these materials are analogous to our clustered state, that also show a robust MR effect due to magnetization rotation of spontaneously formed clusters.

CHAPTER 4

IMPORTANCE OF CLUSTERED STATES

4.1 Introduction

In this Chapter the key role of inhomogeneities will be discussed in more detail. The ideas about the “clustered phase” in Mn-doped magnetic semiconductors explained before (Section 2.5) will be expanded to a variety of other compounds. In the context of manganites inhomogeneities are key to explain the colossal magnetoresistance effect[42]. Moreover, evidence has accumulated that underdoped high temperature superconductors are also inhomogeneous at the nanoscale[89], and theoretical approximations that assume homogeneous states are questionable. It is still unclear if the inhomogeneities have stripe features, as discussed extensively in previous years[90], or whether they correspond to more randomly shaped clusters, as assumed in the manganite context. Also the origin of these inhomogeneities is much debated. Computational simulations will play a key role in determining the properties of models for manganites and cuprates, since percolative clustered physics is difficult to handle with other methods.

After revisiting the relevance of cluster formation in DMSs, a detailed work on the formation of clusters in disordered high temperature superconductors [7] will be presented. For completeness, the well known topic of inhomogeneities in the context of manganites will be shortly addressed. These quite unexpected similarities between apparently very different materials promise to lead to a global unified view, where clustered states become a new paradigm of condensed matter physics[7].

4.2 Clustered States in DMS Revisited

It was shown in Chapters 2 and 3 that a clustered state is formed above T_C for intermediate and large J/t couplings. This state is a candidate to describe DMS materials since it explains both the resistivity maximum around T_C (Section 3.3), as well as the decrease in resistivity with increasing applied magnetic field (Section 3.4). In addition, it provides an optimal T_C . It is only formed for intermediate or larger J/t and when the compensation is strong, $p < 0.4$. Since for large J/t the carriers are localized, the problem becomes one of percolation theory, which has already been treated using different approaches and approximations[76]. In this section only a very simple way of visualizing this state will be presented. First, consider a two-dimensional lattice with 5% Mn spins represented as black dots, as shown in Fig. 4.1a. The carrier wave function, $\psi(r)$, is considered to be localized around a Mn spin and it is assumed to be a step function for simplicity, *i. e.* $\psi(r)$ is non-zero only if $r < r_l$ where r_l is the localization radius introduced by hand. Sites where the wave function is not zero are the black areas of Fig. 4.1b. In this case, sites can be classified into connected regions, and that feature is indicated in Fig. 4.1c using different colors or shades. Each region is correlated and will correspond to a FM cluster. All spins belong to some large cluster. As the concentration x grows, the clusters will tend to merge. Conversely, as x decreases, these clusters will become more and more isolated.

Experimental work on (Ga,Cr)As have revealed unusual magnetic properties which were associated with the random magnetism of the alloy. The authors of Ref. [91] explained their results using a distributed magnetic polaron model, that resembles the clustered-state ideas discussed here and in Refs. [25, 53, 76].

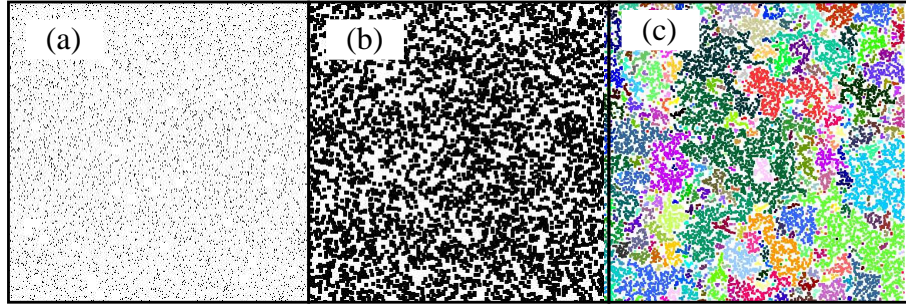


Figure 4.1. Percolation picture for the formation of the clustered-state regime. (a) Two-dimensional lattice representing randomly-located classical spins as black dots with $x=0.05$. (b) Black areas represent non-zero carrier wave function, assuming a step-function profile for the wave functions with radius equal to 2 sites, as explained in the text. (c) Same as (b) but now showing connected regions (which could in practice correspond to the FM clusters discussed in the text) indicated with different colors.

4.3 High- T_c Superconductors

4.3.1 Introduction

High temperature superconductivity was discovered in 1986, by J. G. Bednorz and K. A. Müller in a ceramic copper oxide material at a temperature of about 30K. The result came as a surprise to the physics community since these compounds are poor conductors. However, the confirmation of these experiments by Takagi *et al.* in 1987 brought about a race for the preparation of materials with even higher critical temperatures. Since then compounds with T_c s as high as 130 K have been discovered. New technologies may emerge from this field, for example SQUID magnetometers (mentioned in Section 1.3) and Josephson integrated circuits.

However, despite this enormous technological interest, it is important to remark that this is a very important area of basic research. Basic research in high T_c brings together expertise from materials scientists, physicists and chemists, experimentalists and theorists because of the complexity of the materials[92]. In fact, much of the research in high T_c superconductivity has spilled over to other areas such as magnetism in the manganites, complex oxides, etc.

An overview of the lattice structure and phase diagram of the most widely studied high- T_c compounds can be found in Ref. [5]. A superconductor is said to belong to the family of high- T_c superconductors (HTS) if it has CuO_2 planes. In general, the high- T_c materials are basically tetragonal, and all of them have one or more CuO_2 planes in their structure, which are separated by layers of other atoms (Ba, O, La, \dots). The structure of $\text{La}_{2-x}\text{Sr}_x\text{CuO}_4$ is depicted in Fig. 4.2a. This compound was among the first high-temperature superconductors discovered. In $\text{La}_{2-x}\text{Sr}_x\text{CuO}_4$, the CuO_2 planes are approximately 6.6 \AA apart, separated by two LaO planes. These form the charge reservoir that captures electrons from the conducting planes upon doping, when La^{3+} are randomly replaced by Sr^{2+} and thus fewer electrons are donated to the CuO_2 planes. The electrons come from oxygen ions, changing their configuration from O^{2-} to O^- , and thus creating one *hole* in the p -shell. The phase diagram of this material is shown in Fig. 4.2b and apart from the details it is representative of most high T_c compounds. Near half-filling, antiferromagnetic

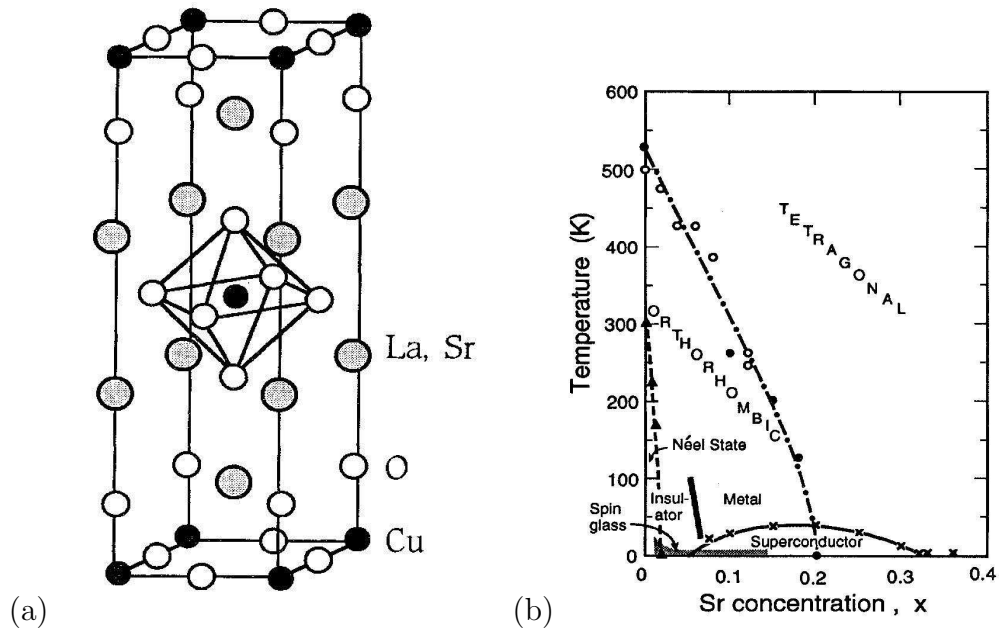


Figure 4.2. (a) Crystal structure and (b) phase diagram of $\text{La}_{2-x}\text{Sr}_x\text{CuO}_4$. (From Ref. [5])

order is observed. For Sr dopings between $0.05 \leq x \leq 0.30$ approximately, a superconducting phase is found at low enough temperatures. The maximum value of T_c is observed at the optimal doping of $x \sim 0.15$. Between the superconducting and antiferromagnetic regions a so called *pseudogap* phase is observed, where a “pseudogap” is present in the DOS.

4.3.2 Clustered States

The formation of clustered states in High-Tc superconductors could explain the important challenges in the physics of these materials, as will be shown. In this context an antiferromagnetic (AF) insulator competes with a *d*-wave superconductor (SC). There is overwhelming experimental evidence for several unconventional regimes in HTS, including the already mentioned pseudogap region at temperatures above the superconducting phase, and a largely unexplored glassy state separating the AF from the SC phase at low hole-doping x . In addition, investigations unveiled another remarkable property of HTSs that defies conventional wisdom: the existence of *giant proximity effects* (GPE) in some cuprates[93], where a supercurrent in Josephson junctions was found to run through non-SC Cu-oxide-based barriers as thick as 10^3 and 10^4Å . This contradicts the expected exponential suppression of supercurrents with barrier thickness beyond the short coherence length $\xi \sim 10 - 20 \text{Å}$ of Cu-oxides. Another challenge is to understand the increase of the SC critical temperature, T_c , with the number of adjacent Cu-oxide layers N_ℓ . The purpose of the original work presented here is to propose a scenario that resolves both effects (*i. e.*, GPE and the increase of T_c with N_ℓ) simultaneously. The main idea relies on the presence of a nanoscale inhomogeneous state for HTS, which leads to the *prediction of colossal effects in cuprates*. Indeed, neutron scattering studies have revealed “stripes” of charge in Nd-LSCO [90], while scanning tunneling microscopy (STM) experiments indicate “patches” of charge in Bi2212 [89], both of which are

consistent with the key assumption in our analysis that inhomogeneous or clustered states are prevalent in HTS.

Studies of the t-J model have revealed SC and striped states[94] evolving from the undoped limit. Then, it is reasonable to assume that AF, SC, and striped states are dominant in cuprates, and their competition regulates the HTS phenomenology. However, further computational progress using basic models is limited by lattice sizes that cannot handle the nanoscale structure unveiled by STM experiments. Considering these restrictions, here a *phenomenological* approach will be pursued to understand how these phases compete, incorporating the quenched disorder inevitably introduced by chemical doping. This effort unveils novel effects of experimental relevance, not captured with first-principles studies.

4.3.3 Method of Study

The analysis starts with a phenomenological model of itinerant electrons (simulating carriers) on a square lattice, locally coupled to classical order parameters:

$$\begin{aligned}
H_F = & -t \sum_{\langle \mathbf{i}\mathbf{j}\rangle, \sigma} (c_{\mathbf{i}\sigma}^\dagger c_{\mathbf{j}\sigma} + H.c.) + 2 \sum_{\mathbf{i}} J_{\mathbf{i}} S_{\mathbf{i}}^z s_{\mathbf{i}}^z - \sum_{\mathbf{i}\sigma} \mu_{\mathbf{i}} n_{\mathbf{i}\sigma} \\
& + \frac{1}{D} \sum_{\mathbf{i}, \alpha} \frac{1}{V_{\mathbf{i}}} |\Delta_{\mathbf{i}\alpha}|^2 + \sum_{\mathbf{i}, \alpha} (\Delta_{\mathbf{i}\alpha} c_{\mathbf{i}\uparrow} c_{\mathbf{i}+\alpha\downarrow} + H.c.), \tag{4.1}
\end{aligned}$$

where $c_{\mathbf{i}\sigma}$ are fermionic operators, $s_{\mathbf{i}}^z = (n_{\mathbf{i}\uparrow} - n_{\mathbf{i}\downarrow})/2$, $n_{\mathbf{i}\sigma}$ is the number operator, D is the lattice dimension, and $\Delta_{\mathbf{i}\alpha} = |\Delta_{\mathbf{i}\alpha}| e^{i\phi_{\mathbf{i}}^\alpha}$ are complex numbers for the SC order parameter defined at the links $(\mathbf{i}, \mathbf{i} + \alpha)$ (α is the unit vector along the x or y directions). The spin variables are assumed to be Ising spins for computational simplicity (denoted by $S_{\mathbf{i}}^z$).

To diagonalize Eq. (4.1) a modified Bogoliubov transformation is applied

$$\begin{aligned}
c_{\mathbf{i}\uparrow} &= a_{\lambda}^{\uparrow}(i) \gamma_{\lambda\uparrow} - a_{\lambda+N}^{\downarrow*} \gamma_{\lambda\downarrow}^{\dagger} \\
c_{\mathbf{i}\downarrow} &= a_{\lambda}^{\downarrow}(i) \gamma_{\lambda\downarrow} - a_{\lambda+N}^{\uparrow*} \gamma_{\lambda\uparrow}^{\dagger} \tag{4.2}
\end{aligned}$$

An implicit sum over the index λ that satisfies $1 \leq \lambda \leq N$ is assumed. Now, operators associated to each term in the Hamiltonian can be defined in a natural way. Thus, K_i will denote the kinetic energy operator, μ_i , the Coulomb potential operator, J_i the J-term operator, and Δ_i the Δ -term operator. Then, the diagonalization of the $2N \times 2N$ matrix:

$$H^\uparrow = \begin{pmatrix} K_i + J_i - \mu_i & \Delta_i \\ \Delta_i^* & -K_i + J_i + \mu_i \end{pmatrix}, \quad (4.3)$$

provides the eigenvectors $a_\lambda^\uparrow(i)$. In a similar way the eigenvectors $a_\lambda^\downarrow(i)$ can be calculated by diagonalizing:

$$H^\downarrow = \begin{pmatrix} K_i - J_i - \mu_i & \Delta_i \\ \Delta_i^* & -K_i - J_i + \mu_i \end{pmatrix}. \quad (4.4)$$

Let E_λ^\uparrow be the N largest eigenvalues of H^\uparrow and Y_λ^\uparrow be the N lowest eigenvalues of H^\uparrow , where $1 \leq \lambda \leq N$. In the same way, let E_λ^\downarrow and Y_λ^\downarrow be the N largest and N lowest eigenvalues of H^\downarrow respectively, where $1 \leq \lambda \leq N$.

Let m_λ^- be the eigenvalues of $M_i^- \equiv K_i - J_i$. Then, after applying transformation Eq. (4.2), Eq. (4.1) becomes:

$$H_F = \sum_\lambda (E_\lambda^\uparrow f(\beta E_\lambda^\uparrow) + E_\lambda^\downarrow f(\beta E_\lambda^\downarrow)) + \sum_\lambda m_\lambda^- - \sum_\lambda E_\lambda^\downarrow, \quad (4.5)$$

where $f(x) = 1/(1 + e^x)$. It uses eigenvalues of both matrices and all sums run from $\lambda = 1$ to $\lambda = N$. This expression is the basis for the evolution of the system using a Monte Carlo procedure similar to the one described for DMS in Section 1.4. Note also that half of the eigenvalues of each matrix have been discarded, otherwise we would have duplicated the number of degrees of freedom of the problem that has to be always $2N$. That the largest eigenvalues are the ones that have to be taken into account can be demonstrated by considering the energy at $T = 0$. Indeed if a smaller eigenvalue is added, a Bogoliubov particle can occupy that level and thus it would be possible to construct a state with lower energy than the ground state, which is absurd.

Observables that are expressed in terms of electron operators, $c_{i\sigma}$, can be calculated by first transforming them into Bogoliubov operators, $\gamma_{\lambda\sigma}$, by means of Eq. (4.2). For instance, the number of electrons is given by the expression:

$$N_e = \sum_{\lambda,i,\sigma} |a_{\lambda+N}^\sigma(i)|^2 + \sum_{\lambda,i,\sigma} (|a_\lambda^\sigma(i)|^2 - |a_{\lambda+N}^\sigma(i)|^2) f(\beta E_\lambda) \quad (4.6)$$

Thus, the number of electrons at $T = 0$ is *not* given by simply filling levels of the one-particle sector, because in this context those particles are Bogoliubov particles not electrons. Paradoxically neither is the number of Bogoliubovs at $T = 0$ obtained by filling levels up to the chemical potential and in fact that number is always zero at $T = 0$ and $J_i = 0$. That follows from the symmetry around zero of the combined eigenvalues of the matrices given by Eq. (4.3) and (4.4). In fact, the eigenvalues of one matrix are the opposites of the other for *any* parameters and configuration as can be easily proved. The chemical potential is of no use for adjusting the number of Bogoliubovs because adding a Bogoliubov does not change the number of electrons since both operators $c_{i\sigma}$ and $c_{i\sigma}^\dagger$ enter in the definition of γ_λ , a result that can be obtained by inverting Eqs. (4.2).

All this shows that special care has to be taken to diagonalize Eq. (4.1) due to the presence of the pairing term that does not conserve the number of particles.

Finally, for future use the formula for the calculation of the density of states is given below:

$$N(\omega) = \sum_{\lambda,i,\sigma} |a_\lambda^\sigma(i)|^2 \delta(\omega - E_\lambda) + |a_{\lambda+N}^\sigma(i)|^2 \delta(\omega + E_\lambda) \quad (4.7)$$

4.3.4 Exact Ground States

Although in general numerical studies have to be used (see §4.3.5 and ff.) to extract information from Eq. (4.1), in certain special cases the ground state can be determined exactly. For example, if $V_i = 0$, $\mu_i = 0$ and $J_i = J$ for all sites therefore

$\Delta_i = 0$ and it can be proved that the ground state is a pure antiferromagnet, with dispersion:

$$E_k = \pm \sqrt{J^2 + e_k^2}, \quad (4.8)$$

where e_k is given by Eq. (A.1). The values of k are restricted to half the Brillouin zone and they are double because of the spin (see also Appendix A). Conversely, if $J_i = 0$ but $V_i = V$ then the ground state is a perfect d -wave superconductor. If $\Delta_{i,\alpha} = |\Delta|e^{i\phi_\alpha}$ then the total energy is given by:

$$E = \sum_k e_k - \sum_k \sqrt{e_k^2 + |2\Delta|^2 |f_k|^2}, \quad (4.9)$$

where

$$f_k = \sum_\alpha e^{i\phi_\alpha} \cos(k_\alpha). \quad (4.10)$$

When $\phi_{\hat{x}} = \phi_{\hat{y}}$ an extended s -wave dispersion is obtained and, on the other hand, $|\phi_{\hat{x}} - \phi_{\hat{y}}| = \pi$ yields a d -wave dispersion instead. Each of these will have a different energy and it can be proved that the d -wave dispersion gives a lower energy compared to the other, and, therefore, it is the true ground state. This is a consequence of the pairing term in the Hamiltonian that involves nearest neighbor sites.

4.3.5 Non-Universal Phase Diagram

The parameters of relevance are J_i , μ_i , and V_i (t is the energy unit), that carry a site dependence to allow the inclusion of quenched disorder. For a fixed configuration, $\{\Delta_{i\alpha}\}$ and $\{S_i^z\}$, the one-particle sector is diagonalized using a modified Bogoliubov transformation [95, 96] as explained in §4.3.3. Then, a standard Monte Carlo (MC) simulation similar to the one used for DMSs (§1.5.1) is carried out. One of the goals is to estimate T_c , as well as T_c^* , defined as the temperature at which strong short-distance SC correlations develop.

Without quenched disorder, V_i , J_i and μ_i in Eq. (4.1) are site independent. The MC analysis reveals that in the clean limit the low temperature (T) phase diagram

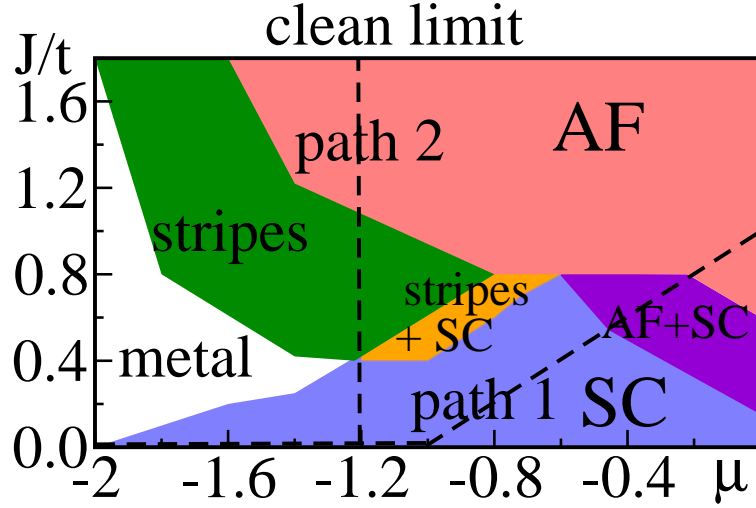


Figure 4.3. MC phase diagram for Eq. (4.1) without disorder at low temperatures, along $V = 1 - J/2$. Six regions are observed: AF, d -SC, stripes, coexisting SC+AF, coexisting stripes+SC, and metal.

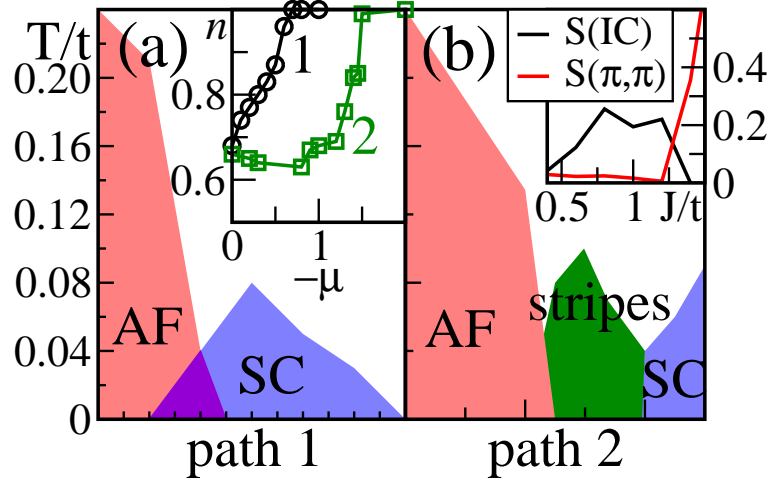


Figure 4.4. (a) MC phase diagram including temperature along “Path 1” (when J reaches 0, the path continues along the horizontal axis). *Inset:* n vs. μ along Paths 1 and 2. Transitions along Path 1 appear continuous, whereas along Path 2 there are indications of first-order transition. (b) MC phase diagram along “Path 2”. Lattice sizes in all cases are 8×8 and 12×12 . *Inset:* Spin structure factor $S(\mathbf{q})$ at (π, π) and for incommensurate (IC) momenta.

(Fig. 4.3) has a robust AF phase for electronic densities $n \sim 1$ and a d -wave SC phase for $n < 1$, not surprising since these states are favored explicitly in Eq. (4.1). The d -wave correlation function, defined as

$$C^{\alpha\beta}(\mathbf{m}) = \sum_{\mathbf{i}} \left\langle |\Delta_{\mathbf{i}}| |\Delta_{\mathbf{i}+\mathbf{m}}| \cos(\phi_{\mathbf{i}}^{\alpha} - \phi_{\mathbf{i}+\mathbf{m}}^{\beta}) \right\rangle, \quad (4.11)$$

was used to estimate T_c as the temperature at which d -wave correlations are 5% of their maximum value, at the largest distances for the lattices considered here. Other criteria lead to identical qualitative trends, slightly shifting the phase diagrams. T^* is deduced similarly, but using the shortest-distance correlation function ($|\mathbf{m}|=1$). The Néel temperature, T_N , associated with the classical spins was defined by the near vanishing ($\leq 5\%$) of long-distance spin order using

$$C_S(\mathbf{m}) = \sum_{\mathbf{i}} \langle S_{\mathbf{i}}^z S_{\mathbf{i}+\mathbf{m}}^z \rangle, \quad (4.12)$$

while T_N^* relates to short-range spin order.

However, the phase diagram presents other interesting regions. Along “Path 1” in Fig. 4.3, the AF-SC transition occurs through a region of *local* coexistence, with tetracritical behavior (Fig. 4.4a). Our approach without disorder has similarities with SO(5) ideas [97] where the AF/SC competition was extensively discussed to explain the high- T_c phase diagram. In addition, a phase diagram where the couplings were kept constant was introduced in Ref. [98]. Along “Path 2” the AF-SC interpolating regime has alternating doped and undoped *stripes*, and a complex phase diagram with temperature (Fig. 4.4b). The stripe region was determined by incommensurabilities in $S(\vec{q})$, *i. e.*, when the maximum of $S(\vec{q})^1$ is shifted from (π, π) by an amount usually equal to $2\pi/L$ in either direction, L being the linear length of the lattice. Moreover, at low temperatures, static spin and charge stripes are seen for this region in the Monte Carlo snapshots. These stripes evolve continuously from the $V = 0$ limit studied in Ref. [99]. At $V \neq 0$, the doped regions of the stripes have nonzero SC

¹ $S(\vec{q})$, the structure factor, is given by the Fourier transform of Eq. (4.12).

amplitude at the mean-field level. Then, in our model *there is no unique AF \rightarrow SC path*. In fact, $\text{La}_{2-x}\text{Sr}_x\text{CuO}_4$ (LSCO) and others may have stripes [90, 100], while $\text{Ca}_{2-x}\text{Na}_x\text{CuO}_2\text{Cl}_2$ has a more complex inhomogeneous pattern. Both, however, become SC with increasing x . This suggests that *the phase regimes in the underdoped region of the cuprates may not be universal*.

4.3.6 Local Order and Pseudo-gap Formation

The results obtained from the model become even more interesting upon introducing disorder. For this case, (J_i, V_i, μ_i) are chosen to be plaquette impurities surrounded by a metallic “halo” and embedded in a background that favors antiferromagnetism. Disorder may have several forms, but here Sr-doping in single-layers is simulated. Sr^{2+} replaces La^{3+} , above the center of a Cu-plaquette in the Cu-oxide square lattice. Then, as hole carriers are added, a hole-attractive plaquette-centered potential should also be incorporated. Near the center of this potential, n should be sufficiently reduced from unity that, phenomenologically, tendencies toward SC should be expected. To interpolate between the SC central plaquette and the AF background, a plaquette “halo” with no dominant tendency was introduced. More precisely, the SC core is composed by four sites and has $(J, V, \mu) = (0.1, 1.0, -1.0)$, the metallic “halo” is composed by the eight surrounding sites and has $(J, V, \mu) = (0.1, 0.1, -0.5)$ and the background has $(J, V, \mu) = (1.0, 0.1, 0.0)$ as sketched in Fig. 4.5a. However, the overall conclusions found here are simple, and independent of the disorder details.

The phase diagram obtained using MC simulations is shown in Fig. 4.5b. The similarity with the widely accepted phase diagram of cuprates is clear. The disorder has opened a hole-density “window” where none of the two competing orders dominates. Inspecting “by eye” the dominant MC configurations (snapshots) at low- T in this intermediate regime reveals a patchy system with islands of SC or AF, and random orientations of the local order parameters, leading to an overall disordered

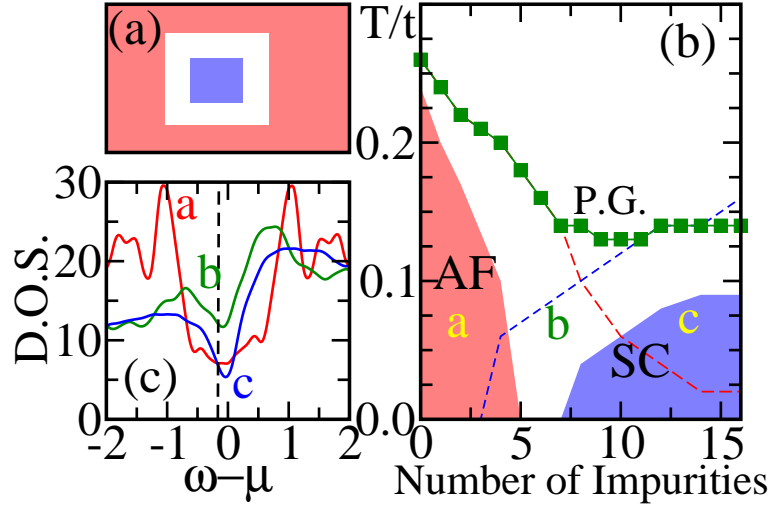


Figure 4.5. (a) Plaquette impurity schematic representation. Parameters are chosen such that the blue (black) region favors superconductivity, $(J, V, \mu) = (0.1, 1.0, -1.0)$, with a surrounding white region where $(J, V, \mu) = (0.1, 0.1, -0.5)$ with no order prevailing. The impurity is embedded in a background (red, dark gray) that favors the AF state, $(J, V, \mu) = (1.0, 0.1, 0.0)$. (b) MC phase diagram for model Eq. (4.1) including quenched disorder (lattices studies are 8×8 and 12×12). Shown are T_c and T_N vs. number of impurities (equal to number of holes). The SC and AF regions with short-range order (dashed lines), and T^* as obtained from the PG (dot-dashed line) are also indicated. (c) DOS at points a , b , and c of (a), with a PG.

“clustered” state. This result is compatible with photoemission experiments for $x = 0.03$ LSCO, that reveal spectral weight in the node direction of the d -wave superconductor even in the insulating glassy regime[101].

A new temperature scale $T_{p.g.}$ is defined when a *pseudogap* (PG) develops in the fermionic density-of-states (DOS) (Fig. 4.5b). The AF and d -SC regions both have a gap (smeared by T and disorder, but nevertheless with recognizable features). But even the “disorder” regime (case b in Fig. 4.5c) has a PG. MC snapshots help explain this behavior: in the disordered state there are small SC or AF regions, as mentioned before. Locally each has a smeared-gap DOS, either AF or SC. Not surprisingly, the mixture presents a PG. The behavior of $T_{p.g.}$ vs. x is remarkably similar to that found experimentally. *The cuprates’ PG may arise from an overall-disordered clustered state with local AF or SC tendencies*, without the need to invoke exotic states. This

PG is associated to robust short-range correlation functions and is represented by the red and blue dashed lines of Fig. 4.5b.

4.3.7 Multilayers and Colossal Effects

The results reported thus far, based on Eq. (4.1), already revealed interesting information. However, the inhomogeneous nature of the clustered region suggests that percolative phenomena may be at work, and for such studies larger clusters are needed. To handle this issue, a new model containing only classical degrees of freedom is proposed, with low-powers interactions typical of Landau-Ginzburg (LG) approaches:

$$\begin{aligned}
H &= r_1 \sum_{\mathbf{i}} |\Delta_{\mathbf{i}}|^2 + \frac{u_1}{2} \sum_{\mathbf{i}} |\Delta_{\mathbf{i}}|^4 + \sum_{\mathbf{i}, \alpha} \rho_2(\mathbf{i}, \alpha) \mathbf{S}_{\mathbf{i}} \cdot \mathbf{S}_{\mathbf{i}+\alpha} \\
&- \sum_{\mathbf{i}, \alpha} \rho_1(\mathbf{i}, \alpha) |\Delta_{\mathbf{i}}| |\Delta_{\mathbf{i}+\alpha}| \cos(\Psi_{\mathbf{i}} - \Psi_{\mathbf{i}+\alpha}) + r_2 \sum_{\mathbf{i}} |\mathbf{S}_{\mathbf{i}}|^2 \\
&+ \frac{u_2}{2} \sum_{\mathbf{i}} |\mathbf{S}_{\mathbf{i}}|^4 + u_{12} \sum_{\mathbf{i}} |\Delta_{\mathbf{i}}|^2 |\mathbf{S}_{\mathbf{i}}|^2.
\end{aligned} \tag{4.13}$$

The fields $\Delta_{\mathbf{i}} = |\Delta_{\mathbf{i}}| e^{i\Psi_{\mathbf{i}}}$ are complex numbers representing the SC order parameter. The classical spin at site \mathbf{i} is $\mathbf{S}_{\mathbf{i}} = |\mathbf{S}_{\mathbf{i}}| (\sin(\theta_{\mathbf{i}}) \cos(\phi_{\mathbf{i}}), \sin(\theta_{\mathbf{i}}) \sin(\phi_{\mathbf{i}}), \cos(\theta_{\mathbf{i}}))$. $\rho_1(\mathbf{i}, \alpha) = 1 - \rho_2(\mathbf{i}, \alpha)$ is used as the analog of $V = 1 - J/2$ of the previous model, allowing an AF-SC interpolation changing just one parameter. α denotes the two directions \hat{x} and \hat{y} in two dimensions, and also \hat{z} for multilayers. $\rho_2(\mathbf{i}, \alpha)$ was chosen to be isotropic, *i. e.*, α -independent.

The spin and superconducting correlations are defined as before:

$$C_{spin}(\vec{x}) = \frac{1}{N} \sum_{\vec{y}} \langle \vec{S}_{\vec{y}} \cdot \vec{S}_{\vec{y}+\vec{x}} \rangle, \tag{4.14}$$

$$C_{sc}(\vec{x}) = \frac{1}{N} \sum_{\vec{y}} \Delta_{\vec{y}} \Delta_{\vec{y}+\vec{x}} \cos(\Psi_{\vec{y}} - \Psi_{\vec{y}+\vec{x}}) \tag{4.15}$$

The vanishing of these functions at maximum distance determine T_c and T_N . In practice T_c (or T_N) was estimated as the temperature at which the SC (or AF) correlation is less than 5% of its maximum value.

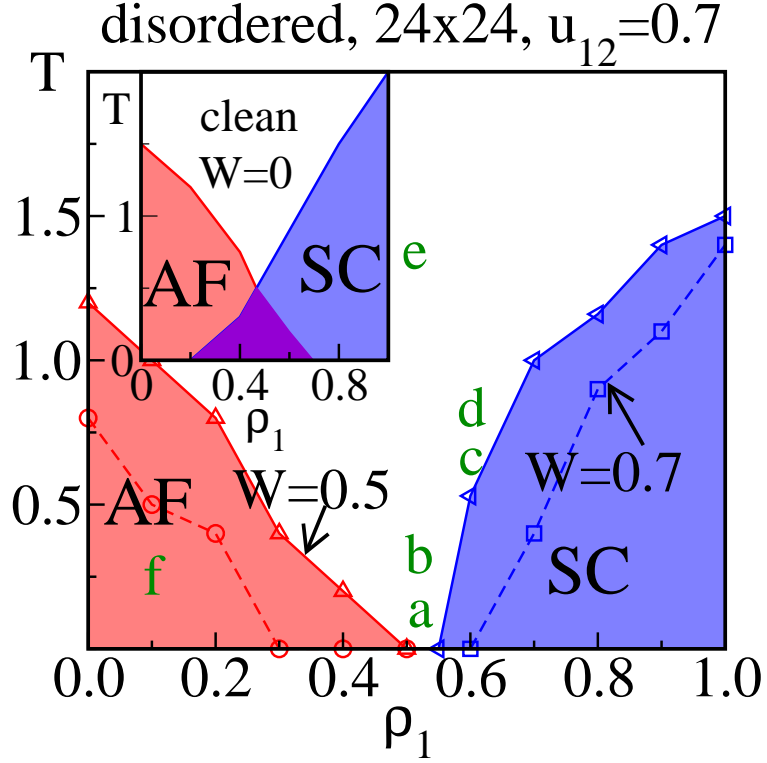


Figure 4.6. MC phase diagram (Eq. (4.13)) at $u_{12} = 0.7$. Parameters are $r_1 = -1$, $r_2 = -0.85$, and $u_1 = u_2 = 1$ and disorder strength $W = 0.5$, but the conclusions are not dependent on coupling fine-tuning. *Inset:* results without disorder ($W = 0$) showing tetracriticality (magenta indicates SC+AF coexistence).

The Hamiltonian is invariant with respect to a global rotation for spins and to a global phase change for $\Delta_{\mathbf{i}}$. The ground state when $\Delta_{\mathbf{i}}$ is constant and $\rho_2 = 0$ is such that Ψ_i is constant if $\rho_1 > 0$ (extended s -wave). If $\rho_1 < 0$ and the lattice is bipartite then $\Psi_{\mathbf{i}}$ is constant in each sublattice and the corresponding difference is equal to π (d -wave). When $\rho_1 = 0$ the ground state is AF ($\rho_2 > 0$) or FM ($\rho_2 < 0$). In this study $\rho_2 > 0$ always.

Disorder is introduced by adding a randomly selected bimodal contribution, *i. e.* $\rho_2(\mathbf{i}, \alpha) = \rho_2^0 \pm W$, where W is the disorder strength ($W = 0$ is the clean limit).

MC results for model Eq. (4.13) with and without disorder are in Fig. 4.6, for “weak” coupling, $u_{12} = 0.7$, which leads to tetracritical behavior in the clean case. The corresponding phase diagram for “strong” coupling, $u_{12} = 2.0$, is shown in

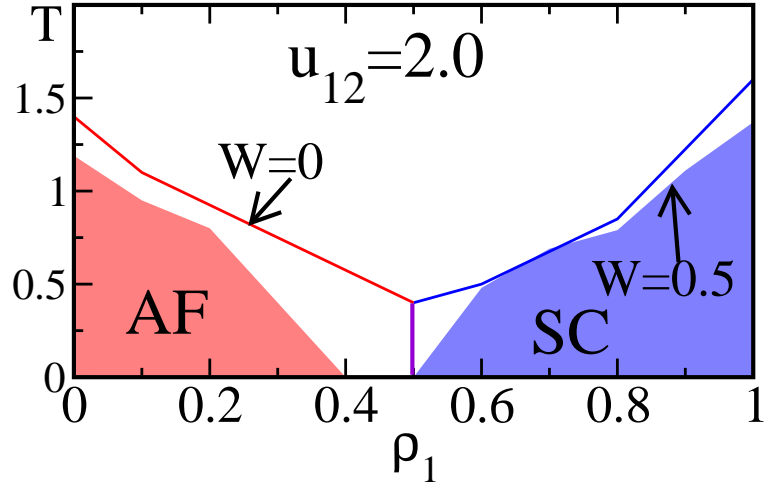


Figure 4.7. Phase diagram for the Guinzburg-Landau model for $u_{12} = 2$. The clean case ($W = 0$) is bicritical but the addition of disorder ($W = 0.5$) opens a clustered region between the superconductor and the antiferromagnet.

Fig. 4.7 and it is bicritical without disorder. Both at $W = 0$ and $W \neq 0$, the qualitative similarity with the fermionic model results, Figs. 4.3 and 4.5b, is clear. Clustered states (not shown) appear in MC snapshots. Then, both models share a similar phenomenology, and Eq. (4.13) can be studied on larger lattices. However, model Eq. (4.13) cannot lead to doped-undoped stripes, unlike the more general case Eq. (4.1).

The main result of this section can now be described. It will be argued below that the models studied can present “colossal” effects. Consider a typical clustered state (Fig. 4.8b) found by MC simulations in the disordered region. This state has preformed local SC correlations – nanoscale regions having robust SC amplitudes within each region, but no SC phase coherence between different regions – rendering the state globally non-SC (the correlation at the largest distances available, C_{SC}^{\max} , is nearly vanishing). Now an artificial SC “external field”, which can be imagined as caused by the proximity of a layer with robust SC order (*e. g.*, comprised of a higher- T_c material) will be considered. In practice, this is achieved in the calculations by extending Eq. (4.15) to three dimensions in a natural way. When two layers are

considered and one of them is kept fixed, the calculation is rigorously equivalent to introduce a term $|\Delta_{\text{SC}}^{\text{ext}}| \sum_{\mathbf{i}} \rho_1(\mathbf{i}, \hat{z}) |\Delta_{\mathbf{i}}| \cos(\Psi_{\mathbf{i}})$, where $\Delta_{\text{SC}}^{\text{ext}}$ acts as an external field for SC. The dependence of $C_{\text{SC}}^{\text{max}}$ with $\Delta_{\text{SC}}^{\text{ext}}$ is remarkable (Fig. 4.8a). While at points e and f , located far from the SC region in Fig. 4.6, the dependence is the expected one for a featureless state, the behavior closer to the superconducting region and particularly at small temperatures is highly nonlinear and unexpected. For example, at point a , $C_{\text{SC}}^{\text{max}}$ vs. $\Delta_{\text{SC}}^{\text{ext}}$ has a slope (at $\Delta_{\text{SC}}^{\text{ext}} = 0.02$) which is approximately 250 times larger than at e or approximately 13 times larger than at $W = 0$ (same T , ρ_2 , and u_{12}). The reason for this anomalous behavior is the clustered nature of the states. This is shown in Fig. 4.8c, to be contrasted with Fig. 4.8b, where a relatively small field – in the natural units of the model – nevertheless leads to a quick alignment of superconducting phases, producing a globally superconducting state.

Nanoscale clusters stabilized by quenched disorder also lead to a novel proposal for explaining the increase of T_c with the number of Cu-oxide layers, N_ℓ . In this effort, the MC phase diagrams of single- and bi-layer systems described by Eq. (4.13), with and without disorder, were calculated using exactly the same parameters (besides a coupling $\rho_2(\mathbf{i}, \hat{z})$, equal to those along \hat{x} and \hat{y} , to connect the layers). It is observed that *the single layer has a lower T_c than the bilayer*. This can be understood in part from the critical fluctuations that are stronger in *two dimensions* than in *three dimensions*. But even more important, cluster percolation at $W \neq 0$ is more difficult in two dimensions than three dimensions, for example, two-dimensional disconnected clusters may become linked through an interpolating cluster in the adjacent layer. Then, in the phenomenological approach presented here it is natural that T_c increases with N_ℓ , as can be seen from the phase diagram in Fig. 4.9. This concept is even *quantitative* – up to a scale – considering the remarkably similar shape of T_c vs. N_ℓ found both in the MC simulation and in experiments (see Fig. 4.10). The MC results also suggest that the substantial variations of T_c known to occur in single-layer cuprates can be attributed to the particular sensitivity of two-dimensional systems

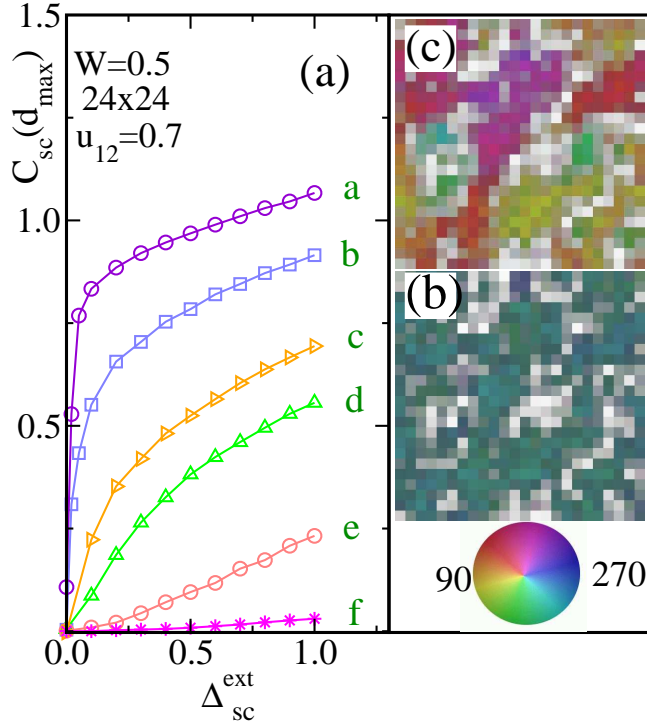


Figure 4.8. (a) C_{SC}^{\max} vs. Δ_{SC}^{ext} (see text) on a 24×24 lattice, with $u_{12} = 0.7$ and $W = 0.5$, at the five points *a-f* indicated in Fig. 4.6. A “colossal” effect is observed in *a*, *b*, *c*, and *d* where the $\Delta_{SC}^{\text{ext}}=0$ state is “clustered”. A much milder (linear) effect occurs far from the SC phase (*e* and *f*). MC snapshots are shown at $\Delta_{SC}^{\text{ext}} = 0.0$ (*b*) and $\Delta_{SC}^{\text{ext}} = 0.2$ (*c*), both at $T = 0.1$ and $\rho_2 = 0.5$, using the same quenched-disorder configuration. The color convention is explained in the circle (colors indicate the SC phase, while intensities are proportional to $Re(\Delta_i)$). The AF order parameter is not shown. The multiple-color nature of the upper snapshot, reflects a SC phase randomly distributed (*i. e.* an overall non-SC state). However, a small external field rapidly aligns those phases, leading to a coherent state in (*c*).

to disorder. As the number of layers is increased, *i. e.*, the system becomes more three-dimensional, the influence of disorder *decreases*, both in experiments [102] and in the numerical simulations presented here.

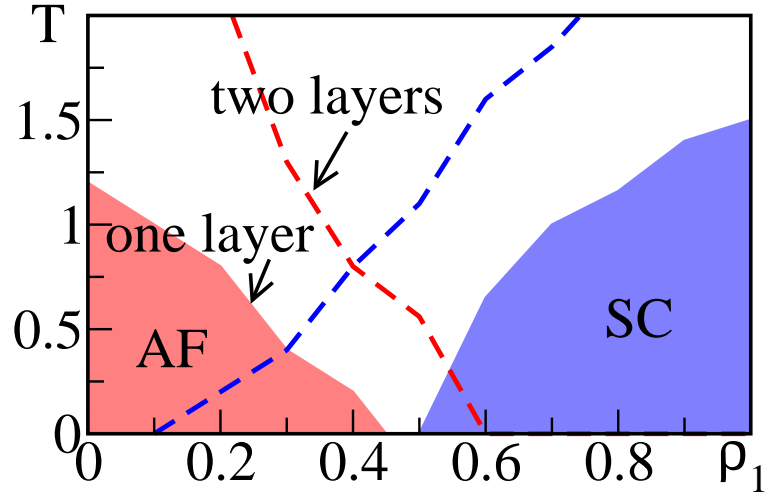


Figure 4.9. Comparison between the phase diagrams of the single layer system and the two layer system for $u_{12} = 0.7$ and $W = 0.5$ on a 24×24 lattice.

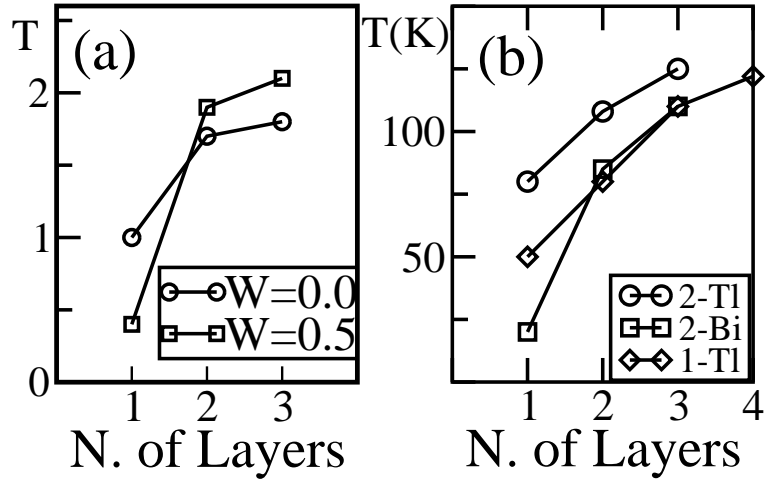


Figure 4.10. (a) T_c vs. N_ℓ for $u_{12} = 0.7$, $\rho_2 = 0.3$, $W = 0.7$, and $24 \times 24 \times N_\ell$ clusters. Shown are results with and without disorder. (b) Experimental T_c (in K) for three HTS families, 2-Tl, 2-Bi, and 1-Tl, as indicated. (From Ref. [6]).

4.4 Manganites

The study of manganese oxides, known as manganites, that exhibit the “colossal” magnetoresistance effect is one of the main areas of research in the area of correlated electron systems. Considerable progress has been achieved in understanding many properties of these compounds. These studies suggest that the ground states of manganite models tend to be intrinsically inhomogeneous due to the presence of strong tendencies toward phase separation, typically involving ferromagnetic metallic and antiferromagnetic charge and orbital ordered insulating domains [42].

The first-order transitions that separate the metallic and insulating phases in the clean limit (*i. e.* without disorder) play a key role to explain the colossal magnetoresistance effect [59, 103, 42, 104] mentioned above. The first-order character of the transition is caused by the different magnetic and charge orders of the competing states. The phase diagram without disorder is illustrated in the left panel of Fig. 4.11. When quenched disorder is introduced in the coupling or density that is modified to change from one phase to the other, the point where the Néel and Curie temperatures meet decreases in value and eventually collapses to zero as in the central panel of Fig. 4.11. For large values of the disorder strength, a spin glassy disordered region appears at low temperatures involving coexisting clusters (Fig. 4.11, right panel). The size of the coexisting islands is regulated by the disorder strength and by the proximity to the original first-order transition. Simulations by Burgy *et al.* [58] have shown that the clustered state between the Curie temperature and the clean-limit critical temperature (T^*), with preformed ferromagnetic regions of random orientations, has a huge magnetoresistance because small fields can easily align the moments of the ferromagnetic islands which leads to a percolative conductor in agreement with experiments [105].

This establishes qualitative similarities with “Giant magnetoresistant” multilayered materials. The quenched disorder simply triggers the stabilization of the cluster formation, but phase competition is the main driving force of the mixed state.

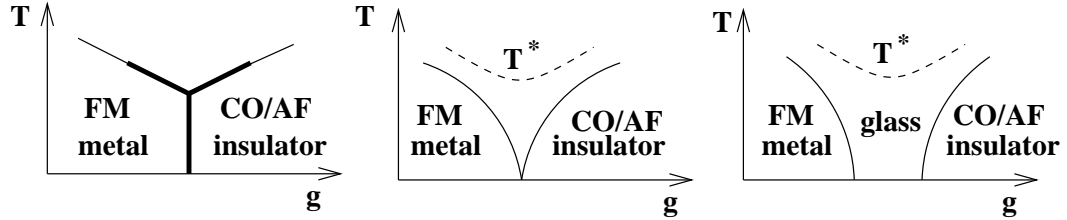


Figure 4.11. *Left* General phase diagram of two competing phases in the absence of quenched-disorder (or when this disorder is very weak). Thick (thin) lines denote first (second) order transitions. g is some parameter needed to change from one phase to the other. *Center* With increasing disorder, the temperature range with first-order transitions separating the ordered states is reduced, and eventually for a *fine-tuned* value of the disorder the resulting phase diagram contains a quantum critical point. In this context, this should be a rare occurrence. *Right* In the limit of substantial quenched disorder, a window without any long-range order opens at low temperature between the ordered phases. The new scale T^* , remnant of the clean-limit transition, is also shown. (From Ref. [7])

CHAPTER 5

CONCLUSIONS

One of the main results of the numerical studies presented in this dissertation is summarized in Fig. 5.1 where the “transport” phase diagram for diluted magnetic semiconductor systems is sketched. The low-temperature ferromagnetic phase is metallic (although often with poor metallicity). The *clustered state* between T^* and T_C has insulating properties, and the same occurs in a good portion of the phase diagram above these two characteristic temperatures.

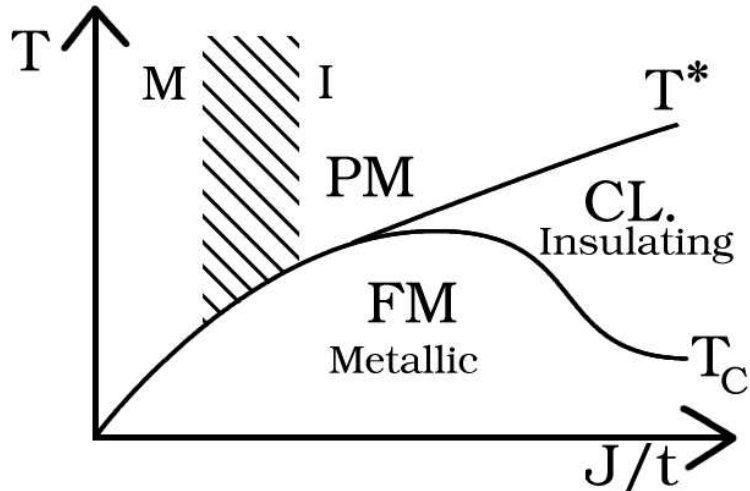


Figure 5.1. Sketch of the phase diagram indicating the conducting and insulating regions, as obtained by numerical simulation. The dashed area in the paramagnetic phase indicates the crossover region from a mild metallic weak coupling regime to a mild insulating strong coupling regime.

The Curie temperature is optimal (*i. e.*, the highest) in this intermediate zone, at fixed values of p and x (Chapter 2). In this regime, there is sufficient interaction

between the clusters to become globally ferromagnetic, and at the same time the coupling is sufficiently strong to induce a robust T_C . If chemical control over J/t were possible, this intermediate region would be the most promising to increase the Curie temperature (again, at fixed x and p).

However, it may even occur that DMS materials are already in the intermediate optimal range of J/t couplings. An indirect way to test this hypothesis relies on calculations of transport properties and its comparison with experiments. In particular, the experimentally measured d.c. resistivity ρ_{dc} of DMS compounds has a nontrivial shape with a (poor) metallic ($d\rho_{dc}/dT > 0$) behavior below T_C , which turns to insulating ($d\rho_{dc}/dT < 0$) at higher temperatures. The nontrivial profile resembles results reported in the area of manganites, which also have a metal-insulator transition as a function of temperature[59], although in those materials the changes in resistivity with temperature are far more dramatic than in DMSs. The formal similarities DMSs-manganites suggest a common origin of the ρ_{dc} vs. temperature curves. In Mn-oxides it is believed that above the Curie temperature, preformed ferromagnetic clusters with random orientations contribute to the insulating behavior[42, 59]. For DMSs, a similar rationalization can be envisioned if the state of relevance above T_C has preformed magnetic clusters. It was explained in Chapter 2 that the intermediate J/t region can have clusters without collapsing T_C to a very small value. At the Curie temperature, the alignment of these preformed moments leads to a metallic state. An explicit calculation of the resistivity – using techniques borrowed from the mesoscopic physics context – was provided in Section 3.3, and the results support the conjecture that clustered states can explain the transport properties of DMSs.

It is interesting to remark that in agreement with the clustered state described here, Timm and von Oppen have shown that *correlated* defects in DMSs are needed to describe experimental data[53]. Their simulations with Coulombic effects incorporated lead to cluster formation, with sizes well beyond those obtained from a random distribution of Mn sites as considered here. In this respect, the results

of Ref. [53] and [18] provide an even more dramatic clustered state than the one found in this work. If the Mn spins were not distributed randomly in our simulations but in a correlated manner, the state above T_C would be even more insulating than reported in Section 3.3 and the physics would resemble much closer that observed in manganites. Kaminski and Das Sarma have also independently arrived to a polaronic state [76] that qualitatively resembles the clustered state discussed here. It is also interesting that in ion-implanted (Ga,Mn)P:C experiments that reported a high Curie temperature, the presence of ferromagnetic clusters were observed and they were attributed to disorder and the proximity to a metal-insulator transition[106]. Even directly in (Ga,Mn)As, the inverse magnetic susceptibility deviates from the Curie law at temperatures above T_C [38], which may be an indication of an anomalous behavior.

In Sections 3.1 and 3.2, dynamical properties of a single-band model for diluted magnetic semiconductors were presented. Both the density of states and the optical conductivity calculations again support the view that the relevant regime of J/t is that of intermediate coupling, where carriers are only partially trapped near Mn spins, and locally ordered regions are present above the Curie temperature T_C . It was also found that the impurity band is formed but not completely separated from the main band in the regime of optimal Curie temperature.

Results found for DMSs are indicative of the key role that inhomogeneous clustered states play in many materials. Their existence leads to quite nontrivial results as discussed in Chapter 4. These states could be related to the heterophase states that were also studied in Ref. [107], but it is now that precise calculations are possible. Giant proximity effects in cuprates were analyzed in this context in Section 4.3. Our study revealed the possibility of colossal effects in materials where the superconducting state competes with the antiferromagnetic state. This could be observed in structures fabricated with superconducting and non-superconducting (clustered) films in close proximity, such that the bulk superconductivity in the

superconducting film acts as the “external field” to orient the superconducting phases in the clustered state. The study also provided a simple explanation for the increase of T_c with the number of layers, N_ℓ . In addition, our models suggest that different cuprates could have stripes, local coexistence, first-order transitions, or a glassy clustered state interpolating between the antiferromagnetic and superconducting phases.

The study of clustered states is rapidly developing into one of the most active areas of present day condensed matter physics. It is a field in an early stage of development, which will need a coordinated effort between theorists – mainly those with expertise in simulations – and experimentalists.

APPENDIX A

RIGOROUS RESULTS FOR KONDO LATTICE AND RELATED MODELS

A formal introduction to basic mathematical properties of the Kondo lattice models or, as they are sometimes called, spin fermion models is presented here. The emphasis is on exact, rigorous or well established results. In addition, exact results for Heisenberg and Ising models are presented.

A.1 Kondo Lattice Model

A.1.1 Definitions

Consider Eq. (1.1) and let $N = L^D$ be the number of lattice sites and N_e the number of electrons. The lattice spacing a is assumed to be unity. A basis for the Hilbert space of this Hamiltonian is given by considering all states with 0 electrons (there is only 1 of them), all states with 1 electrons (there are $2N$ of them), etc. The dimension of the (many-body) Hilbert space is 4^N .

Consider now the subset of all states of the basis of the many-body Hilbert space defined above formed by all one-electron states. It is easy to verify that this subset is closed and, therefore, it expands a Hilbert space of only $2N$ states, which is referred to as the one electron Hilbert space or the one-electron sector. The eigenvalues of H in the one electron-sector (for a given configuration of classical spins, \vec{S}_i), the one electron eigenvalues, are those obtained by diagonalizing H in that sector.

The 4^N eigenvalues of Hamiltonian Eq. (1.1) (for a given configuration of classical spins, \vec{S}_i) can be obtained by filling in all possible ways the eigenvalues of the one

electron sector. In other words: let E_λ be the eigenvalues of the one electron sector. Then any eigenvalue of H can be expressed by $\sum_{\lambda=1}^{2N} n_\lambda E_\lambda$, where the $n_\lambda \in \{0, 1\}$ are called the occupation numbers. Thus instead of having to diagonalize a $4^N \times 4^N$ matrix, it suffices to diagonalize a $2N \times 2N$ matrix. This property follows immediately from the quadratic form of Eq. (1.1) in the fermionic operators.

A.1.2 Symmetries

If E is a one-electron eigenvalue of Eq. (1.1) then $-E$ is also a one-electron eigenvalue. Moreover, the one-electron eigenvectors and eigenvalues of Eq. (1.1) are invariant to the change t into $-t$, which can be proved by applying the canonical transformation $\tilde{c}_{\vec{r}} = \exp(i\vec{\pi} \cdot \vec{r}) c_{\vec{r}}$, where $\vec{\pi}$ is a vector with all its Cartesian components equal to the number π .

The one-electron eigenvectors and eigenvalues of Eq. (1.1) are invariant to the change J into $-J$. This follows from the invariance of Eq. (1.1) to the change J into $-J$ and S_i into $-S_i$ for all i . But since (i) H is invariant with respect to global rotation for the spins (S_i) and (ii) S_i into $-S_i$ is such a transformation then the above proposition follows.

The magnetic properties of the system are invariant to the change $\mu \rightarrow -\mu$. Furthermore, the density of electrons of a system with chemical potential μ plus the corresponding density for a system with chemical potential $-\mu$ is 2. This can be seen by applying the canonical transformation $d_{i\sigma} = c_{i\sigma}^\dagger$. In other words, the model is particle-hole symmetric.

A.1.3 Ground State Properties

When $J = 0$ the one-electron eigenvalues of Eq. (1.1) on a cubic lattice with periodic boundary conditions are

$$e_{(k_x, k_y, k_z)} = -2t(\cos(k_x) + \cos(k_y) + \cos(k_z)). \quad (\text{A.1})$$

Assuming $S_i = (1, 0, 0)$ for all i , *i. e.* a perfect ferromagnet, then the one-electron eigenvalues of Eq. (1.1) are $E_k = e_k - J$ and $E_k = e_k + J$.

Given a site i of a D -dimensional lattice, the *parity* of i is defined as -1 to the power of the sum of its Cartesian coordinates. Assuming $S_i = (\text{parity}(i), 0, 0)$ for all i , *i. e.* a perfect antiferromagnet, then the one-electron eigenvalues are given by $E_k = \pm \sqrt{e_k^2 + J^2}$ and k is restricted to half the Brillouin zone.

If N is even and J is sufficiently strong, when $N_e = N/2$, *i. e.*, when the system is quarter-filled, the ground state of Eq. (1.1) is ferromagnetic. On the other hand for $N_e = N$, the ground state of the model is anti-ferromagnetic [42].

Even though, no explicit Coulombic interaction is present in this model, it can be shown that when $N \rightarrow \infty$, the double occupancy in the ferromagnetic ground state tends to zero.

A.2 Heisenberg Models

The Kondo lattice model can be approximated by a Heisenberg model with possibly long range interactions for small values of the coupling. Therefore, below is a list of some relevant theorems related to Heisenberg and Ising models. However, the exact theorems that will be presented are based on particular assumptions regarding the Hamiltonian, for example short-range interactions. In the case of Kondo lattice or spin-fermion models, the effective Hamiltonian for the localized spins can include interactions at all distances, as well as terms with multiple spin interactions, which will limit the usefulness of these theorems.

A.2.1 Short Range Interactions

The one-dimensional and two-dimensional *quantum* Heisenberg models with short range interactions have no finite temperature phase transition[108][109].

For the quantum Heisenberg model Mermin and Wagner's Theorem can be expressed as follows. Every Hamiltonian

$$\mathcal{H} = \frac{1}{2} \sum_{ij} J_{ij} \mathbf{S}_i \cdot \mathbf{S}_j - h S_{\mathbf{q}}^z, \quad (\text{A.2})$$

with short-range interactions that obey

$$\bar{J} = \frac{1}{2\mathcal{N}} \sum_{ij} |J_{ij}| |\mathbf{x}_i - \mathbf{x}_j|^2 < \infty \quad (\text{A.3})$$

has no spontaneously broken spin symmetry at finite temperatures in one and two dimensions,

$$\lim_{h \rightarrow 0^+} \lim_{\mathcal{N} \rightarrow \infty} m_{\mathbf{q}}(h, \mathcal{N}) = 0; \quad (\text{A.4})$$

where

$$S_{\mathbf{q}}^z = \sum_i e^{i\mathbf{q} \cdot \mathbf{x}_i} S_{\mathbf{q}}^z \quad (\text{A.5})$$

and

$$m_{\mathbf{q}}(h) = \frac{1}{\mathcal{N}Z} \text{Tr} [e^{-\mathcal{H}(h)/T} S_{\mathbf{q}}^z] \quad (\text{A.6})$$

The Hamiltonian Eq (A.2) has a continuous symmetry. The theorem is valid for both, ferromagnets and antiferromagnets, and for any value of S . Ferromagnetism is ruled out by taking $\mathbf{q} = 0$, and antiferromagnetism by choosing it such that $e^{i\mathbf{q} \cdot \mathbf{x}} = 1$ when \mathbf{x} connects sites in the same sublattice, and -1 when it connects sites in different sublattices. When $J_{ij} = |\mathbf{x}_i - \mathbf{x}_j|^{-p}$, condition (A.3) holds if $p > 3$ in 1 dimension or $p > 4$ in 2 dimensions.

The one-dimensional and two-dimensional *classical* Heisenberg models with short range interactions have no finite temperature phase transition[108][109].

Since the theorem above holds for all S , it holds also for the classical (S -independent) limit of the Heisenberg model:

$$\mathcal{H}^{cl} = \frac{1}{2} \sum_{ij} J_{ij}^{cl} \Omega_i \cdot \Omega_j - h^{cl} \Omega_{\mathbf{q}}^z \quad (\text{A.7})$$

where Ω are c-number unit vectors. The correspondence between Eq (A.2) and Eq (A.7) is given by scaling the parameters: $J_{ij} S(S+1) \rightarrow J^{cl}$, $hS \rightarrow h^{cl}$ and

$m_{\mathbf{q}}/S \rightarrow m_{\mathbf{q}}^{cl}$. Thus, the same result applies for the classical model Eq. (A.7), and is valid for both, ferromagnets and antiferromagnets.

The quantum and classical Heisenberg models with short range interactions and the additional condition that there exists a gap in the excitation spectrum, have no phase transition, even at $T = 0$, in one and two dimensions[108].

Mermin and Wagner’s theorem does not apply at $T = 0$. However, if

$$E_m - E_0 > \Delta, \quad \forall m \neq 0, \quad (\text{A.8})$$

where Δ is independent of h , \mathcal{N} , the ground state of the Heisenberg model must be disordered.

As an example, the antiferromagnetic integer spin chains are known to exhibit the “Haldane gap” in their spectrum and thus a disordered ground state. However, gapless excitations do not imply long-range order: the spin half Heisenberg antiferromagnet in one dimension, for instance, has gapless excitations but no long-range order at $T = 0$.

The ground state of the one dimensional Heisenberg antiferromagnet with nearest neighbor interactions, has no long-range order for any value of the spin[110].

The ground state of the two dimensional *quantum* Heisenberg antiferromagnet is ordered for $S \geq 1$ [111]. (In other words, there is Neel order for the two dimensional square lattice if the spin is at least 1).

A.2.2 Long range interactions

The *classical* Heisenberg model with (long range) interactions of the form r^{-p} in one dimension has a finite temperature phase transition for $1 < p < 2$ [112].

The *classical* Heisenberg model with (long range) interactions of the form r^{-p} in two dimension has a finite temperature phase transition for $2 < p < 4$ [112].

The *quantum* Heisenberg ferromagnet in d dimensions has a finite temperature phase transition in the region $d < p < 2d$ and no finite temperature phase transition for $p \geq 2d$ [113]. The Hamiltonian is assumed to be[113]:

$$\mathcal{H} = -\frac{1}{2} \sum_j \sum_\rho J(\rho) \mathbf{S}_j \cdot \mathbf{S}_{j+\rho} - H \sum_j S_j^z, \quad (\text{A.9})$$

and the strength of the coupling is defined by

$$\lim_{N \rightarrow \infty} \frac{J(\rho)}{J_0} = \begin{cases} 0 & (\rho = 0) \\ |\rho|^{-p} & (\text{otherwise}) \end{cases} \quad (\text{A.10})$$

where N is the number of sites and J_0 means the nearest-neighbor interaction, which is positive. The ground state for the case $p = 2$ was found exactly by B. S. Shastri [114] and independently by F. D. M. Haldane [115].

Let $J(n) = n^{-\alpha}$. Then the *quantum* Heisenberg isotropic antiferromagnet

$$-H = \sum_{n \neq m} (-1)^{n-m} J(|n-m|) \mathbf{S}_n \cdot \mathbf{S}_m, \quad (\text{A.11})$$

of spin S has a first order phase transition if S is sufficiently large, at some finite temperature, for $1 < \alpha < 2$ [112].

A.3 Ising Models

The one dimensional Ising model with interactions of the form r^{-p} has a finite temperature phase transition when $1 < p \leq 2$ and no long range order when $p > 2$ [116][117].

The two dimensional Ising model is ferromagnetic[118]. The two dimensional Ising model in the absence of a magnetic field was solved exactly by Onsager[119].

APPENDIX B

POLYNOMIAL EXPANSION METHOD

In the conventional Monte Carlo technique for the model considered so far, the Hamiltonian is numerically diagonalized for each spin configuration $\{\theta_i, \phi_i\}$ as explained before, to obtain all the eigenvalues. Eq. (1.9) is used then to perform the Monte Carlo simulation. However, the exact eigenvalues contain more than enough information for the purpose of performing practical Monte Carlo calculations: it is sufficient to know the density of states within required accuracy. That is the basis for the method proposed by N. Furukawa et al. [64], where instead of the eigenvalues of the Hamiltonian, the density of states (DOS) is estimated by using a moment expansion with orthogonal polynomials. The Chebyshev polynomials are convenient in the moment expansion, which are defined recursively by:

$$T_{m+1}(x) = 2xT_m(x) - T_{m-1}(x), \quad (\text{B.1})$$

with $T_0 = 1$ and $T_1 = x$ for $-1 \leq x \leq 1$. First, a renormalized Hamiltonian $X(\{x_i\})$ is defined whose eigenvalues are between -1 and 1 by $H' = aX + b$ with:

$$a = (E_{max} - E_{min})/2, \quad b = (E_{max} + E_{min})/2, \quad (\text{B.2})$$

where $E_{max}(E_{min})$ is a highest (lowest) eigenvalue of the Hamiltonian H . Then, the m -th Chebyshev moment of the density of states is defined by:

$$\mu_m = \int_{-1}^1 T_m(\epsilon) D(\epsilon) d\epsilon. \quad (\text{B.3})$$

Once the moments μ_m are calculated, the density of states is inversely obtained by

$$D(\epsilon) = \frac{1}{\pi\sqrt{1-\epsilon^2}} \left[\mu_0 + 2 \sum_{m \geq 1} \mu_m T_m(\epsilon) \right]. \quad (\text{B.4})$$

The expectation value of an operator A is calculated by

$$\langle A \rangle = \int_{-1}^1 A(\epsilon) D(\epsilon) d\epsilon = \mu_0 \nu_0 + 2 \sum_{m \geq 1} \mu_m \nu_m, \quad (\text{B.5})$$

where the moments of A are

$$\nu_m = \int_{-1}^1 \frac{d\epsilon}{\pi\sqrt{1-\epsilon^2}} A(\epsilon) T_m(\epsilon). \quad (\text{B.6})$$

In particular, the effective action is obtained from

$$S_{eff} = \mu_0 s_0 + 2 \sum_{m \geq 1} \mu_m s_m, \quad (\text{B.7})$$

where

$$s_m = - \int_{-1}^1 \frac{N_{dim} d\epsilon}{\pi\sqrt{1-\epsilon^2}} \log [1 + e^{-\beta(a\epsilon+b-\mu)}] T_m(\epsilon). \quad (\text{B.8})$$

The moments of the density of states are calculated for Eq. (B.7) by

$$\mu_m = \frac{1}{N_{dim}} Tr \{ T_m(X) \} = \frac{1}{N_{dim}} \sum_{\nu=1}^{N_{dim}} \langle \nu | T_m(X) | \nu \rangle, \quad (\text{B.9})$$

where $|\nu\rangle$ forms a complete basis of the Hamiltonian. The calculation of a moment involves a vector product:

$$\mu_m = \frac{1}{N_{dim}} \sum_{\nu=1}^{N_{dim}} \langle \nu; 0 | \nu; m \rangle, \quad (\text{B.10})$$

which costs a CPU time that scales as $O(N_{dim})$. The definition of the vectors $|\nu; m\rangle$ is:

$$|\nu; m\rangle = T_m(X) |\nu\rangle, \quad (\text{B.11})$$

and are calculated recursively by using the relation

$$|\nu; m+1\rangle = 2X |\nu; m\rangle - |\nu; m-1\rangle. \quad (\text{B.12})$$

In order to take advantage of this method, the Hamiltonian must be sparse, as it is in the case of DMSs and most spin fermion models. The matrix-vector multiplication

must be done as a sparse matrix-vector multiplication. Moreover, moments up to m -th order can be calculated from those only up to $m/2$ -th order by using recursive relations of Chebyshev polynomials. A total CPU time to compute the moments μ_m up to order $m = M$ scales as $O(N_{dim}^2 M)$.

The present method becomes “exact”, that is, equivalent to the direct diagonalization of the Hamiltonian in the conventional technique when the summations in Eq. (B.4) and Eq. (B.5) are taken up to infinite order. In actual calculations, the infinite summations are approximated in these equations by finite summations up to $m = M$. The truncation error of the effective action, ΔS_{eff} , which is a crucial quantity in Monte Carlo updates, becomes exponentially small as a function of M . The reason for this is that the moments s_m in Eq. (B.8) become exponentially small with m . Thus the approximation is justified even for small values of M . The key point of the algorithm, as explained before, is that it can be parallelized, because the calculation of the moments in Eq. (B.10) for each basis ket $|\nu\rangle$ is independent. In this way the basis can be partitioned in such a way that each processor calculates the moments corresponding to a portion of the basis. The CPU time to calculate the moments on each processor is proportional to $N_{dim}^2 M/N_{PE}$, where N_{PE} is the number of processors. It is important to remark that the data to be moved between different nodes are small compared to calculations in each node. Indeed, the communication time is proportional to MN_{PE} and communication among nodes is mainly done here to add up all the moments. The possibility of parallelizing this algorithm can be contrasted with the conventional method where a matrix diagonalization is performed at every Monte Carlo step; in that case the calculations must be serial because it is difficult to make an efficient parallelization of the matrix diagonalization.

APPENDIX C

TRUNCATED POLYNOMIAL EXPANSION METHOD

The calculations for the Boltzmann weights performed in Appendix B can further be extended by introducing truncated matrix operations. In addition, the trace operation performed to obtain the effective action can also be truncated in order to reduce the computational complexity. Using all these reliable approximations the CPU time scales as $O(N)$. The description of the algorithm presented in this Appendix follows closely Ref. [8].

As an example to explain the method, consider a simple model which has the Hamiltonian matrix in the form

$$H_{ij}(\phi) = \begin{cases} g\phi_i & i = j, \\ -t & i \text{ and } j \text{ are nearest neighbors,} \\ 0 & \text{otherwise.} \end{cases} \quad (\text{C.1})$$

where t is the nearest neighbor hopping energy for spinless electrons while g is the electron-field coupling constant. The local adiabatic field $\phi = \{\phi_i\}$ is defined for every lattice site. Therefore, the Hamiltonian matrix $H(\phi)$ is a sparse matrix with $N_{\text{dim}} = N$.

C.1 Truncation of matrix products

In order to obtain $\mu_m(\nu)$ for $m = 0, \dots, M$ from Eq. (B.12), matrix-vector multiplications throughout the Hilbert space are necessary, which give $O(MN)$ computational complexity. Here we introduce a truncation of the matrix-vector multiplications in order to reduce the computational complexity.

Let $|\nu\rangle_i = \delta_{i\nu}$ for the orthonormal set in Eq. (B.11). Since $|\nu; 0\rangle_i$ is non-zero only at $i = \nu$, we have $|\nu; 1\rangle \neq 0$ only at $i = \nu$ as well as at nearest neighbors of ν . Namely, due to the sparse nature of the Hamiltonian matrix (C.1), it is not necessary to calculate all the other vector elements. Similarly, if one keeps track of a set of indices with $|\nu; m-1\rangle_i \neq 0$, the calculation of vector elements $|\nu; m\rangle_i$ can be restricted to limited numbers of indices, so that the computational complexity is much reduced.

The matrix-vector product in Eq. (B.12) can be viewed as a transfer-matrix multiplication to a state vector, which expresses a diffusive propagation of a wavefunction. Consider an initial vector $|\nu; 0\rangle = \vec{e}(\nu)$, which expresses an electron state localized at site ν . Each time the Hamiltonian matrix H is multiplied to obtain $|\nu; m\rangle$, electrons hop to nearest neighbors. As a consequence, the sites with non-zero vector elements $|\nu; m\rangle_i$ spread out as m increases. In Fig. C.1 a schematic illustration is given for the propagation steps. The process also resembles the diffusion of the probability distribution function in a random-walk system.

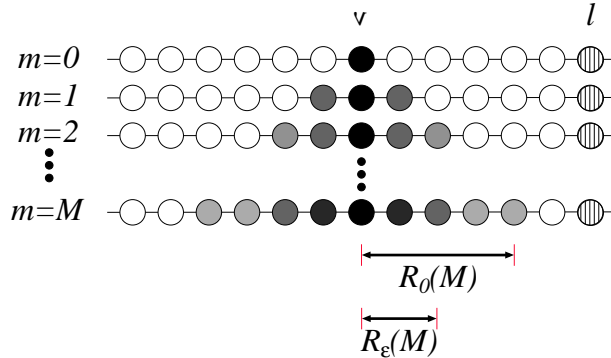


Figure C.1. A sketch for the propagation of vector elements. The vertical axis gives the matrix-vector multiplication steps. Circles aligned in the horizontal direction represent lattice sites. Filled circles show sites with non-zero vector elements, and darkness of them schematically illustrates amplitudes of the vector elements. The initial vector gives a localized state at site ν . See also the discussion in §C.2 (from Ref. [8]).

Let us define the distance between site i and site ν -th, denoted as $\|i - \nu\|$, by the minimum number of hops for an electron to transfer from the i -th site to the ν -th site. On hypercubic lattices, this gives the ‘‘Manhattan distance’’. We define the range of propagation $R_0(m)$ by the longest distance that an electron can hop by m steps of the matrix-vector multiplication in Eq. (B.12). Since sites which are outside of the range of propagation have zero vector elements, *i.e.*,

$$|\nu; m\rangle_i = 0 \quad \text{if } \|i - \nu\| > R_0(m), \quad (\text{C.2})$$

there is contribution to the calculations of $\mu_m(\nu)$ as well as $|\nu; m + 1\rangle$ from these sites. This means that we may perform our matrix-vector calculation only within the neighbors of ν which satisfies $\|i - \nu\| \leq R_0(m)$ to obtain exact results. In the present model (C.1) $R_0(m) = m$, and the number of sites which contributes to the overall calculation of $\mu_m(\nu)$ ($m \leq M$) is proportional to M^d instead of N when every site on the lattice is taken into account. Here d is the spacial dimension of the lattice. By introducing this restriction, the computational complexity to obtain $\mu_m(\nu)$ ($m \leq M$) is reduced from $O(MN)$ to $O(M^{d+1})$ without any cost for the computational accuracies.

The range where calculations are restricted can be further reduced by introducing a threshold ϵ for the vector elements. When the absolute values of the vector elements $|\nu; m\rangle_i$ are small enough, such terms in the calculation of $\mu_m(\nu)$ and $|\nu; m + 1\rangle$ can be neglected. The range of propagation $R_\epsilon(m)$ is defined by the longest distance $\|i - \nu\|$ such that the absolute value of the vector element on the i -th site exceeds the threshold, $|\nu; m\rangle_i \geq \epsilon$. In Fig. C.1 a schematic illustration is given. Then,

$$|\nu; m\rangle_i < \epsilon \quad \text{if } \|i - \nu\| > R_\epsilon(m), \quad (\text{C.3})$$

and contributions to $\mu_m(\nu)$ from sites outside of the range are negligible if values of ϵ are taken appropriately.

Since the diffusion length is proportional to the square-root of the time-steps in general, $R_\epsilon(m) \propto \sqrt{m}$ for $\epsilon > 0$. Then, by introducing a threshold ϵ and restricting

the calculation within $\|i - \nu\| \leq R_\epsilon(m)$, the number of sites which contributes to $\mu_m(\nu)$ scales as $O(M^{d/2})$. Therefore the computational complexity to obtain $\mu_\nu(m)$ ($m \leq M$) is further reduced to $O(M^{d/2+1})$ with the accuracies of $O(\epsilon)$. (To be more specific, the number of sites neglected by this treatment is $O(M^d)$ for the calculation of μ_m ($m = 0, \dots, M$), so the total error for the calculation of the Boltzmann weight is $O(M^{d+1}\epsilon)$.)

The procedure will now be extended to general cases where an index for fermion degrees of freedom represents a combination of site, orbital and spin. Since the basis set to define the Hamiltonian matrices:

$$\hat{\mathcal{H}}(\phi) = \sum_{i,j} c_i^\dagger H_{ij} c_j \quad (\text{C.4})$$

can be taken arbitrary, we may also consider a system with no well-defined geometrical distance between indices. Nevertheless, as long as the Hamiltonian matrices are sparse, we can generalize the algorithm as follows.

The subspace $\mathcal{N}_0(\nu, m)$ is defined as the set of neighboring indices of the initial index ν which are within the range of propagation by m steps,

$$\mathcal{N}_0(\nu, m) = \bigcup_{m'=0}^m \{i \mid |\nu; m'\rangle_i \neq 0\}. \quad (\text{C.5})$$

In the previous example, $\mathcal{N}_0(\nu, m)$ is a set of indices within the range of $R_0(m)$ from ν . Then, the matrix product operations within the subspace $\mathcal{N}_0(\nu, m)$ can be restricted, since

$$|\nu; m\rangle_i = 0 \quad \text{if } i \notin \mathcal{N}_0(\nu, m), \quad (\text{C.6})$$

so that there is no contribution to $\mu_m(\nu)$ from outside of $\mathcal{N}_0(\nu, m)$.

Similarly, the subspace $\mathcal{N}_\epsilon(\nu, m)$ is defined as the set of neighboring indices of ν where absolute values of the vector elements exceed the threshold ϵ ,

$$\mathcal{N}_\epsilon(\nu, m) = \bigcup_{m'=0}^m \{i \mid \|\nu; m'\rangle_i\| > \epsilon\}. \quad (\text{C.7})$$

In the previous example, $\mathcal{N}_\epsilon(\nu, m)$ roughly corresponds to a set of sites within the range of $R_\epsilon(m)$ from ν . By making truncations of the matrix product operations

within the restricted subspace $\mathcal{N}_\epsilon(\nu, m)$, approximate results are obtained for $\mu_m(\nu)$ within errors of $O(\epsilon)$, since

$$||\nu; m'\rangle_i| < \epsilon \quad \text{if } i \notin \mathcal{N}_\epsilon(\nu, m), \quad (\text{C.8})$$

so that contributions from outside of $\mathcal{N}_\epsilon(\nu, m)$ are negligible.

C.2 Truncation of trace operations

In order to obtain S_{eff} directly from Eqs. (B.7) and (B.8), a trace operation throughout the Hilbert space is necessary, which gives $O(N)$ computational complexity. Here we introduce a truncation of the trace operation in order to reduce the computational complexity.

The probability of the MC update from an old field configuration ϕ^{old} to a new configuration ϕ^{new} , which is given by the ratio of the Boltzmann weights:

$$\frac{P(\phi^{\text{new}})}{P(\phi^{\text{old}})} = \exp(-\Delta S_{\text{eff}}), \quad (\text{C.9})$$

where ΔS_{eff} is the difference of the effective action. Using PEM up to the M -th order, we have

$$\Delta S_{\text{eff}} = S_{\text{eff}}(\phi^{\text{new}}) - S_{\text{eff}}(\phi^{\text{old}}) \simeq \sum_{m=0}^M s_m \sum_{\nu}^{N_{\text{dim}}} \Delta \mu_m(\nu), \quad (\text{C.10})$$

where

$$\Delta \mu_m(\nu) = \langle \nu | \nu; m \rangle^{\text{new}} - \langle \nu | \nu; m \rangle^{\text{old}}. \quad (\text{C.11})$$

Here, $|\nu; m\rangle^\alpha$ for $\alpha = (\text{old}, \text{new})$ is defined by

$$|\nu; m\rangle^\alpha = T_m(H(\phi^\alpha))|\nu\rangle, \quad (\text{C.12})$$

and we choose $|\nu\rangle_i = \delta_{i\nu}$. Summation over ν in Eq. (C.10) is the trace operation in Eq. (B.9).

Now consider a local update of the adiabatic fields in the present exemplified model (C.1). Let us choose a site l and try a local update on the site $\phi_l^{\text{old}} \rightarrow \phi_l^{\text{new}}$,

while we have $\phi_i^{\text{old}} = \phi_i^{\text{new}}$ for $i \neq l$. In this case, the change of the Hamiltonian matrix $H(\phi^{\text{old}}) \rightarrow H(\phi^{\text{new}})$ exists only at the l, l -th matrix element, while we have $H_{ij}(\phi^{\text{old}}) = H_{ij}(\phi^{\text{new}})$ elsewhere.

Taking a site ν which is distant enough from the updated site l so that $\|\nu - l\| > R_0(M)$ is satisfied, and consider the diffusion of the vectors $|\nu; m\rangle^{\text{old}}$ and $|\nu; m\rangle^{\text{new}}$. In this case, we have $|\nu; m\rangle^{\text{old}} = |\nu; m\rangle^{\text{new}}$ and hence $\Delta\mu_m(\nu) = 0$. The reason is as follows. For $m \leq M$, the region where the state vectors propagate does not reach the site l , since $R_0(m) < \|\nu - l\|$ is satisfied. In Fig. C.1 a schematic illustration is given. The matrix elements that are operated to the vectors during the diffusion processes are identical between old and new configurations. This makes

$$|\nu; m\rangle_i^{\text{old}} = |\nu; m\rangle_i^{\text{new}} \quad (\text{C.13})$$

for i which satisfies $\|i - k\| \leq R_0(m)$. At the same time, by the definition of $R_0(m)$ we have $|\nu; m\rangle_i^{\text{old}} = |\nu; m\rangle_i^{\text{new}} = 0$ for i such that $\|i - \nu\| > R_0(m)$. Then, we have $|\nu; m\rangle_i^{\text{old}} = |\nu; m\rangle_i^{\text{new}}$ in the entire space.

In other words, $\Delta\mu_m(\nu) \neq 0$ for $m \leq M$ only if k is close enough to l so that the propagation from the site k reaches the site l within M steps. Therefore, it is sufficient to take the summation over ν in Eq. (C.10) only within the vicinity of l which satisfies $\|\nu - l\| \leq R_0(M)$. Namely, the trace operation may be restricted to a subspace which has $O(M^d)$ sites so that the computational complexity for the trace operations is reduced from $O(N)$ to $O(M^d)$.

Furthermore, a truncation of trace operations is introduced which gives approximate results with a reduced computational complexity. A general case with sparse Hamiltonian matrices will be considered. For a moment we restrict ourselves to an update of the adiabatic field where the matrix elements of $H(\phi^{\text{old}})$ and $H(\phi^{\text{new}})$ are identical except for the l, l -th element.

Consider an initial vector at ν and the propagation of the vectors for $H(\phi^{\text{old}})$ and $H(\phi^{\text{new}})$, which gives the set of neighboring indices $\mathcal{N}_\epsilon^{\text{old}}(\nu, m)$ and $\mathcal{N}_\epsilon^{\text{new}}(\nu, m)$,

respectively. If $l \notin \mathcal{N}_\epsilon^{\text{new}}(\nu, M)$ and $l \notin \mathcal{N}_\epsilon^{\text{old}}(\nu, M)$ are satisfied, both $\vec{v}^{\text{old}}(\nu, m)$ and $\vec{v}^{\text{new}}(\nu, m)$ are approximately confined within the subspace where matrix elements of the Hamiltonian are identical, and do not reach the index l . Then

$$|\nu; m\rangle^{\text{old}} \simeq |\nu; m\rangle^{\text{new}}, \quad (\text{C.14})$$

within the error threshold ϵ , and therefore $\Delta\mu_m(k) = O(\epsilon)$ is satisfied. In other words, only indices in the vicinity of l where effective propagations to l occur within M steps should be considered for the calculations of $\Delta\mu_m(\nu)$.

This means that the trace operation in Eq. (C.10) can be restricted to the vicinity of l , defined by a set of indices ν where $l \in \mathcal{N}_\epsilon^{\text{new}}(\nu, M)$ or $l \in \mathcal{N}_\epsilon^{\text{old}}(\nu, M)$ are satisfied. Using Eq. (C.12) and the Hermiticity of the Hamiltonian matrix polynomials

$$T_m(H)|_{l\nu} = (T_m(H)|_{\nu l})^*, \quad (\text{C.15})$$

we have $|\nu; m\rangle_l^\alpha = |\nu; m\rangle_l^{\alpha*}$ for $\alpha = (\text{old}, \text{new})$. Namely, if and only if $\nu \in N_\epsilon^\alpha(l, M)$, we have $l \in N_\epsilon^\alpha(\nu, M)$. Therefore, the trace operation can be restricted to a subspace defined by

$$\mathcal{V}_\epsilon(l, M) \equiv \mathcal{N}_\epsilon^{\text{old}}(l, M) \cup \mathcal{N}_\epsilon^{\text{new}}(l, M). \quad (\text{C.16})$$

Due to the diffusive nature of the propagation, the number of indices in $\mathcal{N}_\epsilon^{\text{old}}(l, M)$ and $\mathcal{N}_\epsilon^{\text{new}}(l, M)$ is $O(M^{d/2})$ on usual lattice systems. The truncated trace operation within \mathcal{V}_ϵ reduces the computational complexity from $O(N)$ to $O(M^{d/2})$ with errors of $O(\epsilon)$.

This algorithm can be extended to cases where a local update modulates matrix elements for multiple indices. An example is the case where fields are coupled to off-diagonal matrix elements, *e.g.*, hopping amplitudes. Let us consider a case where a local update modulates the l, l' -th matrix element. Differences between new and old vectors exist if the propagations of the vectors reach either of the indices l or l' . Then, it is necessary to consider a sum of vicinities centered at l and l' ,

$$\mathcal{V}_\epsilon^{\text{tot}} = \mathcal{V}_\epsilon(l, M) \cup \mathcal{V}_\epsilon(l', M), \quad (\text{C.17})$$

and make trace operations within $\mathcal{V}_\epsilon^{\text{tot}}$. In a general case where a number of matrix elements are modulated, we need to consider all the indices associated with modulated matrix elements. We define \mathcal{C} as a set of indices where matrix elements are modulated by the update,

$$\mathcal{C} = \{l \mid \exists l', H_{ll'}(\phi^{\text{old}}) \neq H_{ll'}(\phi^{\text{new}})\}. \quad (\text{C.18})$$

Then, the total vicinity $\mathcal{V}_\epsilon^{\text{tot}}$ is given by

$$\mathcal{V}_\epsilon^{\text{tot}} = \bigcup_{l \in \mathcal{C}} \mathcal{V}_\epsilon(l, M), \quad (\text{C.19})$$

and the trace operations are performed within $\mathcal{V}_\epsilon^{\text{tot}}$, *i.e.*,

$$\Delta S_{\text{eff}} \simeq \sum_{m=0}^M f_m \sum_{\nu \in \mathcal{V}_\epsilon^{\text{tot}}} \Delta \mu_m(\nu). \quad (\text{C.20})$$

As long as MC updates are local, the number of indices in \mathcal{C} is $O(N^0)$, so that the computational complexity for the trace operation will be $O(M^{d/2})$.

C.3 Comparison with previous methods

Thus we see that the PEM using truncated matrix operations reduces the total computational complexity for one local update from $O(MN^2)$ to $O(M^{d+1})$, by combining threshold truncations for both matrix products and trace operations. Hereafter we refer to the improved method in this section with truncations of matrix operations as the truncated PEM, whereas the original method described in Appendix B is the full PEM. In Table C.1 we summarize the computational complexities for various algorithms for comparison.

It is important to emphasize that the restriction of matrix operations within $\mathcal{N}_0(\nu, M)$ produces identical results for $\mu_m(\nu)$ to those obtained by the full PEM, with a reduced computational complexity. In addition, $\mathcal{N}_{\epsilon \rightarrow 0}(\nu, M) = \mathcal{N}_0(\nu, M)$. This implies that the introduction of the threshold ϵ is a controlled approximation

Table C.1. Computational complexities to perform calculations of $\mu_m(\nu)$, trace operations, calculations of the Boltzmann weight ratio through ΔS_{eff} , and a MC step with local updates in total. Here, full PEM and TPEM stand for the full polynomial expansion method and the truncated polynomial expansion method, respectively. Threshold for the truncated PEM is described by ϵ (From Ref. [8]).

Algorithm	$\mu_m(\nu)$	Trace	ΔS_{eff}	Total
Diag.	–	–	$O(N^3)$	$O(N^4)$
full PEM	$O(MN)$	$O(N)$	$O(MN^2)$	$O(MN^3)$
TPEM				
$\epsilon = 0$	$O(M^{d+1})$	$O(M^d)$	$O(M^{2d+1})$	$O(M^{2d+1}N)$
$\epsilon \neq 0$	$O(M^{\frac{d}{2}+1})$	$O(M^{\frac{d}{2}})$	$O(M^{d+1})$	$O(M^{d+1}N)$

in the sense that $\mu_m(\nu)$ are obtained with an arbitrary accuracy by an appropriate choice of ϵ , with further reduced computational complexities.

REFERENCES

- [1] H. Ohno. Making nonmagnetic semiconductors ferromagnetic. *Science*, 281:951, 1998.
- [2] S. J. Potashnik, K. C. Ku, S. H. Chun, J. J. Berry, N. Samarth, and P. Schiffer. Effects of annealing time on defect-controlled ferromagnetism in $\text{Ga}_{1-x}\text{Mn}_x\text{As}$. *Appl. Phys. Lett.*, 79:1495, 2001.
- [3] H. Ohno. Properties of ferromagnetic III-V semiconductors. *Journal of Magnetism and Magnetic Materials*, 200:110, 1999.
- [4] S. Katsumoto, T. Hayashi, Y. Hashimoto, Y. Iye, Y. Ishiwata, M. Watanabe, R. Eguchi, T. Takeuchi, Y. Harada, S. Shin, and K. Hirakawa. Magnetism and metal-insulator transition in iii-v based diluted magnetic semiconductors. *Mater. Sci. and Eng. B*, 84:88, 2001.
- [5] E. Dagotto. Correlated electrons in high temperature superconductors. *Review of Modern Physics*, 66:763, 1994.
- [6] G. Burns. *High-Temperature Superconductivity: An Introduction*. Academic Press, Inc., San Diego, CA, 1992.
- [7] G. Alvarez and E. Dagotto. cond-mat/0305628, To be published in the Journal of Magnetism and Magnetic Materials, 2003.
- [8] N. Furukawa and Y. Motome. Order N Monte Carlo algorithm for fermion systems coupled with fluctuating adiabatical fields. *cond-mat*, 03:0308298, 2003.
- [9] H. Ohno, A. Shen, F. Matsukura, A. Oiwa, A. Endo, S. Katsumoto, and Y. Iye. (Ga,Mn)As: A new diluted magnetic semiconductor based on GaAs. *Appl. Phys. Lett.*, 69:363, 1996.
- [10] H. Ohno, H. Munekata, T. Penney, S. von Molnár, , and L. L. Chang. Magnetotransport properties of p -type (In,Mn)As diluted magnetic III-V semiconductors. *Phys. Rev. Lett.*, 68:2664, 1992.
- [11] Hidenobu Hori, Saki Sonoda, Takahiko Sasaki, Yoshiyuki Yamamoto, Saburo Shimizu, Ken ichi Suga, and Koichi Kindo. High- T_C ferromagnetism in diluted magnetic semiconducting GaN:Mn films. *Physica B*, 324:142, 2002.

- [12] I. Kuryliszyn, T. Wojtowicz, X. Liu, J. K. Furdyna, W. Dobrowolski, J.-M. Broto, M. Goiran, O. Portugall, H. Rakoto, and B. Raquet. Low temperature annealing studies of $\text{Ga}_{1-x}\text{Mn}_x\text{As}$. *J. Semicond.*, 16:63, 2003.
- [13] T. Dietl. III-V and II-VI Mn-based ferromagnetic semiconductors. In B. Kramer, editor, *Advances in Solid State Physics*. Springer Verlag, Berlin, 2003.
- [14] T. Dietl. Nitrides as spintronic materials. *Phys. Stat. Solidi (b)*, 240:433, 2003.
- [15] S. Datta and B. Das. Electronic analog of the electro-optic modulator. *Appl. Phys. Lett.*, 56:665, 1990.
- [16] M. Johnson. Spin injection in metals and semiconductors. *Semicond. Sci. Technol.*, 17:298, 2002.
- [17] Igor Zutic, Jaroslav Fabian, and S. Das Sarma. Spin-polarized transport in inhomogeneous magnetic semiconductors: Theory of magnetic/nonmagnetic p-n junctions. *Phys. Rev. Lett.*, 88:066603, 2002.
- [18] C. Timm. Disorder effects in diluted magnetic semiconductors. *J. Phys.: Condensed Matter*, 15:R1865, 2003.
- [19] Mona Berciu and R. N. Bhatt. Effects of disorder on ferromagnetism in diluted magnetic semiconductors. *Phys. Rev. Lett.*, 87:107203, 2001.
- [20] A. Chattopadhyay, S. Das Sarma, and A. J. Millis. Transition temperature of ferromagnetic semiconductors: A dynamical mean field study. *Phys. Rev. Lett.*, 87:227202, 2001.
- [21] T. Jungwirth, W. A. Atkinson, B. H. Lee, and A. H. MacDonald. Interlayer coupling in ferromagnetic semiconductor superlattices. *Phys. Rev. B*, 59:9818, 1999.
- [22] T. Dietl, H. Ohno, and F. Matsukura. Hole-mediated ferromagnetism in tetrahedrally coordinated semiconductors. *Phys. Rev. B*, 63:195205, 2001.
- [23] J. König, J. Schliemann, T. Jungwirth, and A.H. MacDonald. Ferromagnetism in (III,Mn)V semiconductors. In D.J. Singh and D.A. Papaconstantopoulos, editors, *Electronic Structure and Magnetism of Complex Materials*. Springer Verlag, Berlin, 2002.
- [24] J. Sinova, T. Jungwirth, S.-R. Eric Yang, J. Kucera, and A. H. MacDonald. Infrared conductivity of metallic (III,Mn)V ferromagnets. *Phys. Rev. B*, 66:041202, 2002.

- [25] G. Alvarez, M. Mayr, and E. Dagotto. Phase diagram of a model for diluted magnetic semiconductors beyond mean-field approximations. *Phys. Rev. Lett.*, 89:277202, 2002.
- [26] E. H. Hwang, A. J. Millis, and S. Das Sarma. Optical conductivity of ferromagnetic semiconductors. *Phys. Rev. B*, 65:233206, 2002.
- [27] M. J. Calderon, G. Gomez-Santos, and L. Brey. Impurity-semiconductor band hybridization effects on the critical temperature of diluted magnetic semiconductors. *Phys. Rev. B*, 66:075218, 2002.
- [28] G. Zarand and B. Janko. $\text{Ga}_{1-x}\text{Mn}_x\text{As}$: A frustrated ferromagnet. *Phys. Rev. Lett.*, 89:047201, 2002.
- [29] F. Matsukura, H. Ohno, A. Shen, and Y. Sugawara. Transport properties and origin of ferromagnetism in $(\text{Ga},\text{Mn})\text{As}$. *Phys. Rev. B*, 57:2037, 1998.
- [30] B. Beschoten, P.A. Crowell, I Malajovich, D.D. Awschalom, F. Matsukura, A. Shen, and H. Ohno. Magnetic circular dichroism studies of carrier-induced ferromagnetism in $(\text{Ga}_{1-x}\text{Mn}_x)\text{As}$. *Phys. Rev. Lett.*, 83:3073, 1999.
- [31] J. Szczytko, A. Twardowski, K. Swiatek, M. Palczewska, M. Tanaka, T. Hayashi, and K. Ando. Mn impurity in $\text{Ga}_{1-x}\text{Mn}_x\text{As}$ epilayers. *Phys. Rev. B*, 60:8304, 1999.
- [32] S. Sanvito, P. Ordejón, and N. A. Hill. First-principles study of the origin and nature of ferromagnetism in $\text{Ga}_{1-x}\text{Mn}_x\text{As}$. *Phys. Rev. B*, 63:165206, 2001.
- [33] J. Okabayashi, A. Kimura, O. Rader, T. Mizokawa, A. Fujimori, T. Hayashi, and M. Tanaka. Core-level photoemission study of $\text{Ga}_{1-x}\text{Mn}_x\text{As}$. *Phys. Rev. B*, 58:R4211, 1998.
- [34] K. Yu, W. Walukiewicz, T. Wojtowicz, I. Kuryliszyn, X. Liu, Y. Sasaki, and J. K. Furdyna. Effect of the location of Mn sites in ferromagnetic $\text{Ga}_{1-x}\text{Mn}_x\text{As}$ on its curie temperature. *Phys. Rev. B*, 65:201303, 2002.
- [35] M.J. Seong, S.H. Chung, H.M. Cheong, N. Samarth, and A. Mascarenhas. Spectroscopic determination of hole density in the ferromagnetic semiconductor $\text{Ga}_{1-x}\text{Mn}_x\text{As}$. *Phys. Rev. B*, 66:033202, 2002.
- [36] H. Munekata, H. Ohno, S.von Molnár, A. Segmüller, L.L. Chang, and L. Esaki. Diluted magnetic III-V semiconductors. *Phys. Rev. Lett.*, 63:1849, 1989.
- [37] A. Van Esch, L. Van Bockstal, J. De Boeck, G. Verbanck, A.S. van Steenberghe, P.J. Wellmann, B. Grietens, R. Bogaerts, F. Herlach, and G. Borghs. Interplay between the magnetic and transport properties in the III-V diluted magnetic semiconductor $\text{Ga}_{1-x}\text{Mn}_x\text{As}$. *Phys. Rev. B*, 56:13103, 1997.

- [38] H. Ohno and F. Matsukura. A ferromagnetic III-V semiconductor: (Ga,Mn)As. *Solid State Communications*, 117:179, 2001.
- [39] Y. D. Park, A.T. Hanbicki, S.C. Erwin, C.S. Hellberg, J.M. Sullivan, J.E. Mattson, T.F. Ambrose, A. Wilson, G. Spanos, and B.T. Jonker. A Group-IV ferromagnetic semiconductor: $\text{Mn}_x\text{Ge}_{1-x}$. *Science*, 295:651, 2002.
- [40] K.C. Ku, S.J. Potashnik, R.F. Wang, M.J. Seong, E. Johnston-Halperin, R. C. Meyers, S. H. Chun, A. Mascarenhas, A.C. Gossard, D.D. Awschalom, P. Schiffer, and N. Samarth. Highly enhanced curie temperature in low-temperature annealed [Ga,Mn]As epilayers. *Appl. Phys. Lett.*, 82:2302, 2003.
- [41] K. Yosida. *Theory of Magnetism*. Springer-Verlag, Berlin, 1996.
- [42] E. Dagotto, T. Hotta, and A. Moreo. Colossal magnetoresistant materials: the key role of phase separation. *Physics Reports*, 344:1, 2001.
- [43] S. Sanvito and N. A. Hill. Ground state of half-metallic zinc-blende MnAs. *Phys. Rev. B*, 62:15553, 2000.
- [44] M. van Schilfgaarde and O. N. Mryasov. Anomalous exchange interactions in III-V dilute magnetic semiconductors. *Phys. Rev. B*, 63:233205, 2001.
- [45] H. Akai. Ferromagnetism and its stability in the diluted magnetic semiconductor (In, Mn)As. *Phys. Rev. Lett.*, 81:3002, 1998.
- [46] J.H. Park, S.K. Kwon, and B.I. Min. Electronic structures of III-V based ferromagnetic semiconductors: half-metallic phase. *Physica B*, 281-283:703, 2000.
- [47] C. Zener. Interaction between the d shells in the transition metals. *Phys. Rev.*, 81:440, 1952.
- [48] J.R. Schrieffer and P. A. Wolf. Relation between the Anderson and Kondo Hamiltonian. *Phys. Rev.*, 149:491, 1966.
- [49] H. Tsunetsugu, M. Sigrist, and K. Ueda. The ground-state phase diagram of the one-dimensional Kondo lattice model. *Phys. Rev.*, 69:809, 1997.
- [50] P.W. Anderson. Localized magnetic states in metals. *Phys. Rev.*, 124:41, 1961.
- [51] J. Kondo. Resistance minimum in dilute magnetic alloys. *Prog. Theor. Phys.*, 32:37, 1964.
- [52] Malcolm P. Kennett, Mona Berciu, and R. N. Bhatt. Monte carlo simulations of an impurity-band model for III-V diluted magnetic semiconductors. *Phys. Rev. B*, 66:045207, 2002.

- [53] C. Timm, F. Schäfer, and F. von Oppen. Comment on 'Effects of disorder on ferromagnetism in diluted magnetic semiconductors'. *Phys. Rev. Lett.*, 90:029701, 2003.
- [54] M. Mayr, G. Alvarez, and E. Dagotto. Global versus local ferromagnetism in a model for diluted magnetic semiconductors studied with Monte Carlo techniques. *Phys. Rev. B*, 65:241202, 2002.
- [55] E.L. Nagaev. *Physics of Magnetic Semiconductors*. Mir Publishers, Moscow, 1983.
- [56] N. W. Ashcroft and N. D. Mermin. *Solid State Physics*. Saunders College Publishing, New York, 1976.
- [57] W.A. Harrison. *Electronic Structure and the Properties of Solids*. Dover Publications, New York, 1989.
- [58] J. Burgy, M. Mayr, V. Martin-Mayor, A. Moreo, and E. Dagotto. Colossal effects in transition metal oxides caused by intrinsic inhomogeneities. *Phys. Rev. Lett.*, 87:277202, 2001.
- [59] E. Dagotto, editor. *Nanoscale Phase Separation and Colossal Magnetoresistance*. Springer Verlag, Berlin, 2002.
- [60] N. Metropolis, A.W. Rosenbluth, M.N. Rosenbluth, A.H. Teller, and E. Teller. Equations of state calculations by fast computing machines. *J. Chem. Phys.*, 21:1087, 1953.
- [61] R. J. Glauber. Time-dependent statistics of the Ising model. *Journal of Math. Phys.*, 4:294, 1963.
- [62] K. Binder and D. W. Heermann, editors. *Monte Carlo Simulations In Statistical Physics*. Springer Verlag, Berlin, 1992.
- [63] H. Aliaga, D. Magnoux, A. Moreo, D. Poilblanc, S. Yunoki, and E. Dagotto. cond-mat/0303513, 2003.
- [64] N. Furukawa, Y. Motome, and H. Nakata. Monte carlo algorithm for the double exchange model optimized for parallel computations. *Computer Physics Communications*, 142:410, 2001.
- [65] J. L. Alonso, L. A. Fernández, F. Guinea, V. Laliena, and V. Martín-Mayo. Hybrid monte carlo algorithm for the double exchange model. *Nucl. Phys. B*, 596:587, 2001.
- [66] T. Dietl. Ferromagnetic semiconductors. *Semicond. Sci. Technol.*, 17:377, 2002.

- [67] S. J. Potashnik, K. C. Ku, R. Mahendiran, S. H. Chun, R. F. Wang, N. Samarth, and P. Schiffer. Saturated ferromagnetism and magnetization deficit in optimally annealed (Ga,Mn)As epilayers. *Phys. Rev. B*, 66:012408, 2002.
- [68] R.P. Campion, K.W. Edmonds, L.X. Zhao, K.Y. Wang, C.T. Foxon, B.L. Gallagher, and C. R. Staddon. The growth of GaMnAs films by molecular beam epitaxy using arsenic dimers. *Journal of Crystal Growth*, 251:311, 2003.
- [69] J. Okabayashi, T. Mizokawa, D. D. Sarma, A. Fujimori, T. Slupinski, A. Oiwa, H. Munekata, and A. Fujimori. Electronic structure of $\text{In}_{1-x}\text{Mn}_x\text{As}$ studied by photoemission spectroscopy: Comparison with $\text{Ga}_{1-x}\text{Mn}_x\text{As}$. *Phys. Rev. B*, 65:161203, 2002.
- [70] M. Linnarsson, E. Janzen, B. Monemar, M. Kleverman, and A. Thilderkvist. Electronic structure of the GaAs: Mn_{Ga} center. *Phys. Rev. B*, 55:6938, 1997.
- [71] E. Kulatov, H. Nakayama, H. Mariette, H. Ohta, and Y. A. Uspenskii. Electronic structure, magnetic ordering, and optical properties of GaN and GaAs doped with Mn. *Phys. Rev. B*, 66:045203, 2002.
- [72] T. Dietl, H. Ohno, F. Matsukura, J. Cibert, and D. Ferrand. Zener model description of ferromagnetism in Zinc-Blende magnetic semiconductors. *Science*, 287:1019, 2000.
- [73] J. Konig, H. H. Lin, and A. H. MacDonald. Theory of diluted magnetic semiconductor ferromagnetism. *Phys. Rev. Lett.*, 84:5628, 2000.
- [74] S.-R. Eric Yang, J. Sinova, T. Jungwirth, Y.P. Shim, and A.H. MacDonald. Non-drude optical conductivity of (III,Mn)V ferromagnetic semiconductors. *Phys. Rev. B*, 67:045205, 2003.
- [75] G. Alvarez and E. Dagotto. Single-band model for diluted magnetic semiconductors: Dynamical and transport properties and relevance of clustered states. *Phys. Rev. B.*, 68:045202, 2003.
- [76] A. Kaminski and S. Das Sarma. Polaron percolation in diluted magnetic semiconductors. *Phys. Rev. Lett.*, 88:247202, 2002.
- [77] S.H. Chun, S. J. Potashnik, K. C. Ku, P. Schiffer, and N. Samarth. Spin-polarized tunneling in hybrid metal-semiconductor magnetic tunnel junctions. *Phys. Rev. B*, 66:100408, 2002.
- [78] A. Moreo, S. Yunoki, and E. Dagotto. Pseudogap formation in models for manganites. *Phys. Rev. Lett.*, 83:2773, 1999.

- [79] J. Okabayashi, A. Kimura, O. Rader, T. Mizokawa, A. Fujimori, T. Hayashi, and M. Tanaka. Angle-resolved photoemission study of $\text{Ga}_{1-x}\text{Mn}_x\text{As}$. *Phys. Rev. B*, 64:125304, 2001.
- [80] H. Asklund, L. Ilver, J. Kanski, J. Sadowski, and R. Mathieu. Photoemission studies of $\text{Ga}_{1-x}\text{Mn}_x\text{As}$: Mn concentration dependent properties. *Phys. Rev. B*, 66:115319, 2002.
- [81] T. Jungwirth, Jürgen König, Jairo Sinova, J. Kucera, and A. H. MacDonald. Curie temperature trends in (III,Mn)V ferromagnetic semiconductors. *Phys. Rev. B*, 66:012402, 2002.
- [82] E. J. Singley, R. Kawakami, D. D. Awschalom, and D. N. Basov. Infrared probe of itinerant ferromagnetism in $\text{Ga}_{1-x}\text{Mn}_x\text{As}$. *Phys. Rev. Lett.*, 89:097203, 2002.
- [83] H. Hirakawa, A. Oiwa, and H. Munekata. Infrared optical conductivity of $\text{In}_{1-x}\text{Mn}_x\text{As}$. *Physica E*, 10:215, 2001.
- [84] J. A. Vergés. Computational implementation of the Kubo formula for the static conductance: application to two-dimensional quantum dots. *Comp. Phys. Commun.*, 118:71, 1999.
- [85] P.A. Lee and D.S. Fisher. Anderson localization in two dimensions. *Phys. Rev. Lett.*, 47:882, 1981.
- [86] G. Mahan. *Many-particle Physics*. Plenum Press, New York, 1993.
- [87] M.J. Calderón, J.A. Vergés, and L. Brey. Conductance as a function of temperature in the double-exchange model. *Phys. Rev. B*, 59:4170, 1999d.
- [88] Y. D. Park, A. Wilson, A. T. Hanbicki, T. Ambrose J. E. Mattson, G. Spanos, and B. T. Jonker. Magnetoresistance of Mn:Ge ferromagnetic nanoclusters in a diluted magnetic semiconductor matrix. *Appl. Phys. Lett.*, 78:2739, 2001.
- [89] K.M. Lang, V. Madhavan, J. E. Hoffman, E. W. Hudson, H. Eisaki, S. Uchida, and J. C. Davis. Imaging the granular structure of high-Tc superconductivity in underdoped $\text{Bi}_2\text{Sr}_2\text{CaCu}_2\text{O}_{8+\delta}$. *Nature*, 415:412, 2002.
- [90] J. M. Tranquada, B. J. Sternlieb, J. D. Axe, Y. Nakamura, and S. Uchida. Evidence for stripe correlations of spins and holes in copper oxide superconductors. *Nature*, 375:561, 1995.
- [91] A. Dakhama, B. Lakshmi, and D. Heiman. Magnetic interactions and transport in (Ga,Cr)As. *Phys. Rev. B*, 67:115204, 2003.
- [92] I. K. Schuller et al. A Snapshot View of High Temperature Superconductivity 2002, 1981.

- [93] R.S. Decca, H.D. Drew, E. Osquiguil, B. Maiorov, and J. Guimpel. Anomalous proximity effect in underdoped $\text{YBa}_2\text{Cu}_3\text{O}_{6+x}$ josephson junctions. *Phys. Rev. Lett.*, 85:3708, 2000.
- [94] S. Sorella, G. B. Martins, F. Becca, C. Gazza, L. Capriotti, A. Parola, and E. Dagotto. Superconductivity in the two-dimensional t-J model. *Phys. Rev. Lett.*, 88:117002, 2002.
- [95] A. Ghosal, Catherine Kallin, and A. John Berlinsky. Competition of superconductivity and antiferromagnetism in a d -wave vortex lattice. *Phys. Rev. B*, 66:214502, 2002.
- [96] M. Ichioka and K. Machida. Electronic structure of stripes in two-dimensional hubbard model. *J. Phys. Soc. Jpn.*, 68:4020, 1999.
- [97] S.C. Zhang. A unified theory based on $SO(5)$ symmetry of superconductivity and antiferromagnetism. *Science*, 275:1089, 1997.
- [98] B. Kyung, J-S Landry, and A.-M. S. Tremblay. Antiferromagnetic fluctuations and d -wave superconductivity in electron-doped high-temperature superconductors. *Phys. Rev. B*, 68:174502, 2003.
- [99] M. Moraghebi, S. Yunoki, and A. Moreo. Robust d -wave pairing correlations in a hole-doped spin-fermion model. *Phys. Rev. Lett.*, 88:187001, 2002.
- [100] X.J. Zhou, T. Yoshida, S. A. Kellar, P. V. Bogdanov, E. D. Lu, A. Lanzara, M. Nakamura, T. Noda, T. Kakeshita, H. Eisaki, S. Uchida, A. Fujimori, Z. Hussain, and Z.-X. Shen. Dual nature of the electronic structure of $(\text{La}_{2-x-y}\text{Nd}_y\text{Sr}_x)\text{CuO}_4$ and $\text{La}_{1.85}\text{Sr}_{0.15}\text{CuO}_4$. *Phys. Rev. Lett.*, 86:5578, 2001.
- [101] T. Yoshida, X. J. Zhou, T. Sasagawa, W. L. Yang, P. V. Bogdanov, A. Lanzara, Z. Hussain, T. Mizokawa, A. Fujimori, H. Eisaki, Z.-X. Shen, T. Kakeshita, and S. Uchida. Metallic behavior of lightly doped $\text{La}_{2-x}\text{Sr}_x\text{CuO}_4$ with a Fermi surface forming an arc. *Phys. Rev. Lett.*, 91:027001, 2003.
- [102] H. Eisaki, N. Kaneko, D.L. Feng, A. Damascelli, P.K. Mang, K.M. Shen, Z.-X. Shen, and M. Greven. cond-mat/0312570, 2003.
- [103] A. Moreo, S. Yunoki, and E. Dagotto. Phase separation scenario for manganese oxides and related materials. *Science*, 283:2034, 1999.
- [104] Y. Tokura. *Colossal Magnetoresistive Oxides*. Gordon and Breach, New York, 2000.
- [105] M. Fäth, S. Freisem, A. A. Menovsky, Y. Tomioka, J. Aarts, and J. A. Mydosh. Spatially inhomogeneous metal-insulator transition in doped manganites. *Science*, 285:1540, 1999.

- [106] N. Theodoropoulou, A.F. Hebard, M.E. Overberg, C.R. Abernathy, S.J. Pearton, S.N.G. Chu, and R.G. Wilson. Unconventional carrier-mediated ferromagnetism above room temperature in ion-implanted (Ga, Mn)P:C. *Phys. Rev. Lett.*, 89:107203, 2003.
- [107] V. Yukalov. Phase transitions and heterophase fluctuations. *Phys. Rep.*, 208:395, 1991.
- [108] A. Auerbach. *Interacting Electrons and Quantum Magnetism*. Springer-Verlag, Berlin, 1994.
- [109] N. D. Mermin and H. Wagner. Absence of ferromagnetism or antiferromagnetism in one- or two-dimensional isotropic heisenberg models. *Phys. Rev. Lett.*, 17:1133, 1966.
- [110] E. Manousakis. The spin-1/2 heisenberg antiferromagnet on a square lattice and its application to the cuprous oxides. *Rev. Mod. Phys.*, 63:1, 1991.
- [111] E. H. Lieb I. Affleck, T. Kennedy and H. Tasaki. Valence bond ground states in isotropic quantum antiferromagnets. *Commun. Math. Phys.*, 115:477, 1988.
- [112] E. H. Lieb J. Frolich, R. Israel and B. Simon. Phase transitions and reflection positivity. I. General theory and long range lattice models. *Commun. Math. Phys.*, 62:1, 1978.
- [113] H. Nakano and M. Takahashi. Magnetic properties of quantum Heisenberg ferromagnets with long-range interactions. *Phys. Rev. B*, 52:6606, 1995.
- [114] B. S. Shastry. Exact solution of an $S = 1/2$ Heisenberg antiferromagnetic chain with long-ranged interactions. *Phys. Rev. Lett.*, 60:639, 1988.
- [115] F. D. M. Haldane. Exact Jastrow-Gutzwiller resonating-valence-bond ground state of the spin-(1/2 antiferromagnetic Heisenberg chain with $1/r^2$ exchange. *Phys. Rev. Lett.*, 60:635, 1988.
- [116] F. J. Dyson. An Ising ferromagnet with discontinuous long-range order. *Commun. Math. Phys.*, 21:269, 1971.
- [117] B. Simon. Absence of continuous symmetry breaking in a one-dimensional n^2 model. *J. Stat. Phys.*, 26:307, 1981.
- [118] R.B. Griffiths. Peierls proof of spontaneous magnetization in a two-dimensional Ising ferromagnet. *Phys. Rev.*, 136:A437, 1964.
- [119] L. Onsager. Crystal statistics. I. A two-dimensional model with an order-disorder transition. *Phys. Rev.*, 65:117, 1944.

BIOGRAPHICAL SKETCH

Gonzalo Alvarez

Education

- Aug. 2000 - present Ph. D. student.
Condensed Matter Theory Group at the
National High Magnetic Field Laboratory.
Advisor: Prof. Elbio Dagotto.
- April 1999 M.S. in Physics.
(Institute of Physics,
University of Montevideo, Uruguay).
- Sept. 1996 B.S. in Physics
(School of Science,
University of Montevideo, Uruguay).

Research

- Aug. 2000 - present Graduate Research Assistant.
Advisor: Prof. Elbio Dagotto.
Ph. D. Dissertation: Theoretical studies
of Models for
Diluted Magnetic Semiconductors and
Transition-Metal Oxides.
- Sept. 1996 - Aug. 2000 Research assistant.
Quantum Field Theory Group,
School of Science, Montevideo. Uruguay.
Topic: Lattice Gauge Theory. Advisor:
Dr. Hugo Fort.

Teaching

- Aug. 2000 - Aug. 2001 Teaching assistant. Physics Department.
Florida State University.
- Sept. 1996 - Aug. 2000 Teaching assistant. Physics Department.
University of Montevideo. Uruguay.

Honors

- Recipient of GMAG Outstanding Dissertation in Magnetism award (Invited Talk at the March Meeting, Montreal, 2004).

Publications

- G. Alvarez, M. Mayr, A. Moreo and E. Dagotto, *Prediction of Colossal Effects in High T_C Superconductors*, cond-mat/0401474.
- C. Sen, G. Alvarez and E. Dagotto, *Effects of Disorder Near the Metal to Insulator Transition in Manganites*, cond-mat/0401619.
- G. Alvarez and E. Dagotto, *Single-Band Model for Diluted Magnetic Semiconductors: Dynamical and Transport Properties and Relevance of Clustered States*, Phys. Rev. B **68**, 045202 (2003).
- G. Alvarez, M. Mayr, and E. Dagotto, *Phase Diagram of a Model for Diluted Magnetic Semiconductors Beyond Mean-Field Approximations*, Phys. Rev. Lett. **89**, 277202 (2002).
- M. Mayr, G. Alvarez, and E. Dagotto, *Global versus local ferromagnetism in a model for diluted magnetic semiconductors studied with Monte Carlo techniques*, Phys. Rev. B **65** 241202 (2002).
- G. Alvarez and H. Fort, *Effect of large amplitude fluctuations in the Ginzburg-Landau phase transition*, Phys. Rev. B **64**, 092506 (2001).
- G. Alvarez and H. Fort, *Phase transitions driven by vortices in two-dimensional superfluids and superconductors: From Kosterlitz-Thouless to first order*, Phys. Rev. B **63**, 132504 (2001).

- J. M. Aroca, H. Fort and G. Alvarez, *Finite lattice Hamiltonian computations in the P-representation: The Schwinger model*, Europhys. Lett, **45** (5), 565 (1999)

Book Chapters and Conference Proceedings

- G. Alvarez and E. Dagotto, *Clustered States as a New Paradigm of Condensed Matter Physics*, cond-mat / 0305628. Proceedings of the International Conference on Magnetism, ICM, Rome 2003
- Coauthor of Chapter 7, *Monte Carlo simulations and Application to Manganite Models of Nanoscale Phase Separation and Colossal Magnetoresistance* by E. Dagotto. Springer-Verlag. Berlin. Heidelberg. 2002.

Meetings and Workshops

- Invited Speaker, Seminar, University of Southern California, Los Angeles, CA. March 26, 2004.
- Invited Talk, *Relevance of Clustered States in Diluted Magnetic Semiconductors and Other Materials*, University of Maryland, College Park, MD. March 3rd, 2004.
- Invited Speaker, Seminar, Rutgers University, February 26th, 2004.
- Invited Talk, March Meeting of the American Physical Society 2004, *GMAG Dissertation Award: Computational Studies of Diluted Magnetic Semiconductors and Other Materials*
- Workshop, *Monte Carlo Methods for Classical and Quantum Spin Systems and Beyond*. Oak Ridge National Laboratory. August 4-8, 2003.

- Invited talk, *Theoretical Study of a model for Diluted Magnetic Semiconductors*. UF / FSU Workshop on Condensed Matter, Gainesville, FL, April 26, 2003.
- March Meeting of the American Physical Society, 2003, Austin, TX. Section S24.004. G. Alvarez, E. Dagotto. *Dynamical and transport properties of a spin-fermion model for Diluted Magnetic Semiconductors*.
- March Meeting 2002 of the American Physical Society, Indianapolis, IN. Section L19.003 G. Alvarez, E. Dagotto. *Monte Carlo Study of Dilute Magnetic Semiconductors*.
- Summer School on Lattice QCD, at *The European Centre for Theoretical Studies in Nuclear Physics and Related Areas*, Trento, Italy, 1998.

Computer / Technical Proficiencies

- Experience in implementing Monte Carlo simulations for various Kondo Lattice models, using both exact diagonalization and serial/parallel polynomial expansion method in the fermionic sector. Development of computer program to calculate a series expansion for the Schwinger model.
- Computer Languages: Fluent knowledge of C, C++ and STL programming, Perl, UNIX shell scripting, XML. Parallel computation using MPI, Unix system administration.